The Density Matrix Renormalization Group

Applied to mesoscopic structures

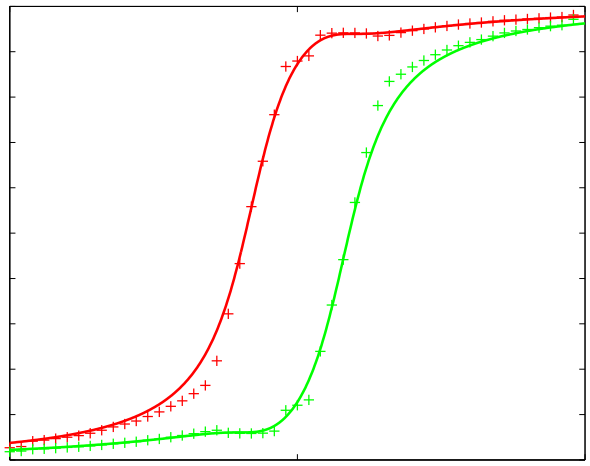

M.Sc. Thesis
Dan Bohr
April 2004

MIC – Department of Micro and Nanotechnology
Technical University of Denmark
Lyngby, Denmark

The Density Matrix Renormalization Group Applied to mesoscopic structures

© Dan Bohr, 2004.

M.Sc. Thesis, Technical University of Denmark.

MIC – Department of Micro and Nanotechnology
Ørsteds Plads
DTU – Building 345east
DK-2800 Kgs. Lyngby
Denmark
E-mail: dab@mic.dtu.dk
Web: http://www.mic.dtu.dk

Typeset in LaTeX 2ε

Abstract

In recent years much attention has been focused on understanding various nanotechnological devices. Doing exact calculations using quantum mechanical models limits the manageable system size heavily due to the exponentially large Hilbert space, making full quantum calculations unfeasible in the vast majority of cases. Non-perturbative methods and methods beyond mean field theories, such as the Density Matrix Renormalization Group (DMRG), are of great interest when studying systems with strong correlations, such as quantum wires and dots.

We have made our own implementation of DMRG and studied two model systems: (*i*) the one-dimensional Hubbard model at half filling and (*ii*) a two level quantum dot coupled to semi-infinite leads. For the Hubbard model we studied the effect of on-site repulsion, while for the quantum dot with leads we computed the occupation as a function of chemical potential varying the strength of the dot-lead coupling. In the non-interacting limit we have compared DMRG and analytic Green's function results and found good agreement when keeping sufficiently many states in the DMRG calculation.

We used MatLab to implement DMRG which turned out to make parts of the implementation cumbersome due to the matrix layout of MatLab. Based on our experience we believe that low level object oriented languages would be more suitable for DMRG.

Recently we have studied the possibility of calculating dynamical properties using a simple Lanczos method combined with DMRG. We have not yet been successful and probably more sophisticated methods, as proposed by both Jeckelmann and White, are required to successfully perform these calculations.

To approach transport we have calculated the occupation of a biased dot versus gate voltage using DMRG and these results have been compared to Green's function results. For small gate voltages the agreement is fine, while for larger gate voltages there is a qualitative disagreement, and a more careful analysis is needed to remedy this.

Preface

The present thesis is submitted in candidacy for the Master of Science degree within the Applied Physics program at the Technical University of Denmark (DTU). It is the result of part of my work at the Department of Micro and Nanotechnology (MIC) in the period May 2003 to April 2004 under supervision of Professor Antti-Pekka Jauho.

The thesis concerns the powerful numerical method known as the Density Matrix Renormalization Group (DMRG). On the theoretical level DMRG is fairly simple to understand; an elegant derivation of the DMRG states can be given and superficially the DMRG algorithms are easy to understand. Actually implementing it turned out to be much more difficult, and I spent long time setting up matrix representations of operators, expanding the Hilbert space as the system grows and other vital technicalities.

Having taken care of these issues I found that doing precise DMRG calculations indeed is *very* hardware demanding. Virtually any DMRG calculation presented in this thesis took days rather than hours – some even nearly a week – which obviously limited the number of calculations I was able to do.

I would like to thank my supervisor for introducing me to the field of DMRG through this project. During the project many people have helped me in various ways, and apart from my supervisor I would like to emphasize Professor Stellan Östlund, who kindly invited me to Chalmers and helped me with the DMRG implementation on the Hubbard model, Professor Richard Berkovits, who accepted to answer questions about the quantum dot with leads setup, substantially improving the quality of my calculations, and Thomas Frederiksen who's useful comments to the manuscript I appreciate very much.

ooOoo

Lyngby
April 30, 2004

Dan Bohr

Contents

Chapter 1

Introduction

The complexity of models used in solid state physics has increased dramatically since the first models were proposed by Drude and Sommerfeld. Today quantum mechanical models are very powerful tools in the description of nature, but present one formidable challenge: The Hilbert space needed to describe a given system grows exponentially with the system size, and thus even the fastest of computers rapidly reach a maximum system size that can be handled. No matter how fast computers are available this will always impose an upper limit to how large systems we can treat using exact calculations.

Therefore a systematic way of sorting the information according to vitality to the description is useful. When describing certain limits, e.g. the low energy limit, not all information is needed and we may disregard some parts without changing the description significantly, and hence increase the manageable system size. One type is the Renormalization Groups (RG's) which are widely used in modern science.

The goal of any renormalization group is to find the best states to retain when describing a system of l states keeping only $m < l$ states. K. G. Wilson was among the first to successfully perform numerical renormalization [1]. In his approach the line of argument is that the most important states to retain when describing low energy properties are the lowest eigenvalue eigenstates of the Hamiltonian.

Wilson's procedure had many successes but for interacting quantum lattice systems it fails, mainly due to problems with the boundary conditions. Some can be remedied by choosing other boundary conditions or by putting the system of interest inside a larger system – a setup known as the *superblock* setup.[1] This failure can be illustrated by the tight binding chain (TBC). In the continuum limit the TBC describes a particle in a box with infinitely high potentials at the boundaries. Consider the joining of the ground state wavefunctions of the two blocks to try to form a ground state

[1] Elaboration on Wilson's renormalization can be found in the original work by Wilson and Kogut [1], and the Springer Lecture Notes in Physics edited by Peschel *et al.* [2].

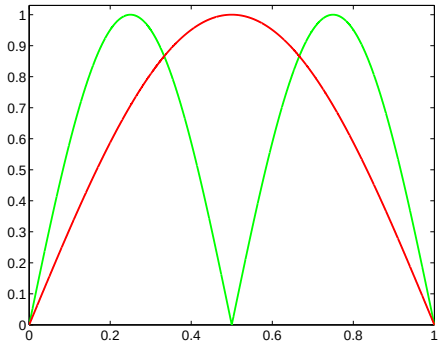

Figure 1.1: Attempt to approximate the superblock ground state wavefunction by the ground state wavefunctions of two subblocks. The wavefunctions are not normalized and the units are arbitrary.

wavefunction of the superblock as seen in Fig. 1.1. The true ground state wavefunction of the superblock deviates qualitatively from the one predicted by the joint wavefunctions of the separate blocks, due to the boundary condition imposed on each of the blocks.

Faced with such problems White formulated the Density Matrix Renormalization Group (DMRG) in 1992 [3, 4]. DMRG is able to handle strongly interacting quantum systems, including quantum lattice systems, and generally gives very accurate results, making it a natural and obvious candidate for many numerical calculations. Since then DMRG has been established as a very powerful tool used by many groups around the world.

In recent years much attention has been focused on transport phenomena, also in strongly correlated systems where existing methods are limited. Analytic studies have only been carried out in certain limits, and usually under quite severe restrictions. Mean field theories neglect higher order correlations *ab initio* thereby restricting the kind of systems that can be described. Contrary DMRG is able to handle strongly interacting quantum systems in equilibrium, and has also turned out to be a good starting point for treating transport in strongly interacting systems [5, 6].

Since White introduced DMRG, the basic algorithm has been extended and modified to treat many different systems, ranging from *ab initio* quantum chemistry calculations, over applications in high energy physics to calculating dynamical properties using DMRG. In this context it is interesting to note that several schemes to calculate dynamical properties and transport have been proposed in the literature [2, 5, 6, 7].

In this thesis we aim at a basic understanding of the theory behind DMRG and at implementing DMRG on a couple of models. In general we

attempt to include sufficient technical details such that beginners in the field can write their own DMRG implementations. Some experience in numerical physics and mathematics as well as with a mathematical programming language would however be a great advantage.

1.1 Outline of the thesis

In Chap. 2 we present in general terms the theoretical framework of DMRG and the important DMRG algorithms are formulated. The general idea behind DMRG can be understood by a fairly simple derivation of the DMRG states – and a loose criterion for successful use of DMRG is formulated. Methods for calculating observables are presented, and a few expansions of the basic DMRG are discussed.

In Chap. 3 we show how DMRG is implemented on the one-dimensional Hubbard chain. We use our implementation to calculate ground state properties at half filling, both with and without a magnetic field, and varying the on-site repulsion and the chainlength.

In Chap. 4 and 5 we implement DMRG on a quantum dot coupled to one and two semi-infinite one-dimensional leads. We use DMRG to calculate the occupation of the dot as a function of chemical potential in the system. In the two lead case we additionally calculate the occupation when the dot is biased using different chemical potentials for the left and right lead, and attempt a very simple calculation of the static current.

To increase the transparency of the text parts of Chap. 2 are repeated in the specific contexts in Chap. 3, 4 and 5, and therefore some sections may resemble each other.

In Chap. 6 we present a simpler implementation of DMRG on single particle quantum mechanics. We show that the truncation procedure of DMRG reduces to a projection of the wavefunction, making single particle quantum mechanics a good starting point for DMRG calculations.

Several improvements of the implementation performed in this work that would render the calculation faster and more reliable are proposed in Chap. 7. A number of extensions of DMRG are mentioned, enabling calculations beyond reach of ordinary DMRG.

In Chap. 8 we briefly summarize this work and discuss the current status of DMRG in the literature. Perspectives of DMRG and its extensions are discussed, and the natural continuation of this work on DMRG within condensed matter physics and nanotechnology is outlined.

Chapter 2

The Density Matrix Renormalization Group

Realizing the boundary condition problem of Wilson's Numerical Renormalization mentioned in the introduction White formulated the Density Matrix Renormalization Group (DMRG) algorithms in the early 90s [3, 4]. DMRG uses a superblock setup consisting of a system block and an environment block, and the line of argument as to which states to retain is very different from other renormalization groups.

In this chapter we review DMRG and formulate in general terms the two important algorithms used in this work. We give a simple derivation of the DMRG states, which shows there is no perturbative series involved, so that the systems may be arbitrary strongly correlated.

Based on this derivation we formulate a loose criterion for successful application of DMRG. Finally we show how expectation values are handled in the DMRG framework and suggest several ways to speed up calculations. This chapter is mainly based on the Springer Lecture Notes in Physics edited by Peschel *et al.* [2], and the original articles by White [3, 4].

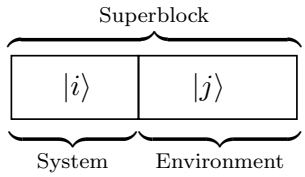

Figure 2.1: Most general superblock setup. States $|i\rangle$ are system states and states $|j\rangle$ are environment states.

2.1 Retained states

The basic idea of DMRG is to optimize the *basis* in which the system is described. This is done using a superblock setup where the system is joined with an environment block to eliminate boundary condition problems. To see how this works we consider an arbitrary superblock state $|\psi\rangle$. Using the notation in Fig. 2.1, denoting system states by $|i\rangle$ and environment states by $|j\rangle$, this state can be written in product form

$$|\psi\rangle \;=\; \sum_{i=1}^{I}\sum_{j=1}^{J}\psi_{ij}\,|i\rangle\,|j\rangle\,, \tag{2.1}$$

where $\sum_{i=1}^{I}$ denotes summation over the complete basis of the system block, and $\sum_{j=1}^{J}$ denotes summation over the complete basis of the environment block. The reduced density matrix (RDM) for the system block is obtained by tracing out the environment degrees of freedom[1]

$$\begin{aligned}\rho_{ii'} \;&\equiv\; \sum_{j}\psi^{*}_{i'j}\psi_{ij}\\ &=\; \sum_{j}\psi_{ij}\psi^{\dagger}_{ji'},\end{aligned} \tag{2.2}$$

or in matrix notation

$$\rho \;=\; \psi\psi^{\dagger}. \tag{2.3}$$

For any *system* block operator A we then find the quantum mechanical average as

$$\begin{aligned}\langle\psi|A|\psi\rangle \;&=\; \sum_{iji'j'}\langle j|\langle i|A|i'\rangle|j'\rangle\psi_{i'j'}\psi^{\dagger}_{ji}\\ &=\; \sum_{ii'}A_{ii'}\sum_{j}\psi_{i'j}\psi^{\dagger}_{ji}\\ &=\; \sum_{ii'}A_{ii'}\rho_{i'i}\\ &=\; \mathrm{Tr}\rho A.\end{aligned} \tag{2.4}$$

Normalizing ρ, $\mathrm{Tr}\rho = 1$, and denoting its eigenstates by $|u^{\alpha}\rangle$ and the eigenvalues by $w_\alpha \geq 0$ we have $\sum_\alpha w_\alpha = 1$. For any system operator A we may write the trace in this eigenbasis

$$\langle\psi|A|\psi\rangle \;=\; \sum_{\alpha} w_\alpha\,\langle u^{\alpha}|\,A\,|u^{\alpha}\rangle\,. \tag{2.5}$$

[1] This is the definition used by Feynman [8]. White and many others in the community use $\rho_{ii'} = \sum_j \psi^{*}_{ij}\psi_{i'j}$. This discrepancy seems to be quite persistent in the literature.

The goal is to construct the best possible approximate state, $|\bar{\psi}\rangle \approx |\psi\rangle$, for the superblock using a given number of states. Eq. (2.5) yields a hint: If for one particular α we had $w_\alpha = 0$ we would make *no error* by disregarding the corresponding state $|u^\alpha\rangle$ when calculating quantum mechanical averages.

Mathematically the goal is to minimize

$$S = \left| |\psi\rangle - |\bar{\psi}\rangle \right|^2, \tag{2.6a}$$

$$|\bar{\psi}\rangle = \sum_{\alpha,j} a_{\alpha,j} |u^\alpha\rangle |j\rangle, \quad \alpha = 1, \ldots, m < I. \tag{2.6b}$$

by varying over all coefficients $a_{\alpha,j}$ and choosing the best possible orthonormal basis states u^α, $\langle u^\alpha | u^{\alpha'} \rangle = \delta_{\alpha\alpha'}$.

In order to map the problem of finding the best states and coefficients onto a known form we use a change of basis

$$\begin{aligned} |\bar{\psi}\rangle &= \sum_\alpha |u^\alpha\rangle \sum_j a_{\alpha,j} |j\rangle \\ &\equiv \sum_\alpha a_\alpha |u^\alpha\rangle |v^\alpha\rangle, \quad a_\alpha |v^\alpha\rangle = \sum_j a_{\alpha,j} |j\rangle . \end{aligned} \tag{2.7}$$

Normalization of states $|v^\alpha\rangle$ yields

$$\begin{aligned} \langle v^\alpha \mid v^\alpha \rangle &\equiv 1 \\ &= \sum_j \langle v^\alpha \mid j \rangle \langle j \mid v^\alpha \rangle \\ &= \sum_j \left| v_j^\alpha \right|^2, \end{aligned} \tag{2.8}$$

and a_α is chosen so that this is fulfilled, $|a_\alpha|^2 = \sum_j |a_{\alpha,j}|^2$.

Switching to matrix notation and using m basis states in the approximate state $|\bar{\psi}\rangle$, the error measure is

$$\begin{aligned} S &= \sum_{ij} S_{ij} \\ &= \sum_{ij} \left(\psi_{ij} - \sum_{\alpha=1}^{m} a_\alpha u_i^\alpha v_j^\alpha \right)^2, \end{aligned} \tag{2.9}$$

a form known from linear algebra.[2] The state vector of the superblock $|\psi\rangle$ is represented by the rectangular (possibly complex) matrix ψ_{ij} defined in Eq. (2.1), and we may write it in singular value decomposition,[3]

$$\psi = UDV^\dagger, \tag{2.10}$$

[2] S in Eq. (2.9) is the square of the Frobenius norm of the matrix $(\psi - \bar{\psi})$, see e.g. `http://www.uwlax.edu/faculty/will/svd/norm/`.

[3] Eric W. Weisstein. "Singular Value Decomposition." From MathWorld–A Wolfram Web Resource. `http://mathworld.wolfram.com/SingularValueDecomposition.html`.

where U and D are $I \times I$ matrices and V is $J \times I$, where I and J are the number of states in the system and environment blocks respectively. U and V are unitary and D is diagonal with positive elements. The connection between U, V, and D can be demonstrated as follows:

$$\begin{aligned} \psi\psi^\dagger &= UDV^\dagger VDU^\dagger \\ &= UD^2U^\dagger \Rightarrow \\ \psi\psi^\dagger U &= UD^2 \\ &= U\mathrm{diag}(\sigma_1^2, \ldots, \sigma_I^2), \end{aligned} \tag{2.11a}$$

$$\begin{aligned} \psi^\dagger\psi &= VDU^\dagger UDV^\dagger \\ &= VD^2V^\dagger \Rightarrow \\ \psi^\dagger\psi V &= VD^2 \\ &= V\mathrm{diag}(\sigma_1^2, \ldots, \sigma_I^2). \end{aligned} \tag{2.11b}$$

Hence the elements of D can be found as the square root of the eigenvalues of $\psi\psi^\dagger$ or $\psi^\dagger\psi$. The columns of U are the corresponding eigenvectors of $\psi\psi^\dagger$ while the columns of V are the corresponding eigenvectors of $\psi^\dagger\psi$.[4]

Now we see how to minimize S in Eq. (2.9): for a_α choose the m largest values of σ_i, for u^α choose the corresponding columns of U, and for v^α choose the corresponding columns of V. For a given $m < I$ this will be the optimal choice. Note that the singular value decomposition is used only in the derivation of the DMRG states and *not* in numerical calculations.

From Eq. (2.11a) it is clear that the singular value decomposition is equivalent to diagonalization of the reduced density matrix

$$\begin{aligned} \rho &= \psi\psi^\dagger, \\ \psi\psi^\dagger U &= U\mathrm{diag}(\sigma_1^2, \ldots, \sigma_I^2) \Rightarrow \\ U^\dagger\rho U &= \mathrm{diag}(\sigma_1^2, \ldots, \sigma_I^2), \end{aligned} \tag{2.12}$$

i.e. that U is the matrix of eigenvectors of ρ. Hence the best possible states to retain are the m largest eigenvalue eigenstates of ρ, or equivalently the m most probable eigenstates of ρ.

If the system is in a mixed state with probabilities W_k,[5]

$$\big|\psi\big\rangle = \sum_k W_k \big|\psi^k\big\rangle, \tag{2.13}$$

each $\big|\psi^k\big\rangle$ can be written as in Eq. (2.1), and the relevant error measure accordingly

$$S = \sum_k W_k \sum_{ij} \Big(\psi_{ij}^k - \sum_{\alpha=1}^{m} a_\alpha^k u_i^\alpha v_j^{k,\alpha}\Big)^2. \tag{2.14}$$

[4] Note that $\psi^\dagger\psi$ is the RDM for the environment block.

[5] To use finite temperatures W_k is normalized Boltzmann weights [2], p. 39.

We seek a *single set of optimal states*, hence not allowing u_i^α to depend on k, while the environment states are allowed to change with k.

The reduced density matrix is

$$\rho_{ii'} = \sum_k W_k \sum_j \psi_{ij}^k (\psi^k)_{ji'}^\dagger, \tag{2.15}$$

and a similar optimization procedure gives

$$U^\dagger \rho U = \mathrm{diag}(\sigma_1^2, \cdots, \sigma_I^2), \tag{2.16}$$

where

$$\sigma_i^2 = \sum_k W_k (a_i^k)^2, \tag{2.17}$$

so that the optimal states again are the largest eigenvalue eigenstates of the reduced density matrix, defined in Eq. (2.15).

In conclusion we have shown that the $m < I$ optimal DMRG states are the m largest eigenvalue eigenstates of the reduced density matrix as properly defined in Eq. (2.2) and (2.15).

2.1.1 Efficiency

It is clear from the above derivation of the DMRG states that success of DMRG is intimately connected with the spectrum of the reduced density matrix. For fixed number of DMRG states m, the error of truncation is larger if many eigenvalues of ρ are approximately equal, as compared to when a few eigenvalues dominate. In fact one can use the sum of the truncated eigenvalues as a guideline to the magnitude of the truncation error at each step, although it does not tell anything about the *actual* error in observables.

Thus DMRG performs best if the spectrum of eigenvalues of the RDM decays rapidly. When the decay becomes slower a larger number of states must be kept to maintain precision and when this number becomes too large precision can no longer be maintained and eventually DMRG fails.

For certain exactly solvable models it is possible to show analytically that the spectrum of the RDM decays exponentially explaining the good performance of DMRG in these cases. Also it should be noted that the boundary conditions influence the spectrum of the RDM and generally DMRG performs substantially worse for systems with periodic rather than open boundary conditions [2], p. 41. Hence most often better precision is obtained using larger systems with open BCs as compared to a small system with periodic BCs.

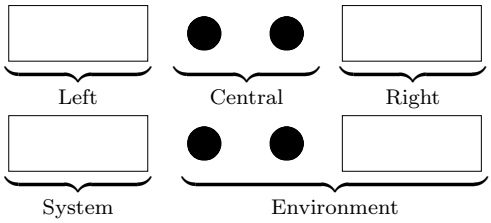

Figure 2.2: Generic superblock configuration and the nomenclature used in this work. We use both notations, and use m to denote the number of states in the truncated basis for the system block throughout this thesis.

2.2 Algorithms

To implement the idea of optimizing the basis we need algorithms for building up a system from a sufficiently small size and for improving the description of a given finite system. In this section we describe how the superblock procedure is combined with the DMRG projection, leading to the two important DMRG algorithms.

In order not to truncate too heavily at each step the usual way of adding degrees of freedom is to add one site at a time, hence building up the system from a very small size in a controlled manner. A site means either a site in a quantum lattice system or any other generic and sufficiently small building block of the Hilbert space. The key idea is to divide the system into 4 blocks, a left/system block, two central blocks, typically being single sites, and a right block. The central and right blocks constitute the environment block, as illustrated in Fig. 2.2.

There are two generically different algorithms, the *infinite* and the *finite* system algorithms differing by the choice of environment block. In the following only ground state properties are targeted, although it is possible to target also excited states or multiple states at the same time, as shown in the previous section. We use the terminology of a one-dimensional system, although this is not strictly necessary.[6] Any block, superblock, system block etc., is defined entirely by matrix representations of the Hamiltonian and other relevant operators in the current basis. Hence in the following the phrase *"...form the superblock..."* means construct the Hamiltonian and other operators for the superblock in the current basis.

2.2.1 Infinite system algorithm

In the infinite system algorithm the system is enlarged one site at a time. As environment block the simplest and most common choice is to use two

[6] DMRG has been successfully applied to two-dimensional systems, see e.g. [9] and references therein.

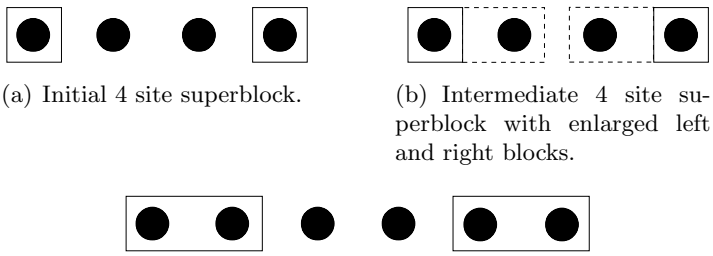

(a) Initial 4 site superblock.

(b) Intermediate 4 site superblock with enlarged left and right blocks.

(c) 6 site superblock.

Figure 2.3: Superblock configurations in the first DMRG step.

single sites joined with a spatial reflection of the system block, as seen in Fig. 2.3. The superblock size thus grows by two sites at each step – giving rise to the name 'infinite system algorithm'. The algorithm is:

1. Form a superblock consisting of L sites, where L is small enough that the ground state of the superblock Hamiltonian can be computed exactly. In Fig. 2.3(a) the case $L = 4$ is shown.

2. Compute the ground state of the superblock Hamiltonian H_L^{super} numerically.

3. From the ground state, in general the target state(s), construct the reduced density matrix ρ, defined in Eq. (2.2), for the *new* system block, i.e. the system block obtained when the leftmost central site has been added, as seen in Fig. 2.3(b).

4. Diagonalize the reduced density matrix ρ obtaining the m most probable eigenstates. The value of m should be chosen sufficiently large to make the calculation accurate and sufficiently small to make superblock matrices manageable on the computers available. Collect the m column vectors u_α in the truncation matrix $O = (u_1, u_2, \cdots, u_m)$. Note that usually a full diagonalization of ρ is fastest since many eigenstates are needed.

5. Denoting by index l the last site in the old system block, $l = 1$ in Fig. 2.3(b), construct the Hamiltonian H_{l+1} and other operators A_{l+1} in the new system block, and transform them to the eigenbasis of the reduced density matrix by $\bar{H}_{l+1} = O_L^\dagger H_{l+1} O_L$, and $\bar{A}_{l+1} = O_L^\dagger A_{l+1} O_L$.

6. Form a superblock of size $L+2$ using $\bar{H}_{l+1}$, two single sites, and $\bar{H}_{l+1}^R$, Fig. 2.3(c). Note that the right block is the spatial reflection of the left block.

7. Repeat this procedure using this new superblock, defined by the Hamiltonian H_{L+2}^{super}, as input to step 2.

In the first few steps it is possible to have m larger than the total number of states in the system. In such cases one should keep all eigenstates of ρ, and the truncation reduces to a shift of basis.

Using the infinite system algorithm the superblock can be built two sites at the time from a small size in a controlled manner. These iterations can either be continued to approximate the infinite system limit, or stopped when the desired superblock size has been reached. Note that in step 2 it is essential to compute *only* the target state(s) and *not* perform a full diagonalization of the superblock Hamiltonian.

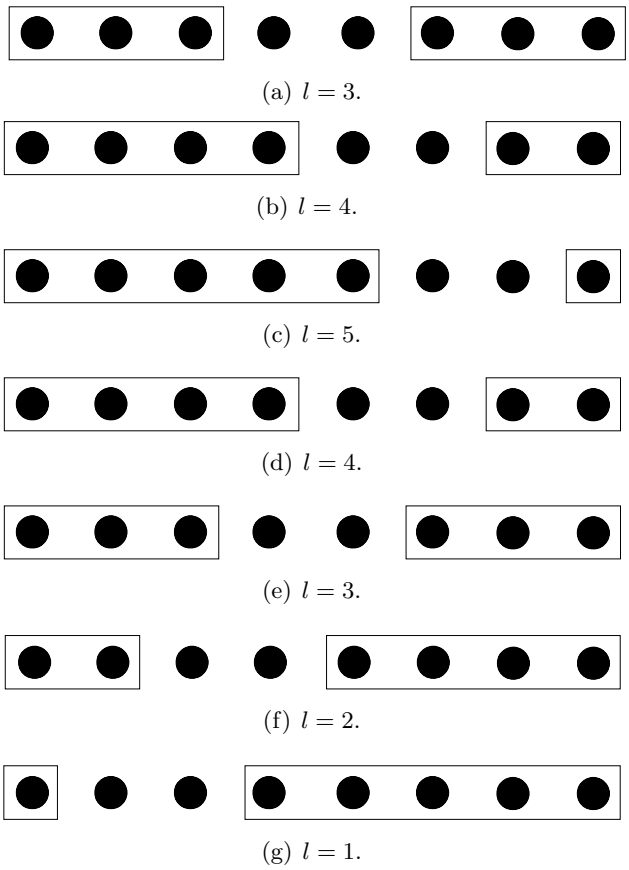

(a) $l = 3$.

(b) $l = 4$.

(c) $l = 5$.

(d) $l = 4$.

(e) $l = 3$.

(f) $l = 2$.

(g) $l = 1$.

Figure 2.4: Superblock configurations for fixed superblock length, $L = 8$, in the initial left to right and right to left phases.

2.2.2 Finite system algorithm

Once a superblock of the desired size has been built one can choose the environment block in a different way. Keeping the superblock size fixed, the point of division between the two blocks can be moved back and forth

through the superblock improving the accuracy of the description at each such sweep. The algorithm is:

1. Use the infinite system algorithm to build up a superblock of the desired size L storing at each step the left and right block Hamiltonians and operators relevant to connect these blocks. Also matrices for observables A should be stored at each step.

2. Carry out steps 3-5 in the infinite system algorithm, computing $\bar{H}_{l+1}$ and $\bar{A}_{l+1}$, l being the point of division as illustrated in Fig. 2.4. Store $\bar{H}_{l+1}$ and $\bar{A}_{l+1}$.

3. Form a superblock of unchanged size L using $\bar{H}_{l+1}$, two single sites and $\bar{H}^R_{l-1}$. Note that $\bar{H}^R_{l-1}$ was found and stored during the build up of the initial superblock using the infinite system algorithm.

4. Repeat steps 2-3 until $l = L - 3$. The above constitutes the left to right phase in which the left block is enlarged, illustrated in Fig. 2.4(a)-2.4(c).

5. Reverse the roles of left and right and move the point of division all the way through the superblock until $l = 1$. This is the right to left phase, in which the right block is enlarged, illustrated in Fig. 2.4(c)-2.4(g).

6. Reverse the roles of left and right again, and repeat this 'zipping' back and forth until convergence is reached.

The left to right phase improves the description of the left block, while the right to left phase improves the description of the right block. When the calculation has converged the iterations are usually stopped when the left and right blocks are of equal size. Specific examples of these two algorithms are given in Chap. 3, 4, and 5.

2.2.3 Diagonalization routine

The largest matrices encountered in DMRG are the superblock matrices. A major part of the calculational time is spent computing the ground state of the superblock, or generally the target states. Hence it is essential to use an efficient algorithm. In addition, since only the ground state – or at least a very limited number of low lying eigenstates – of the Hamiltonian are needed it is essential not to perform a full diagonalization since this is unnecessary and time consuming. Iterative diagonalization schemes like the Lanczos and Davidson algorithms are well suited for these purposes and implementations exist for many different programming languages.

It should be noted that it is possible to eliminate the need of constructing the full superblock Hamiltonian by incorporating a special diagonalization routine [2], p. 47.

2.3 Symmetries and commutators

Preserving symmetries of the system is essential for a successful truncated description. The DMRG optimization process consists of multiple truncations and basis changes, and hence it is relevant to check if any symmetries are unintentionally broken during these operations. Having a symmetry operator S operating only on the system part of the superblock, the relevant check is

$$[\rho_{\text{system}}, S] \;=\; 0, \tag{2.18}$$

where '0' is a zero-matrix of the same size as ρ_{system} and S [10]. Also it can be useful to perform other checks such as (anti)commutators between bosonic (fermionic) operators.

These checks should be performed at each step of the DMRG algorithm. If they are not sufficiently fulfilled it is necessary to keep more states, i.e. use larger m. Hence these checks aid in determining how many states it is necessary to keep in order to describe the system accurately. The degree to which these checks should be satisfied varies between models and implementations, and some checks are more vital than others depending on what observables we wish to describe accurately. These points should be investigated using benchmark results to verify the precision of the DMRG within the model and parameter values chosen.

2.4 Speeding up the calculation

A number of schemes to speed up the basic DMRG algorithms described above have been proposed, and in this section we consider a few.

2.4.1 Quantum numbers

Identification of good quantum numbers can be used to speed up the DMRG calculation substantially. In one-dimensional systems with short range interactions the matrix representations of operators contain mostly zeros. The basis states of each block (system and environment) may be labelled and sorted according to good quantum numbers, which leaves non-zero entries of most matrices in rectangular submatrices. Depending on the matrix in question these submatrices may either connect states with the same set of quantum numbers (i.e. square submatrices on the diagonal) or connect states with different sets of quantum numbers (rectangular off-diagonal submatrices). Hence, instead of working with large sparse matrices it is possible to work with a set of smaller dense matrices. This is the optimal way to store the data, since only non-zero elements are stored, reducing memory requirements. Also finding the ground state of the superblock becomes computa-

tionally easier, since we may compute the ground state of a smaller dense Hamiltonian matrix rather than the large sparse Hamiltonian matrix.

Sorting the superblock states according to quantum numbers additionally allows one to seek the ground state within a given set of quantum numbers, e.g. particle number or total spin, while working with the entire superblock Hilbert space would always compute the total ground state.

2.4.2 Wavefunction transformations

A large part of the total calculational time in the DMRG scheme is used computing the ground state of the superblock, and therefore it is very important to use an efficient algorithm.

In DMRG convergence to the *actual* ground state of the current Hamiltonian is vital since the basis is optimized for the target state. Hence convergence to a different state would optimize the basis to describe this state rather than the ground state. Most algorithms for finding eigenvectors and eigenvalues use a random vector as starting point for an iterative diagonalization scheme. Thus to ensure convergence to the actual ground state of the Hamiltonian, and not a different low lying eigenstate, a large number of iterative steps are needed, making the computation lengthy.

One solution to this problem is to have a good initial guess to the actual ground state. This ensures that not very many iterations are necessary as well as ensuring convergence to the actual ground state. And such a guess can indeed be found in the finite system algorithm – using the ground state from the previous step. To incorporate this initial guess in the DMRG scheme the ground state wavefunction of the *previous* step has to be shifted to the current basis using the transformation matrices from the previous DMRG step. Hence the transformation matrices should be stored at each step increasing storage requirements somewhat.

2.4.3 Varying number of retained states

Another way to speed up the calculation is to use a varying number of retained states throughout the calculation. The idea is to build up the system and let the finite system algorithm converge using m_0 states. Upon convergence the number of states kept is increased to $m_1 > m_0$ and the finite system algorithm is iterated until convergence is achieved again. One can then increase the number of states even further if sufficient precision has not yet been obtained.

By varying m in this way the time spent on the infinite system algorithm becomes less and we spend most time on the finite system algorithm. When the finite system algorithm is used the precision of the infinite system sweep is less critical and hence the calculation is not too sensitive to the number of states kept in the build up of the system. Hence the optimal strategy is to

use a relatively small number of states in the build up, and then increase m rather fast once convergence has been reached in the finite system algorithm.

2.5 Observables and measurements

DMRG is an indirect method in which operators are known only through their matrix representations. The basic DMRG is only suitable for static quantities but several schemes to obtain dynamic quantities using DMRG have been proposed in the literature [2, 5, 6, 7]. In the following subsections we show how to obtain expectation values of static operators and a simple Lanczos method of obtaining expectation values of dynamic correlators.

2.5.1 Static quantities

Expectation values of any static operator A that can be expressed in the original basis are fairly easy to calculate. One has to construct and update the matrix representing the operator at each DMRG step and these matrices should be stored if the finite system algorithm is used.

After the final DMRG step one should have matrix representations of A and the target state $|\psi\rangle$ in the current optimized DMRG basis. The expectation value can then be found as in Eq. (2.5),

$$\begin{aligned} \langle\psi|\, A\, |\psi\rangle &= \mathrm{Tr}[\rho A] \\ &= \mathrm{Tr}\big[\psi^\dagger A \psi\big] \\ &= \sum_{i,i',j} \psi^\dagger_{ji} A_{ii'} \psi_{i'j}, \end{aligned} \tag{2.19}$$

where ψ is the target state matrix defined in Eq. (2.1). This product gives one scalar, the expectation value, for each target state and the evaluation gives the numerically *exact* expectation value for the approximate eigenstate.

Alternatively one can obtain expectation values directly from the *vector* representation of $|\psi\rangle$,

$$\big\langle\psi\big|A\big|\psi\big\rangle = \sum_{kl} \psi^*_k A_{kl} \psi_l, \tag{2.20}$$

where now ψ is the column ground state vector, and A is any operator in the basis of the *full* superblock. In App. A we show that the two methods in Eq. (2.19) and (2.20) yield identical results for any system operator, and thus the difference amounts to different organizations of the same data.

The evaluation of correlators often involve operators applied to different parts of the system. Thus we may have to evaluate the expectation value of an operator $A = B \cdot C$, where B operates on one part of the superblock and C operates on another. Let $|i\rangle$ be states in the system block and $|j\rangle$ be

states in the environment block. The state of the system may be written in product form

$$|\psi\rangle = \sum_{i'j'} \psi_{i'j'} \big|i'\big\rangle \big|j'\big\rangle, \tag{2.21a}$$

$$\langle\psi| = \sum_{ij} \langle j| \langle i| \psi^\dagger_{ji}, \tag{2.21b}$$

so that if B and C operate on the system and environment blocks respectively the expectation value of A is

$$\begin{aligned} \langle\psi| A |\psi\rangle &= \sum_{i,i',j,j'} \big\langle\, i\big|\, B\, \big|i'\big\rangle \big\langle\, j\big|\, C\, \big|j'\big\rangle \psi^\dagger_{ji} \psi_{i'j'} \\ &= \sum_{i,i',j,j'} \psi^\dagger_{ji} B_{ii'} C_{jj'} \psi_{i'j'}. \end{aligned} \tag{2.22}$$

If, however, B and C operate on the same block one should notice that

$$\sum_{i,i',i'',j} \psi^\dagger_{ji} B_{ii'} C_{i'i''} \psi_{i''j} \neq \langle\psi| A |\psi\rangle . \tag{2.23}$$

The sum over i' runs over the truncated basis set and should really run over a complete set. Instead one should treat the combined operator as *one* operator and construct and update matrices for $[B \cdot C]$ throughout the calculation and then evaluate

$$\langle\psi| A |\psi\rangle = \sum_{i,i',j} \psi^\dagger_{ji} \left[B \cdot C\right]_{ii'} \psi_{i'j}, \tag{2.24}$$

to obtain the correct expectation value. Notice that Eq. (2.24) is identical to Eq. (2.19) for the combined operator $A = B \cdot C$.

Using these relations it is fairly easy to obtain averages of operators if they can be constructed in the initial basis. One simply updates the matrix representations exactly the same way as the Hamiltonian and other operators are updated, and when DMRG has converged use Eq. (2.19), (2.20), or (2.22) to find expectation values. Which of the two methods is most conveniently used depends on how data is represented in the implementation. Specific examples of the calculation of observables using both methods are given in Chap. 3, 4, and 5.

2.5.2 Dynamic quantities

One scheme to calculate expectation values of dynamic operators was proposed by Wang, Hallberg, and Naef [2]. Following their ideas we show how to obtain dynamic quantities in the zero temperature limit.

For any approximate ground state $|\psi_0\rangle$ of the Hamiltonian H we may construct an orthogonal basis in a Lanczos procedure. We specialize to calculating fermionic correlators

$$C(t) \;=\; \langle\psi_0|\,\{A^\dagger(t), A(0)\}\,|\psi_0\rangle\,. \tag{2.25}$$

We usually seek the Fourier transform

$$C(\omega) \;=\; \int_{-\infty}^{\infty} dt\; e^{i\omega t}\,\langle\psi_0|\,\{A^\dagger(t), A(0)\}\,|\psi_0\rangle\,, \tag{2.26}$$

and inserting the Heisenberg time evolution we find

$$\begin{aligned} C(\omega) \;&=\; \int_{-\infty}^{\infty} dt\; e^{i\omega t}\,\langle\psi_0|\,\{e^{iHt}A^\dagger e^{-iHt}, A\}\,|\psi_0\rangle \\ &=\; \langle\psi_0|\,A^\dagger \int_{-\infty}^{\infty} dt\; e^{i(\omega+E_0-H)t}A + A\int_{-\infty}^{\infty} dt\; e^{i(\omega-E_0+H)t}A^\dagger\,|\psi_0\rangle \\ &=\; 2\pi\,\langle\psi_0|\,A^\dagger\delta(\omega+E_0-H)A + A\delta(\omega-E_0+H)A^\dagger\,|\psi_0\rangle\,. \end{aligned} \tag{2.27}$$

Additionally we use the identity

$$\frac{1}{x+i\eta} = \frac{1}{x} - i\pi\delta(x), \quad \eta\to 0^+, \tag{2.28}$$

to rewrite the δ-functions

$$\delta(\omega\pm(E_0-H)) \;=\; -\frac{1}{\pi}\lim_{\eta\to 0^+}\mathrm{Im}\frac{1}{\omega\pm(E_0-H)+i\eta}, \tag{2.29}$$

so that

$$\begin{aligned} &C(\omega) = \\ &\quad -2\lim_{\eta\to 0^+}\mathrm{Im}\,\langle\psi_0|\,A^\dagger\frac{1}{\omega+E_0-H+i\eta}A + A\frac{1}{\omega-E_0+H+i\eta}A^\dagger\,|\psi_0\rangle\,, \end{aligned} \tag{2.30}$$

or finally using the notation

$$G^+(z) \;=\; \langle\psi_0|\,A(z+H)^{-1}A^\dagger\,|\psi_0\rangle\,, \tag{2.31a}$$

$$G^-(z) \;=\; \langle\psi_0|\,A^\dagger(z-H)^{-1}A\,|\psi_0\rangle\,, \tag{2.31b}$$

we find

$$C(\omega) \;=\; -2\lim_{\eta\to 0^+}\mathrm{Im}\left(G^-(\omega+E_0+i\eta)+G^+(\omega-E_0+i\eta)\right). \tag{2.32}$$

We start the Lanczos procedure by defining

$$|f_0\rangle \;=\; \begin{cases} A\,|\psi_0\rangle\,, \\ A^\dagger\,|\psi_0\rangle\,, \end{cases} \tag{2.33}$$

and iterate to find further Lanczos vectors,

$$|f_{n+1}\rangle \;=\; H\,|f_n\rangle - a_n\,|f_n\rangle - b_n^2\,|f_{n-1}\rangle\,, \tag{2.34}$$

where $n \geq 0$, $b_0 = 0$, and $\langle f_n | f_m \rangle = 0$ for $n \neq m$ as shown explicitly in App. B. The coefficients are

$$a_n \;=\; \frac{\langle f_n|\,H\,|f_n\rangle}{\langle f_n|f_n\rangle}, \tag{2.35a}$$

$$b_n^2 \;=\; \frac{\langle f_n|f_n\rangle}{\langle f_{n-1}|f_{n-1}\rangle}. \tag{2.35b}$$

In order to reexpress the Green's functions Eq. (2.31) we first define an orthonormal basis

$$|n\rangle \;=\; \frac{|f_n\rangle}{\sqrt{\langle f_n\,|f_n\rangle}}. \tag{2.36}$$

Using Eq. (2.34) the Hamiltonian applied to the basis state $|n\rangle$ is

$$\begin{aligned} &H\,|n\rangle = \\ &\sqrt{\frac{\langle f_{n+1}\,|f_{n+1}\rangle}{\langle f_n\,|f_n\rangle}}\,|n+1\rangle + a_n\,|n\rangle + b_n^2\sqrt{\frac{\langle f_{n-1}\,|f_{n-1}\rangle}{\langle f_n\,|f_n\rangle}}\,|n-1\rangle\,, \end{aligned} \tag{2.37}$$

and using the notation

$$\sqrt{\frac{\langle f_m\,|f_m\rangle}{\langle f_n\,|f_n\rangle}} \;=\; n_{m,n}, \tag{2.38}$$

we find the matrix elements

$$\begin{aligned} \langle m|\,H\,|n\rangle \;&=\; n_{n+1,n}\delta_{m,n+1} + a_n\delta_{m,n} + b_n^2 n_{n-1,n}\delta_{m,n-1} \\ &= \begin{cases} n_{n+1,n}, & m = n+1, \\ a_n, & m = n, \\ b_n^2 n_{n-1,n}, & m = n-1. \end{cases} \end{aligned} \tag{2.39}$$

Thus by construction the Hamiltonian is tri-diagonal in the Lanczos basis

$$(z \pm H)_n \;=\; \begin{pmatrix} z \pm a_0 & \pm b_1^2 n_{0,1} & 0 & \cdots & 0 \\ \pm n_{1,0} & z \pm a_1 & \pm b_2^2 n_{1,2} & & \vdots \\ 0 & \pm n_{2,1} & z \pm a_2 & & 0 \\ \vdots & & & \ddots & \pm b_n^2 n_{n-1,n} \\ 0 & \cdots & 0 & \pm n_{n,n-1} & z \pm a_n \end{pmatrix}. \tag{2.40}$$

First we rewrite Eq. (2.31) as

$$\begin{aligned} G^{\pm}(z) &= \langle f_0|(z \pm H)^{-1}|f_0\rangle \\ &= \sum_{mm'} \langle f_0|m\rangle\langle m|(z \pm H)^{-1}|m'\rangle\langle m'|f_0\rangle \\ &= \sum_{mm'} \frac{\langle f_0|f_m\rangle}{\sqrt{\langle f_m|f_m\rangle}}\langle m|(z \pm H)^{-1}|m'\rangle\frac{\langle f_{m'}|f_0\rangle}{\sqrt{\langle f_{m'}|f_{m'}\rangle}} \\ &= \langle f_0|f_0\rangle\langle 0|(z \pm H)^{-1}|0\rangle. \end{aligned} \tag{2.41}$$

Hence we need to find the first element of the inverse of the matrix $(z \pm H)$ in the basis of Eq. (2.36).[7] In order to invert the matrix in Eq. (2.40) we first consider the solution to 2nd order in the coefficients a_i and b_i^2

$$\begin{aligned} (z \pm H)_1 &= \begin{pmatrix} z \pm a_0 & \pm b_1^2 n_{0,1} \\ \pm n_{1,0} & z \pm a_1 \end{pmatrix} \Rightarrow \\ \langle 0|[(z \pm H)_1]^{-1}|0\rangle &= \frac{[C_1]_{(1,1)}}{\det(z \pm H)_1}, \end{aligned} \tag{2.42}$$

where $[C_1]_{(1,1)}$ is the complement of $[(z \pm H)_1]_{(1,1)}$, given by the subdeterminant, in this case just a scalar,

$$[C_1]_{(1,1)} = z \pm a_1, \tag{2.43}$$

so that to this order

$$\begin{aligned} \langle 0|[(z \pm H)_1]^{-1}|0\rangle &= \frac{z \pm a_1}{(z \pm a_0)(z \pm a_1) - b_1^2 n_{0,1} n_{1,0}} \\ &= \frac{1}{z \pm a_0 - \frac{b_1^2}{z \pm a_1}}, \end{aligned} \tag{2.44}$$

where we used that $n_{i,i+1}n_{i+1,i} = 1$.

Next we consider the solution to $(n+1)$'st order in the coefficients a_i and b_i^2, given by a very similar expression,

$$\langle 0|[(z \pm H)_n]^{-1}|0\rangle = \frac{[C_n]_{(1,1)}}{\det(z \pm H)_n}, \tag{2.45}$$

with the complement given by the subdeterminant

$$\begin{aligned} [C_n]_{(1,1)} &= \begin{vmatrix} z \pm a_1 & \pm b_2^2 n_{1,2} & 0 & \cdots & 0 \\ \pm n_{2,1} & z \pm a_2 & \pm b_3^2 n_{2,3} & & \vdots \\ 0 & & & & 0 \\ \vdots & & & \ddots & \pm b_n^2 n_{n-1,n} \\ 0 & \cdots & 0 & \pm n_{n,n-1} & z \pm a_n \end{vmatrix} \\ &\equiv \det(2:n), \end{aligned} \tag{2.46}$$

[7] See e.g. [11] for details on inverting matrices.

which defines the notation $\det(2:n)$ for the subdeterminant of $(z \pm H)_n$ in Eq. (2.46). Extending in the obvious way the usage of this notation we have

$$\left\langle 0\middle|[(z \pm H)_n]^{-1}\middle|0\right\rangle \;=\; \frac{\det(2:n)}{\det(1:n)}. \tag{2.47}$$

The full determinant can be rewritten

$$\begin{aligned}
\det(1:n) \;&=\; (z \pm a_0)\det(2:n) \\
&\quad \mp b_1^2 n_{0,1} \begin{vmatrix} \pm n_{1,0} & \pm b_2^2 n_{1,2} & 0 & \cdots & 0 \\ 0 & z \pm a_2 & \pm b_3^2 n_{2,3} & & \vdots \\ 0 & & & & 0 \\ \vdots & & & \ddots & \pm b_n^2 n_{n-1,n} \\ 0 & \cdots & 0 & \pm n_{n,n-1} & z \pm a_n \end{vmatrix} \\
&=\; (z \pm a_0)\det(2:n) - b_1^2 n_{0,1} n_{1,0} \det(3:n) \\
&=\; (z \pm a_0)\det(2:n) - b_1^2 \det(3:n),
\end{aligned} \tag{2.48}$$

and hence we find

$$\begin{aligned}
\left\langle 0\middle|[(z \pm H)_n]^{-1}\middle|0\right\rangle \;&=\; \frac{\det(2:n)}{(z \pm a_0)\det(2:n) - b_1^2 \det(3:n)} \\
&=\; \frac{1}{z \pm a_0 - b_1^2 \frac{\det(3:n)}{\det(2:n)}}.
\end{aligned} \tag{2.49}$$

Due to the tri-diagonal structure of the Hamiltonian matrix in Eq. (2.40) we can rewrite any fraction $\det(m+1:n)/\det(m:n)$ in a completely similar way,

$$\begin{aligned}
\frac{\det(m+1:n)}{\det(m:n)} \;&=\; \frac{\det(m+1:n)}{(z \pm a_{m-1})\det(m+1:n) - b_m^2 \det(m+2:n)} \\
&=\; \frac{1}{z \pm a_{m-1} - b_m^2 \frac{\det(m+2:n)}{\det(m+1:n)}}.
\end{aligned} \tag{2.50}$$

Hence by successive use of Eq. (2.50) and using Eq. (2.41) we find the final solution for arbitrary n, in particular $n \to \infty$,

$$G^+(z) \;=\; \frac{\langle\psi_0|\, AA^\dagger \,|\psi_0\rangle}{z + a_0 - \cfrac{b_1^2}{z + a_1 - \cfrac{b_2^2}{z + \cdots}}}, \tag{2.51a}$$

$$G^-(z) \;=\; \frac{\langle\psi_0|\, A^\dagger A \,|\psi_0\rangle}{z - a_0 - \cfrac{b_1^2}{z - a_1 - \cfrac{b_2^2}{z - \cdots}}}. \tag{2.51b}$$

The condition for this method to be feasible is that the continued fractions in Eq. (2.51) converge using a finite and manageable number of Lanczos coefficients a_i and b_i^2. If very many coefficients are needed it becomes difficult to maintain the accuracy.

In principle this procedure is independent of the method used to find the ground state [12]. In a DMRG implementation of the method above there are however technical details that need attention. The DMRG basis is usually heavily truncated compared to the complete basis. The truncation is performed to optimally describe the target state, usually the ground state. The basis may therefore not be suitable for describing excitations in the system, making it impossible to accurately describe dynamical quantities in this basis.

This apparent incompatibility can be remedied by including exited states as target states. As was pointed out by Hallberg the first few Lanczos vectors are candidates for such additional target states [13]. Hence the new normalized target states become

$$\left|\psi^l\right\rangle \;=\; \begin{cases} \left|\psi_0\right\rangle, & l=1, \\ \dfrac{\left|f_{l-2}\right\rangle}{\left\langle f_{l-2}\middle|f_{l-2}\right\rangle}, & l=2,3,\cdots,M, \end{cases} \tag{2.52}$$

and the reduced density matrix accordingly

$$\rho_{ii'} \;=\; \sum_{l=1}^{M} p_l \psi^l_{ij} (\psi^l)^\dagger_{ji'}, \tag{2.53}$$

where p_l is the weight for target state $\left|\psi^l\right\rangle$ and $\sum p_l = 1$ to maintain the normalization.

With these additional target states excitations can be described using a standard DMRG implementation. The additional calculations amount to computing and including as target states at each step M normalized Lanczos vectors, given the ground state $|\psi_0\rangle$, the Hamiltonian H, and the operator A or $A^\dagger$. Since the precision of DMRG generally decreases when more target states are included the optimal value of M has to be determined from case to case. Including more states improves the description of excitations but lowers the general precision of DMRG.

2.6 General comments

DMRG is an approximate method, which restricts the complete Hilbert space of the particular model considered to make computations less demanding. From the derivation of the DMRG states it is clear that the method is variational of nature and that no perturbative series is used. Thus arbitrary strongly correlated systems may be treated using DMRG.

However one cannot always expect completely monotonous convergence in energy due to the fact that the variational procedure optimizes the *basis* of the target state. Thus the description of the target state improves at each

step while the energy is not necessarily lowered [14]. Also it should be noted that the ground state energy of the superblock depends on the configuration of the superblock, i.e. the relative size of the left and right blocks.

In DMRG the strength of the truncation is given entirely by m, and in general increasing m increases the accuracy of the description. Hence there is full control over the truncation and the severity can be checked by increasing m. A monotonous increase in the precision is therefore naively expected for increasing m, and when m equals the total number of states in the system no truncation is performed. In the limit of keeping all system states DMRG is conceptually meaningless since we might as well use exact diagonalization techniques, and the above statements are only included to emphasize the correspondence between m and the degree of truncation.

There is one exception however, when degeneracies of the spectrum of the reduced density matrix exist. Such degeneracies correspond to symmetries of the Hamiltonian and hence all the degenerate states should be kept. As an example Caprara and Rosengren argues that spin triplets manifest themselves in this way and that all degenerate states of the reduced density matrix therefore must be kept [10].

Finally it should be noted that the range of interactions is closely related to the dimensionality of lattice systems. Any two or tree-dimensional lattice system with short range interactions can be mapped onto a sufficiently long one-dimensional system with long range interactions. Hence one might naively expect that such systems could be treated in the DMRG framework. This is not the case as it turns out that the calculational time grows rapidly with the width of quasi-one-dimensional systems making such simple approaches unfeasible. Similarly the calculational time grows rapidly when interactions become longer ranged. It should however be noted that DMRG has been successfully applied to two-dimensional systems, using more sophisticated approaches [9].

Chapter 3

Hubbard model

To understand in more detail how DMRG works we implemented it on the one-dimensional Hubbard chain, describing fermions confined to a one-dimensional chain consisting of sites, on which there can be 0, 1, or 2 spinful electrons.

In this chapter we review our implementation of DMRG and use it to calculate low energy properties of the Hubbard chain for various lengths and couplings, both in zero and finite magnetic field. In the non-interacting limit we compare the DMRG ground state energy to corresponding analytic results and find good consistency. We briefly comment on the results found and conclude the chapter with a discussion of the limitations of our implementation.

3.1 Hamiltonian and matrices

In order to limit our study of the Hubbard model we have focused on calculations at half filling. The usual Hubbard term $Un_{i\uparrow}n_{i\downarrow}$ does not ensure this since it does not treat empty and doubly occupied sites equally, and thus the chemical potential depends on the value of U. To ensure half filling we use the Hamiltonian

$$H \;=\; -t\sum_{i=1}^{L-1}\sum_{\sigma=\uparrow,\downarrow}\left(c_{i\sigma}^{\dagger}c_{i+1\sigma}+c_{i+1\sigma}^{\dagger}c_{i\sigma}\right)+U\sum_{i=1}^{L}\left(1-N_i\right)^2, \qquad (3.1)$$

where $N_i = n_{i\uparrow} + n_{i\downarrow}$, and where the term $(1-N_i)^2$ ensures that states with $N_i = 1$ are energetically favorable compared to $N_i = 0$ and $N_i = 2$.

The basis used for the sites is $|0\rangle$, $|\uparrow\rangle \equiv c_{\uparrow}^{\dagger}|0\rangle$, $|\downarrow\rangle \equiv c_{\downarrow}^{\dagger}|0\rangle$, and $|\uparrow\downarrow\rangle \equiv c_{\uparrow}^{\dagger}c_{\downarrow}^{\dagger}|0\rangle$. In this basis the matrix representation of annihilation operators $c_{i\sigma}$, the number operator N_i, the total z-spin operator S_i^z, and the on-site

repulsion Hamiltonian H_U for the single sites are

$$c_{i\uparrow} = \begin{pmatrix} 0 & 1 & 0 & 0 \\ 0 & 0 & 0 & 0 \\ 0 & 0 & 0 & 1 \\ 0 & 0 & 0 & 0 \end{pmatrix}, \tag{3.2a}$$

$$c_{i\downarrow} = \begin{pmatrix} 0 & 0 & 1 & 0 \\ 0 & 0 & 0 & -1 \\ 0 & 0 & 0 & 0 \\ 0 & 0 & 0 & 0 \end{pmatrix}, \tag{3.2b}$$

$$N_i = \begin{pmatrix} 0 & 0 & 0 & 0 \\ 0 & 1 & 0 & 0 \\ 0 & 0 & 1 & 0 \\ 0 & 0 & 0 & 2 \end{pmatrix} = c_{i\uparrow}^\dagger c_{i\uparrow} + c_{i\downarrow}^\dagger c_{i\downarrow}, \tag{3.2c}$$

$$S_i^z = \begin{pmatrix} 0 & 0 & 0 & 0 \\ 0 & \frac{1}{2} & 0 & 0 \\ 0 & 0 & -\frac{1}{2} & 0 \\ 0 & 0 & 0 & 0 \end{pmatrix}, \tag{3.2d}$$

$$H_U = U \begin{pmatrix} 1 & 0 & 0 & 0 \\ 0 & 0 & 0 & 0 \\ 0 & 0 & 0 & 0 \\ 0 & 0 & 0 & 1 \end{pmatrix}. \tag{3.2e}$$

These operators have to be expressed in the basis of several sites. Electrons anticommute and hence we must keep track of the number of electrons 'to the left of' any given anticommuting operator, provided a numbering of the basis states. We use the obvious numbering given by the site numbers. This bookkeeping is done using a matrix counting the number of particles on each site, and returning a sign in accordance. For the single site this matrix is

$$P_i = \begin{pmatrix} 1 & 0 & 0 & 0 \\ 0 & -1 & 0 & 0 \\ 0 & 0 & -1 & 0 \\ 0 & 0 & 0 & 1 \end{pmatrix}. \tag{3.3}$$

In App. C we demonstrate in further detail the properties of P in relation to anticommutation of fermionic operators.

Denoting fermionic operators by f and bosonic operators by b we enlarge the basis by performing Kronecker tensor products,

$$\tilde{f}_1 = f_1 \otimes \delta_2, \tag{3.4a}$$

$$\tilde{f}_2 = P_1 \otimes f_2, \tag{3.4b}$$

$$\tilde{b}_1 = b_1 \otimes \delta_2, \tag{3.4c}$$

$$\tilde{b}_2 = \delta_1 \otimes b_2, \tag{3.4d}$$

where e.g. $\tilde{b}_1$ means operator b_1 in the enlarged basis of sites 1 and 2. This illustrates the use of matrix P.

Hermiticity of H

The Hamiltonian operator is hermitian, and thus also the matrix representation should be. Throughout DMRG calculations we find that the Hamiltonian matrix indeed is hermitian – apart from numerical imprecisions on the scale of the machine working precision ($\sim 10^{-16}$). Some sparse matrix diagonalization routines require complete hermiticity of the matrices. Having ensured it was only numerical imprecisions preventing the Hamiltonian from being hermitian, i.e. checking that

$$\max(H - H^\dagger) \;\sim\; 10^{-16}, \tag{3.5}$$

we use the substitution,

$$\frac{H + H^\dagger}{2} \;\rightarrow\; H. \tag{3.6}$$

to ensure hermiticity. This forces *any* matrix to be hermitian, and therefore it is *absolutely crucial to ensure that only numerical imprecisions are eliminated this way.* If the Hamiltonian turns out to be far from hermitian something else is wrong, and using this trick prevents such errors from displaying themselves directly and leads to wrong or imprecise results.

3.2 Symmetries

Preserving symmetries of the Hamiltonian is essential. We have incorporated two symmetry checks at each step of the algorithm,

$$\left[\rho, N^L\right] \;=\; 0, \tag{3.7a}$$
$$\left[\rho, S_z^L\right] \;=\; 0, \tag{3.7b}$$

as well as various anticommutation checks, e.g.

$$\left\{c_{l,\sigma}, c_{l,\sigma}^\dagger\right\} \;=\; 1, \tag{3.8a}$$
$$\left\{c_{l,\sigma}, c_{l+1,\sigma}^\dagger\right\} \;=\; 0, \tag{3.8b}$$

where l denotes the rightmost site of the left block, and '0' and '1' are zero and identity matrices respectively.

These checks are performed after each truncation in the DMRG calculation. This is not completely trivial since these checks are never completely fulfilled. In this implementation the degree to which these checks are satisfied depends crucially on the parameter values chosen. Usually the checks are

fulfilled within $10^{-8} - 10^{-12}$, remarkably being worst in the non-interacting limit where we often find values as high as 10^{-6}, which is probably close to the lower acceptable limit of precision in order for the DMRG calculations to be precise. Keeping more states would improve this but also make the calculational time longer. It is worth noting that much DMRG work reported use significantly higher number of states kept than we have been able to.

3.3 Infinite system sweep

The DMRG procedure is started by constructing the Hamiltonian and other operators for a four site superblock. As illustrated in Eq. (3.4) the basis is enlarged by performing Kronecker tensor products. The Hamiltonian for sites 1 and 2 is constructed first,

$$\begin{aligned} H_{12} &= H_U \otimes \delta_2 + \delta_1 \otimes H_U \\ &\quad -t \sum_\sigma \left[\left(c^\dagger_{1\sigma} \otimes \delta_2\right)\left(P_1 \otimes c_{2\sigma}\right) + \left(P_1 \otimes c^\dagger_{2\sigma}\right)\left(c_{1\sigma} \otimes \delta_2\right) \right], \end{aligned} \tag{3.9}$$

where the first line represents the on-site repulsions and the second line represents the hopping between sites 1 and 2. Note the usage of matrix P_1 to maintain anticommutation of fermionic operators.

Other relevant operators are

$$S^z_{12} = S^z_1 \otimes \delta_2 + \delta_1 \otimes S^z_2, \tag{3.10a}$$
$$P_{12} = P_1 \otimes P_2, \tag{3.10b}$$
$$c^L_\sigma = P_1 \otimes c_{2\sigma}, \tag{3.10c}$$
$$N_{12} = N_1 \otimes \delta_2 + \delta_1 \otimes N_2, \tag{3.10d}$$

representing the total z-component of the spin, the fermionic sign operator, the annihilation operator for the rightmost site, and the number operator for two sites respectively. Note that c^L_σ is needed to connect the left block to the leftmost central site. All matrices in the combined Hilbert space of sites 1 and 2 have dimensions 16×16.

Completely analogous expressions exist for the right block. Hence we may construct the Hamiltonian and other operators for the four site superblock, shown in Fig. 3.1(a),

$$\begin{aligned} H_{1234} &= H_{12} \otimes \delta_{34} + \delta_{12} \otimes H_{34} \\ &\quad -t \sum_\sigma \left(((c^L_\sigma)^\dagger \otimes \delta_{34})(P_{12} \otimes c^R_\sigma) + (P_{12} \otimes (c^R_\sigma)^\dagger)(c^L_\sigma \otimes \delta_{34}) \right), \end{aligned} \tag{3.11}$$

where c^R_σ is the annihilation operator for the leftmost site in the right block, and where the second line in Eq. (3.11) is the hopping between the left and right blocks.

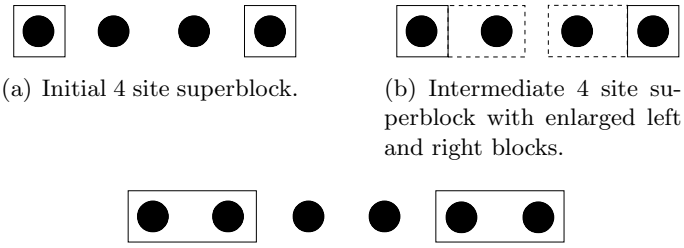

(a) Initial 4 site superblock.

(b) Intermediate 4 site superblock with enlarged left and right blocks.

(c) 6 site superblock.

Figure 3.1: Superblock configurations in the first infinite system DMRG step.

Usually there is no truncation at this point since the Hilbert space is sufficiently small to be handled exactly. However to illustrate the DMRG scheme we do so anyway. The first step is to compute the ground state eigenvector of the Hamiltonian, denoted H_{1234} above, currently a 256×256 sparse matrix. We use Lanczos solver `laneig`[1] or Davidson solver `jdqr`[2] for MatLab.

Denoting the generic element of the ground state vector v_α,

$$|\psi\rangle \;=\; (v_1, \cdots, v_{256})\,, \tag{3.12}$$

the ground state matrix for the new left system, consisting of sites 1 and 2 as in Fig. 3.1(b), is constructed as

$$\psi \;=\; \begin{array}{c} \\ |0,0\rangle \\ |0,\uparrow\rangle \\ \vdots \\ |\uparrow\downarrow,\uparrow\downarrow\rangle \end{array} \begin{array}{c} \begin{array}{cccc} |0,0\rangle & |0,\uparrow\rangle & \cdots & |\uparrow\downarrow,\uparrow\downarrow\rangle \end{array} \\ \begin{pmatrix} v_1 & v_2 & \cdots & v_{16} \\ v_{17} & v_{18} & & v_{32} \\ \vdots & & \ddots & \vdots \\ v_{240} & v_{241} & \cdots & v_{256} \end{pmatrix} \end{array}, \tag{3.13}$$

where the rows correspond to the complete basis for sites 1 and 2, and the columns correspond to the complete basis for sites 3 and 4. Note that e.g. v_{16} corresponds to the basis vector $|0,0,\uparrow\downarrow,\uparrow\downarrow\rangle \equiv |0,0\,\rangle|\uparrow\downarrow,\uparrow\downarrow\rangle$.

The reduced density matrix (RDM) for the left subsystem is given by

$$\rho_L \;=\; \psi\psi^\dagger. \tag{3.14}$$

DMRG instructs us to retain the most probable eigenstates of the RDM. In this model however N^L and ${S_z}^L$ are symmetries, which can be demonstrated as follows: Let $|\psi_N\rangle$ be the state vector of the superblock for given fixed particle number N

$$|\psi_N\rangle \;=\; \sum_{\alpha,\beta} \psi_{\alpha\beta}\,|n_\alpha\rangle\,|n_\beta\rangle\,, \tag{3.15}$$

[1] `http://soi.stanford.edu/~rmunk/PROPACK/`.

[2] `http://www.math.uu.nl/people/sleijpen/index.html`.

where $|n_\alpha\rangle$ and $|n_\beta\rangle$ are states of the system and environment block respectively, and labeled by their particle numbers. Obviously we have $N = n_\alpha + n_\beta$, and thus given N and n_β also n_α is fixed. The reduced density matrix is

$$\rho_{\alpha\alpha'} \;=\; \sum_\beta \psi_{\alpha\beta}\psi^\dagger_{\beta\alpha'} \tag{3.16}$$

which implies that $|n_\alpha\rangle$ and $|n_{\alpha'}\rangle$ are states with the same particle number, and hence $\left[\rho, N^L\right] = 0$. Similar arguments apply for S_z^L.

Thus we may choose simultaneous eigenstates of ρ_L, N^L, and ${S_z}^L$, by computing eigenvectors of

$$\bar{\rho}_L \;=\; \rho_L + r_1 N^L + r_2 {S_z}^L, \quad r_i \in]0,1]. \tag{3.17}$$

The eigenvalues of ρ_L are then found by $U^\dagger \rho_L U$, where U is the matrix of eigenvectors found above. With this procedure we ensure that the particle number and spin remains good quantum numbers for the DMRG basis we construct, thus keeping matrices N^L and S_z^L diagonal.

Diagonalizing $\bar{\rho}_L$ and collecting the m retained column eigenvectors, denoted by u_α, in a matrix,

$$O \;=\; (u_1, u_2, \cdots, u_m)\,, \tag{3.18}$$

we can truncate and shift to the retained eigenbasis of ρ_L. The block Hamiltonian and all operators needed to reconstruct the superblock Hamiltonian are shifted to this basis,

$$\tilde{H}_1 \;=\; O^\dagger H_{12} O, \tag{3.19a}$$
$$\tilde{c}^L_\sigma \;=\; O^\dagger c^L_\sigma O, \tag{3.19b}$$
$$\tilde{P}_L \;=\; O^\dagger P_L O, \tag{3.19c}$$
$$\tilde{A} \;=\; O^\dagger A O, \tag{3.19d}$$

where A is the matrix representation of *any* operator working on the left block. Truncating in a similar fashion the right block, retaining eigenstates of ρ_R, we obtain $\tilde{H}_4$ and $\tilde{c}^R_\sigma$. Renaming $\tilde{H}_1 \to H_1$, $\tilde{c}^L_\sigma \to c^L_\sigma$, $\tilde{P}_L \to P_L$, $\tilde{H}_4 \to H_4$, and $\tilde{c}^R_\sigma \to c^R_\sigma$ we have a truncated description of the enlarged left and right blocks in Fig. 3.1(b).

Truncated left block matrices H_1, c^L_σ, and P_L, and the corresponding truncated right block matrices, should be stored for use in the finite system algorithm. We store additionally matrices for N^L and S^L_z in order to calculate these quantum numbers for the final state. If other observables are to be found matrices representing those have to be stored as well.

Using the truncated block matrices the Hamiltonian of a superblock consisting of 6 sites can be constructed. The left and right blocks of this

superblock contains two sites each and are represented in a *truncated* basis by H_1 and H_4, and the two central sites are represented in their full real space basis. The superblock is shown in Fig. 3.1(c).

This setup is formally identical to the initial having matrices for the left and right block and for the two central sites, and hence we may repeat all the above steps. We iterate in this way until the chain reaches the desired length, increasing the superblock chain length by two sites at each iteration.

3.4 Finite system sweeps

Once the superblock reaches the desired length L all matrices for the right and left block being up to half the total length should be stored on disk or in memory. At the onset of the finite system algorithm the superblock consists of a left and right block, each consisting of $L/2-1$ sites and represented in a truncated basis, and two central sites each represented in their full real space basis.

Once the superblock Hamiltonian has been constructed the basic step is similar to the infinite system method. Taking the left to right sweep as an example the basic DMRG step is:

1. Compute the ground state of the superblock Hamiltonian.
2. Construct the RDM ρ_L for the *new* left block, consisting of the *old* left block, initially of length $L/2-1$, and the leftmost central site.
3. Diagonalize ρ_L.
4. Find the retained eigenbasis by keeping the m most probable eigenstates of ρ_L.
5. Transform all *left* matrices to the eigenbasis of ρ_L and store them.
6. Construct a new superblock Hamiltonian, consisting of the *new* truncated left block, two central sites, and a new right block containing one site less. At the first finite system step the length of the new left block is $L/2$, and the length of the new right block is $L/2-2$. Matrices defining the new right block were found and stored during the infinite system sweep.

This prescription is repeated using the *new* superblock as input until the point of division has been moved all the way through the chain. The basic right to left step is identical to the above reversing the roles of left and right. Each finite system sweep improves the description of the block that is enlarged during the sweep.

Having obtained convergence by sweeping back and forth through the chain the algorithm is stopped when the left and right blocks are of equal

size. It is not always obvious when convergence has been reached – but one usable measure is the change in ground state energy from sweep to sweep. Note however that the energy is not necessarily monotonously decreasing, as discussed in Sect. 2.6. Typically we iterate 4-6 times and iterating further does not improve the description.

3.4.1 Varying number of retained states

Our calculations on the Hubbard model uses the infinite as well as the finite system algorithms. We have experimented with retaining different number of states in the calculation, as described in Sect. 2.4.3. In the infinite system sweep (the build up of the system) we retain $m = 10$ states, which makes the build up very fast for the system sizes we have used. Once the system has been built we iterate the finite system algorithm 5 times using $m = 10$, ensuring convergence with this number of states kept. Then we increase m to the final value, typically $m = 24$, and iterate until convergence has been reached, usually around 5 times.

In our implementation we use multidimensional arrays to store matrices for the left and right blocks, and in MatLab these are non-sparse and declared with a given fixed size. Thus to retain different number of states in the calculation we need at least two storage arrays increasing memory requirements.

In general we find lower ground state energies when we use $m = 24$ in the whole calculation. Also we find that the precision of the infinite system algorithm does indeed depend on the number of states kept, hence we cannot really justify using $m = 10$ when building up the system and have therefore used constant m in all calculations presented in this thesis.

It should be noted that we use a significantly smaller number of states than in most DMRG results reported in the literature. The above conclusions may depend heavily on m and should therefore be viewed as conclusions for our implementation only; they are *not* general statements.

3.5 Computing the ground state

The superblock contains basis states corresponding to many different quantum numbers, e.g. particle number and spin. Often a target state of a given particle number is desired, and hence such a subspace of the total Hilbert space has to be picked out. The most time consuming part of the algorithm is computing the ground state, and since such subspaces are often substantially smaller than the full Hilbert space the overall effect is a speed up of the total calculation.

We have specialized to calculating at half filling using a Hamiltonian operator that ensures this, cf. Eq. (3.1). This *does not* imply that the basis used only contains states at exactly half filling. Rather it means that the

ground state is a half filled state. In our calculations it would therefore suffice to simply compute the ground state of the entire Hamiltonian matrix. But taking into account the speed up of the ground state calculation explained above we still use a subspace calculation.

Instead of picking out the subspace completely and working with a smaller dense matrix we have chosen to (temporarily) set entries of the superblock Hamiltonian to zero before the diagonalization, hence creating a much sparser Hamiltonian. In doing so the total DMRG calculation becomes up to 10 times faster in our implementation.

3.6 Magnetic field

In order to split the spin degeneracy present in the Hubbard model we have included a small magnetic field in the z-direction. The extra term in the site Hamiltonian is

$$H_h \;=\; -h \sum_{i=1}^{L} (S_z)_i \,, \tag{3.20}$$

with the corresponding matrix representation

$$H_h \;=\; -\frac{h}{2} \begin{pmatrix} 0 & 0 & 0 & 0 \\ 0 & 1 & 0 & 0 \\ 0 & 0 & -1 & 0 \\ 0 & 0 & 0 & 0 \end{pmatrix} . \tag{3.21}$$

As h is turned up the ground state energy of the system is changed but for very small h, of the order $t/100$, the energy is essentially unchanged.

Due to the spin-splitting for non-zero h symmetries and anticommutation relations are fulfilled to much greater extent, which can be understood as follows: The risk of breaking the spin-flip symmetry by the truncation of the Hilbert space is eliminated once the symmetry itself is eliminated. Thus there is one less constraint on the number of states kept, reflecting itself in the symmetry and anticommutator checks.

Also the calculation of the total spin on the chain changes as a consequence of non-zero h. Without a magnetic field the spin states were energy degenerate. Thus the state of the superblock can be an arbitrary superposition of a 'spin up' and a 'spin down' state, giving an arbitrary total S_z depending on the weight between these states. Due to the spin-splitting effect of non-zero h the total spin on the chain becomes half-integer, as is clearly observed in our DMRG calculations.

3.7 Expectation values

In this section we explain how expectation values of various operators are obtained in this implementation of DMRG. Having constructed and updated matrices for the total particle number and spin throughout the DMRG calculation it is fairly easy to obtain expectation values of these operators.

At the end of the DMRG routine we have matrix representations of the operators we want to find expectation values for, in the current DMRG basis, as well as a ground state vector found from the current Hamiltonian. The left and right blocks are described by m DMRG states, and hence the superblock basis consists of $16m^2$ states. Taking the *total* particle number of the superblock as an example we find expectation values in either of the two ways considered in Sect. 2.5.

Denoting the matrix representation of the particle number operator of the superblock N

$$N \;=\; N_{\text{system}} \otimes \delta_{\text{environment}} + \delta_{\text{system}} \otimes N_{\text{environment}}, \tag{3.22}$$

we find the total particle number by the vector-matrix-vector multiplication

$$\big\langle \psi_0 \big| N \big| \psi_0 \big\rangle \;=\; \psi_0^\dagger N \psi_0, \tag{3.23}$$

where ψ_0 is the $16m^2$ component column ground state vector and N is the $16m^2 \times 16m^2$ matrix in Eq. (3.22).

Obtaining the particle number of the system block itself can be done in two ways. Either you expand the representation of the number operator for the system to the basis of the superblock by,

$$\tilde{N}_{\text{system}} \;=\; N_{\text{system}} \otimes \delta_{\text{environment}}, \tag{3.24}$$

and then proceed as above,

$$\big\langle \psi_0 \big| N_{\text{system}} \big| \psi_0 \big\rangle \;=\; \psi_0^\dagger \tilde{N}_{\text{system}} \psi_0, \tag{3.25}$$

where $\tilde{N}_{\text{system}}$ is the $16m^2 \times 16m^2$ matrix in Eq. (3.24) and ψ_0 is the $16m^2$ component ground state vector.
Alternatively we may use

$$\langle \psi_0 |\, N_{\text{system}} \,| \psi_0 \rangle \;=\; \text{Tr} \left[\; \underline{\underline{\psi_0}}^\dagger N_{\text{system}} \underline{\underline{\psi_0}} \; \right], \tag{3.26}$$

where now $\underline{\underline{\psi_0}}$ is the $m \times m$ matrix given in Eq. (3.13) and N_{system} is the $m \times m$ matrix representation of the number operator for the system.

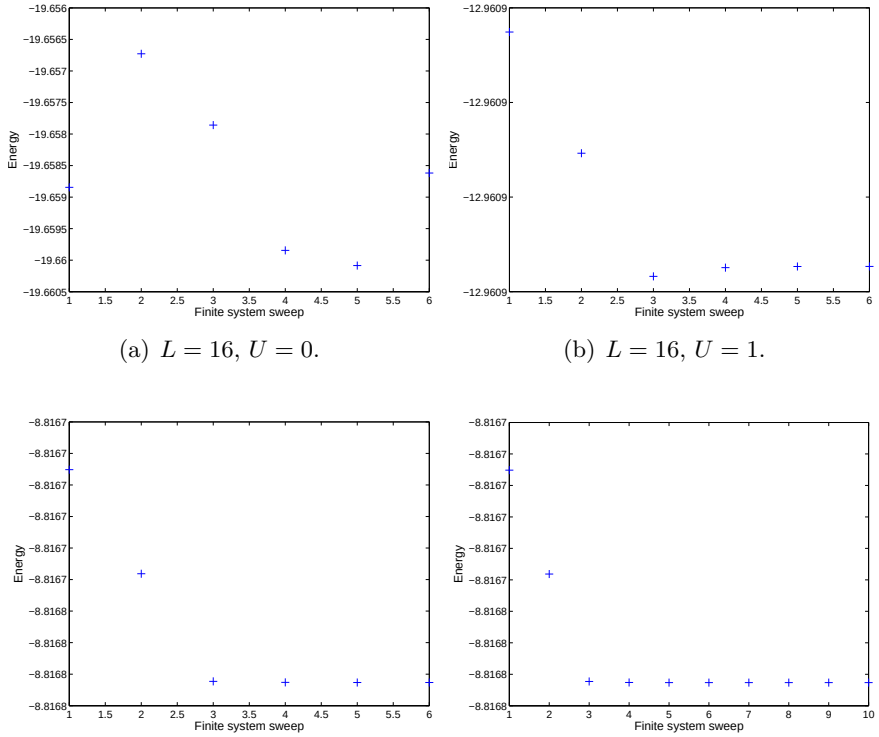

(a) $L = 16$, $U = 0$.

(b) $L = 16$, $U = 1$.

(c) $L = 16$, $U = 2$.

(d) $L = 16$, $U = 2$.

Figure 3.2: Convergence of the ground state energy as a function of the finite system sweep number. Notice the non-monotonous convergence in energy when $U = 0$. DMRG calculations performed using $m = 24$ states.

3.8 Results

Using the implementation described above we have obtained results for the ground state energy, particle number, and spin of the complete superblock as well as for the system block. We have targeted only the ground state but for the final superblock we have calculated properties of exited states as well. The description of exited states is therefore not expected to be as accurate as the ground state.

There are odd-even oscillations in the properties of the system, i.e. they depend on wether there is an odd or even number of sites in the system. The superblock always consists of an even number of sites and hence does not exhibit this kind of behavior. Plots of the ground state energy of the superblock as function of the finite system iteration number are shown in Fig. 3.2. As can be seen the effect of the finite system sweeps is limited, which is surprising since Noack and White comments that most often this is not the case [2], p. 44. Notice also the non-monotonous decrease in energy

in Fig. 3.2(a).

We see two possible explanations for the small improvement using the finite system algorithm: (*i*) We retain a quite small number of states. Most work reported use much larger m, and Noack and White argues that the infinite system algorithm is relatively insensitive to the number of states kept [2]. We expect this statement to be valid *only* for sufficiently large values of m since very small values would truncate *too* heavily in the build up of the system. (*ii*) We calculate at half filling, which is a special particle-hole symmetric filling. This introduces symmetries in the Hamiltonian, possibly influencing the DMRG calculation.

3.8.1 Fixed U

Keeping the on-site repulsion U fixed and varying the length of the chain L we have calculated the energy, total particle number, and total spin for the lowest five eigenstates of the superblock. In Fig. 3.3 and 3.4 we have plotted $E_i(L)/L$, $N_i(L)$, and $S_z^i(L)$ for $U = 0.5$ and $U = 2$ both with and without a magnetic field, $h = 0$ and $h = 1/100$, and using $m = 24$ states in DMRG calculations. These figures show that the behavior of the Hubbard chain does not change qualitatively when the chain length is changed.

3.8.2 Fixed L

For fixed chain length L and varying on-site repulsion U we have performed DMRG calculations of the energy, total spin, and total particle number for the ground state and four lowest exited states of the superblock. In Fig. 3.5 we have plotted $E_i(U)$, $N_i(U)$, and $S_z^i(U)$ using chainlengths $L = 20$ and $L = 40$, $h = 1/100$, and $m = 24$ states in DMRG calculations. These figures reveal the effect of increasing on-site interaction and as expected exited states becomes number degenerate with the ground state for sufficiently large U.

3.8.3 Eigenspectrum of ρ

We have computed the eigenspectrum of the enlarged system block at the last step in the DMRG calculation for $L = 12$, $L = 14$, $L = 16$, and $L = 20$ for different couplings both with and without a magnetic field. From the ground state vector the reduced density matrix for the enlarged left system consisting of the left block and the leftmost central site has been calculated and the complete set of eigenvalues found. The result is seen in Fig. 3.6, and indeed the eigenspectrum decays rather fast. Note that in the generic DMRG step we truncate to $m = 24$ states.

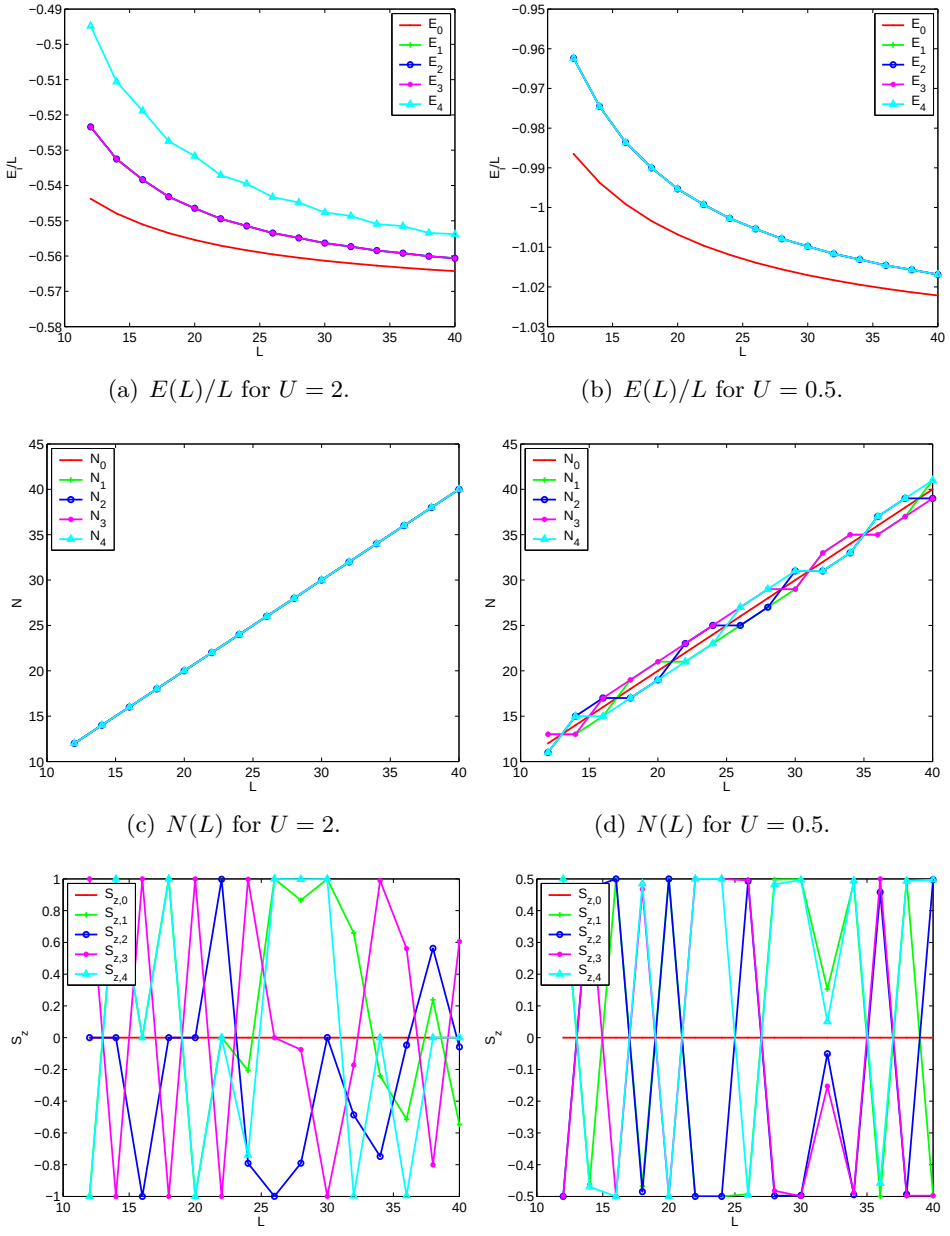

(a) $E(L)/L$ for $U = 2$.

(b) $E(L)/L$ for $U = 0.5$.

(c) $N(L)$ for $U = 2$.

(d) $N(L)$ for $U = 0.5$.

(e) $S_z(L)$ for $U = 2$.

(f) $S_z(L)$ for $U = 0.5$.

Figure 3.3: Lowest 5 states, $E_i(L)/L$, $N_i(L)$, and $S_z^i(L)$ for $h = 0$. Qualitatively the properties of the Hubbard chain is independent of the chainlength. DMRG calculations performed using $m = 24$ states.

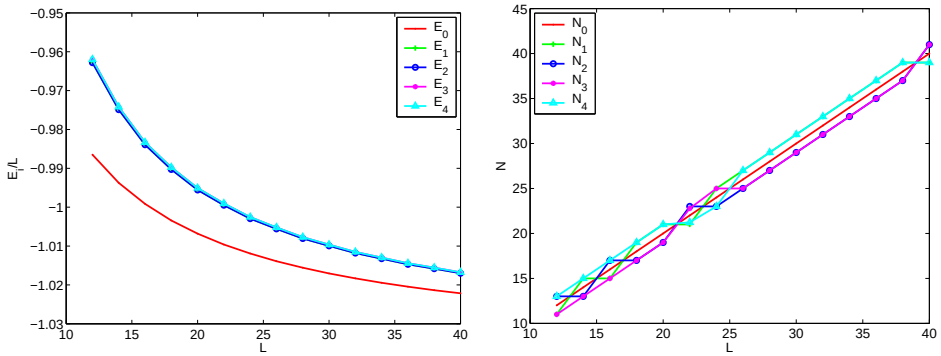

(a) $E(L)/L$. (b) $N(L)$.

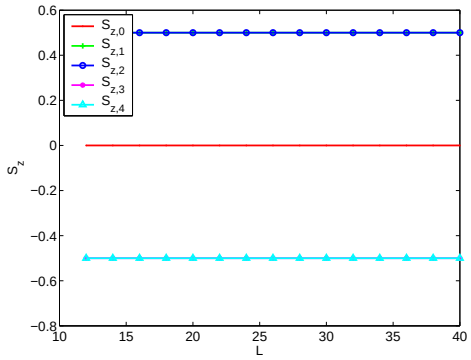

(c) $Sz(L)$.

Figure 3.4: Lowest 5 states, $E_i(L)/L$, $N_i(L)$, and $S_z^i(L)$ for $U = 0.5$ and $h = 1/100$. Notice the strictly half-integer spin. DMRG calculations preformed using $m = 24$ states.

3.9 Interpretation

The phase diagram of the Hubbard model is in general rich and contains many different regions. It is not the purpose of this thesis to analyze in detail the Hubbard model. We will limit ourselves to a few comments on the data calculated using our DMRG implementation.

We have limited our implementation to a narrow band around half filling. More specifically we ensured a half filled ground state by the choice of Hamiltonian but allowed for exited states to be away from half filling. At half filling and zero magnetic field the ground state is a spinles state, $S_z = 0$. Considering exited states we are able to see the 'competition' between double occupancy, costing energy U, and flipping spins, which eliminates hopping possibilities and thus costs energy t. We outline a few features.

Large U limit: In the large U limit the lowest exited states are number

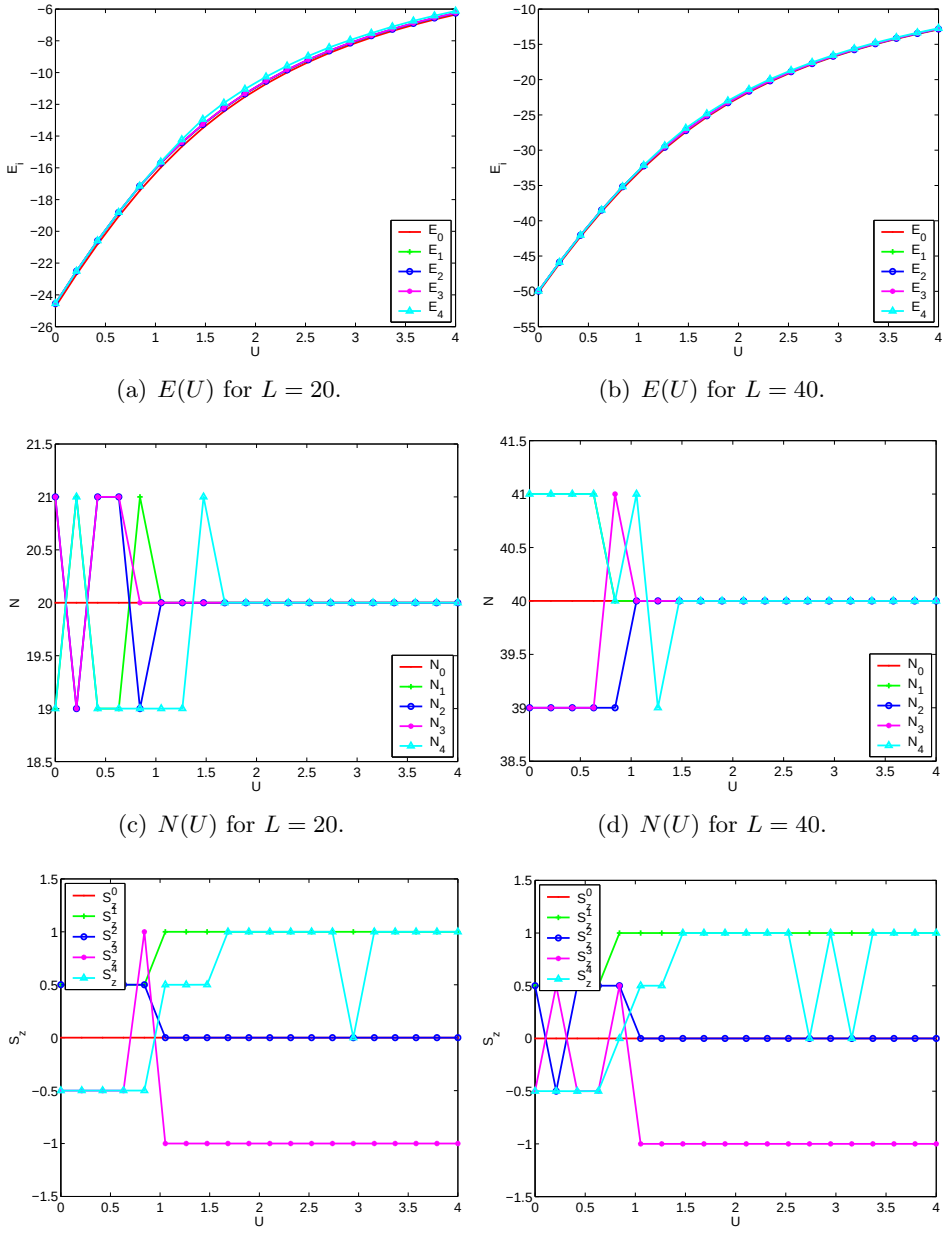

(a) $E(U)$ for $L = 20$.

(b) $E(U)$ for $L = 40$.

(c) $N(U)$ for $L = 20$.

(d) $N(U)$ for $L = 40$.

(e) $S_z(U)$ for $L = 20$.

(f) $S_z(U)$ for $L = 40$.

Figure 3.5: Lowest 5 states, $E_i(U)$, $N_i(U)$, and $S_z^i(U)$ for $h = 1/100$. Sufficiently large U makes exited states number degenerate with the ground state. DMRG calculations performed using $m = 24$ states.

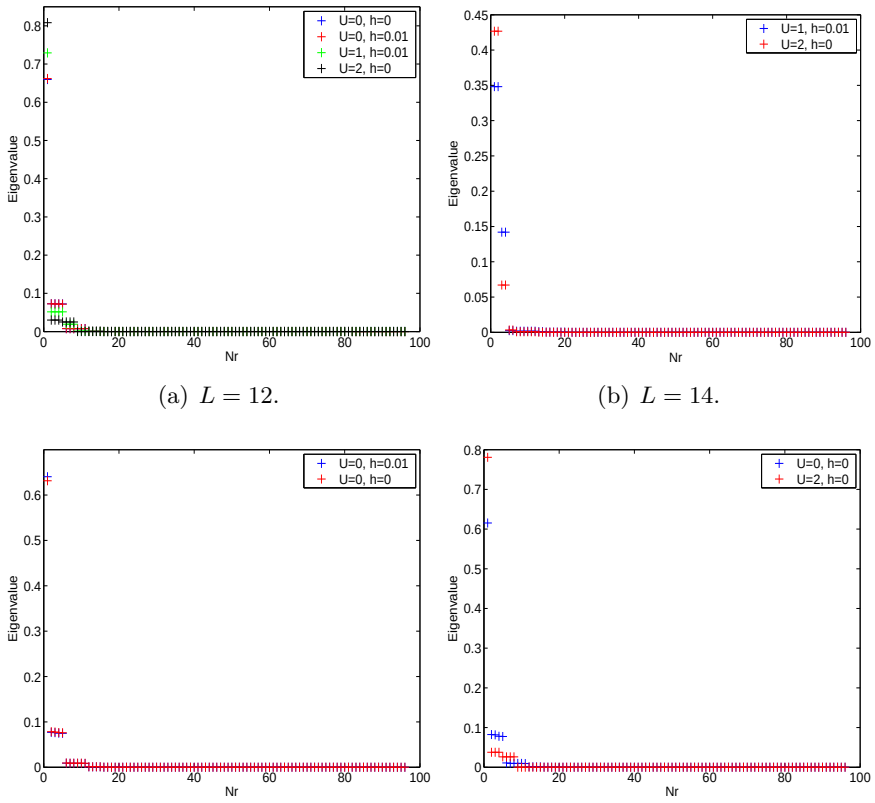

(a) $L = 12$. (b) $L = 14$.

(c) $L = 16$. (d) $L = 20$.

Figure 3.6: Eigenspectrum for various lengths and on-site interactions. Notice that a very limited number of eigenvalues dominate and very many are essentially zero. DMRG calculations performed using $m = 24$ states such that we usually truncate to 24 states.

degenerate with the ground state due to the large energy cost of leaving half filling, giving always doubly occupied or empty sites. For chainlengths $L = 20$ and $L = 40$ this kind of behavior is clearly observed, as seen in Fig. 3.5(c) and 3.5(d), and this behavior seems to be independent of the chainlength, Fig. 3.3(c). In this limit the lowest exited states differ from the ground state by having one or more spins flipped.

Length dependence: Qualitatively the properties of the Hubbard chain are independent of the length of the chain, which is clearly seen in Fig. 3.3 and 3.4. The very similar properties of chainlengths $L = 20$ and $L = 40$ in Fig. 3.5 further demonstrate this.

Magnetic field: Including a magnetic field, $h \neq 0$, breaks the spin symmetry, revealed in several ways. Firstly the total spin on the superblock

becomes half-integer, as seen in Fig. 3.4(c), 3.5(e), and 3.5(f). With no magnetic field there are two degenerate ground states and the eigenroutine finds and arbitrary superposition of the two, possibly giving non-half-integer spins.

Secondly for non-zero h the lowest exited states tend to have positive superblock spin since this is the preferred direction given by the magnetic field.

3.10 Analytic result

As benchmark for the performance of DMRG we have calculated numerically exact results in the non-interacting limit $U = 0$. In this limit spin up and down electrons are treated separately. Hence we may construct a Hamiltonian matrix using a single particle spinles basis,

$$H_0 = -t \begin{pmatrix} 0 & 1 & \cdots & 0 \\ 1 & 0 & & \vdots \\ \vdots & & \ddots & 1 \\ 0 & \cdots & 1 & 0 \end{pmatrix}, \tag{3.27}$$

where the dimensions of H_0 is $L \times L$. For the chain lengths we consider full diagonalization of H_0 is possible since the matrix size scales linearly with the system size.

The ground state energy of H_0 at half filling is obtained by diagonalizing and summing up the lowest $L/2$ eigenvalues. Remembering the spinfactor 2 and denoting the eigenvalues e_i we thus find the ground state energy of the spinful non-interacting Hubbard model at half filling

$$E_0 = 2 \sum_{i=1}^{L/2} e_i. \tag{3.28}$$

A few comparisons of the numerically exact results with the corresponding DMRG results are shown in Tab. 3.1, enabling us to benchmark the performance of DMRG in the non-interacting limit. The agreement is very fine, considering that e.g. the 40 site chain is described using approximately 10^4 states, while the entire Hilbert space contains approximately 10^{24} states. So despite the heavily truncated Hilbert space produced by DMRG the ground state properties are still described quite well.

3.11 Limitations and future work

The code produced for the Hubbard model is specialized to calculations near half filling. But this is not the only limitation of our DMRG implementation.

L	Exact	DMRG	$\Delta E/E$
12	-14.5925	-14.5895	$2 \cdot 10^{-4}$
14	-17.1335	-17.0927	$2 \cdot 10^{-3}$
20	-24.7630	-24.7183	$2 \cdot 10^{-3}$
26	-32.3969	-32.3675	$9 \cdot 10^{-4}$
30	-37.4873	-37.4472	$1 \cdot 10^{-3}$
40	-50.2156	-50.1468	$1 \cdot 10^{-3}$

Table 3.1: Comparison of exact and DMRG results for $U = 0$ and $h = 0$. Our implementation yields quite accurate estimates of the ground state energy. DMRG calculations performed using $m = 24$ states.

In this section we consider a few other limitations and discuss possible ways to eliminate these.

Target states: The current code is limited to a narrow band around half filling, always targeting a half filled ground state. We are not able to handle arbitrary fillings or e.g. restraining the spin using our implementation.

Expanding our implementation to treat arbitrary fillings probably implies reorganizing the code to make full use of quantum numbers, which also speeds up the calculation. We expect object oriented languages like C++ or Python to be better suited for this layout than MatLab.

Calculational time: The system size currently accessible is heavily limited by the long calculational time. Many further optimizations of the code can be made, which could improve on this. It would be interesting to rewrite the code in either of the programming languages mentioned above, rethinking the structure of the program. Another potential speedup of the code is the wavefunction transformations described in Sect. 2.4.2, which has not yet been implemented.

Precision: We have not been able to improve the description by increasing the number of states kept in the DMRG. This would most likely enable us to e.g. maintain anticommutation relations to larger extent. It should be noted that most work presented in the literature use larger m than we do – some even use $m \sim 500$.

Likewise we have not been able to really test what values of m gave best results. There may be significant improvements of the precision by increasing or decreasing m moderately, as discussed in Sect. 2.6. We have mainly used $m = 24$ since this is the choice used by M. Andersen *et al.* on a similar setup [15]. Whether this is actually the optimal choice should be checked thoroughly.

Benchmark for $U \neq 0$: So far we have only tested the performance of DMRG in the non-interacting limit. To test DMRG further it would be interesting to compare results also for $U \neq 0$. Simple approximations and perturbative results could be compared where applicable to give a better understanding of DMRG in those limits.

Also we have only benchmarked the ground state energy and verified that DMRG finds a zero spin ground state. It would be interesting to also benchmark properties of exited states to see to what extend these results are reliable. One possible selfconsistency check could be to include a few exited states as target states and see how the results changed. Probably more that $m = 24$ states are needed to maintain sufficient precision in such calculations as the general precision of DMRG decreases when more states are targeted.

3.12 Conclusions

In this chapter we have implemented DMRG on the one dimensional Hubbard model at half filling, giving technical details of the implementation as well as pointing out some difficulties in the implementation. For various chain lengths we have successfully calculated properties of the ground state as well as exited states, more specifically the energy, particle number, and total spin of the states. In the non-interacting limit we have compared DMRG and analytic results and found the DMRG ground state energies very accurate, with relative energy deviations of the order $10^{-3} - 10^{-4}$. To expand the model we included a small magnetic field and made additional calculations. Expected features of the spin splitting are clearly observed in the results. We briefly commented on the results found using our DMRG implementation, and finally we discussed the limitations and future improvements of the implementation.

Chapter 4

Quantum dot with single infinite lead

In recent years quantum dots have received much attention experimentally as well as theoretically, also within DMRG. One example is Berkovits who studies a quantum dot coupled to a single one-dimensional semi-infinite lead using DMRG calculations [16]. In this chapter we follow the work of Berkovits and implement DMRG on this setup, calculating the occupation of the dot versus chemical potential. In the non-interacting limit we work out the occupations analytically using Green's functions and compare to the DMRG results. To extend the capability of our DMRG implementation we attempt to calculate the spectral function of the dot using a simple Lanczos scheme. Finally we comment on results found with our implementation.

4.1 Hamiltonian and matrices

The model considered here is a quantum dot with N_{Dot} levels coupled to a single one-dimensional semi-infinite lead. On the dot there is coulomb interaction – modelled by a repulsion term for double occupancy, the electrons are treated as spinles, and electrons in the leads are assumed to be non-interacting,

$$H_{Dot} = \sum_{i=1}^{N_{Dot}} (\epsilon_i - V_g) a_i^\dagger a_i + U \sum_{i>j}^{N_{Dot}} a_i^\dagger a_i a_j^\dagger a_j, \tag{4.1a}$$

$$H_{Lead} = -t \sum_{j=1}^{\infty} (c_j^\dagger c_{j+1} + c_{j+1}^\dagger c_j), \tag{4.1b}$$

$$H_{DL} = \sum_{i=1}^{N_{Dot}} V_i (a_i^\dagger c_1 + c_1^\dagger a_i), \tag{4.1c}$$

and including a chemical potential μ, the complete Hamiltonian is

$$H = H_{Dot} + H_{Lead} + H_{DL} - \mu\left(\sum_{i=1}^{N_{Dot}} a_i^\dagger a_i + \sum_{j=1}^{\infty} c_j^\dagger c_j\right). \tag{4.2}$$

where a_i represents states in the dot and c_i represents states in the lead.

Electrons are treated as spinles so the real space basis used for the single sites is $\{|0\rangle, |1\rangle\}$. In this basis the basic operators have the following matrix representations

$$a_i = \begin{pmatrix} 0 & 1 \\ 0 & 0 \end{pmatrix}, \tag{4.3a}$$

$$c_i = \begin{pmatrix} 0 & 1 \\ 0 & 0 \end{pmatrix}, \tag{4.3b}$$

$$P_i = \begin{pmatrix} 1 & 0 \\ 0 & -1 \end{pmatrix}, \tag{4.3c}$$

$$N_i = \begin{pmatrix} 0 & 0 \\ 0 & 1 \end{pmatrix} = a_i^\dagger a_i = c_i^\dagger c_i. \tag{4.3d}$$

Matrices P_i and N_i are the fermionic sign operator and the number operator for the single sites respectively.

The basic idea of enlarging the basis is the same as for the Hubbard model considered in Chap. 3. However, here we study the semi-infinite lead limit, eliminating the use of the finite system algorithm, and therefore fewer matrices have to be stored. We specialize our calculations to two dot levels, i.e. $N_{Dot} = 2$.

Hermiticity of H

Just as with the Hubbard model there are numerical imprecisions preventing the Hamiltonian from being completely hermitian. We eliminate these by the replacement

$$\frac{H + H^\dagger}{2} \rightarrow H. \tag{4.4}$$

This enforces hermiticity onto *any* matrix and it should therefore be verified that $\max(H - H^\dagger) \sim 10^{-16}$ before using this replacement, as explained in Sect. 3.1.

4.2 Infinite system sweep

The superblock setup for this system is two quantum dots connected by a one-dimensional lead, i.e. the right block is a spatial reflection of the left,

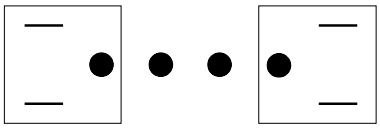

(a) First superblock used in the infinite system sweep.

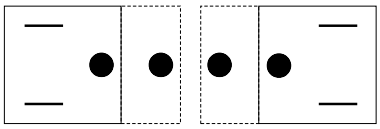

(b) Intermediate superblock with left and right blocks enlarged.

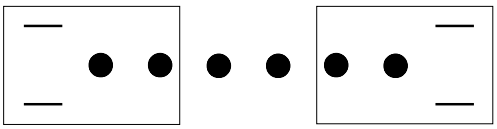

(c) Second superblock used in the infinite system sweep.

Figure 4.1: Superblocks used in the first step of the infinite system algorithm.

as seen in Fig. 4.1. The infinite system sweep is initiated by constructing a left block consisting of the dot and one lead site as seen in Fig. 4.1(a),

$$H_L = H_{Dot} + H_{DL} - \mu\Big(\sum_{i=1}^{2} a_i^\dagger a_i + c_1^\dagger c_1\Big), \tag{4.5a}$$

$$c_L = P_{Dot} \otimes c_1, \tag{4.5b}$$

$$P_L = P_{Dot} \otimes P_1, \tag{4.5c}$$

where it is understood that matrix representations of operators in Eq. (4.5a) are in the enlarged basis of the dot and one lead site, i.e. 8×8 matrices. Note that c_L is the matrix representation of the annihilation operator on the rightmost site in the left block, needed to connect the left block to the first central site.

Additionally matrices for the number operator of the two dot levels are constructed,

$$N_1^{Dot} = N_1 \otimes \delta_2^{Dot} \otimes \delta_1, \tag{4.6a}$$

$$N_2^{Dot} = \delta_1^{Dot} \otimes N_2 \otimes \delta_1, \tag{4.6b}$$

where δ_i^{Dot} denotes a unit matrix in the Hilbert space of dot site i, and δ_j denotes a unit matrix in the Hilbert space of lead site j.

The basic DMRG step is to include an additional site in the lead and truncate to m DMRG states. The enlargement is

$$\begin{aligned}
\tilde{H}_L &= H_L \otimes \delta_2 - \mu\delta_L \otimes N_2 \\
&\quad -t\left(\left(c_L^\dagger \otimes \delta_2\right)\left(P_L \otimes c_2\right) + \left(P_L \otimes c_2^\dagger\right)\left(c_L \otimes \delta_2\right)\right), && \text{(4.7a)}\\
\tilde{c}_L &= P_L \otimes c_2, && \text{(4.7b)}\\
\tilde{P}_L &= P_L \otimes P_2, && \text{(4.7c)}\\
\tilde{N}_i^{Dot} &= N_i^{Dot} \otimes \delta_2, \quad i = 1, 2, && \text{(4.7d)}
\end{aligned}$$

where $-\mu\delta_L \otimes N_2$ is the chemical potential term for site 2 in the lead and $-t\big(\big(c_L^\dagger \otimes \delta_2\big)\big(P_L \otimes c_2\big) + \big(P_L \otimes c_2^\dagger\big)\big(c_L \otimes \delta_2\big)\big)$ is the hopping between sites 1 and 2 in the lead. Similarly $\tilde{H}_R$ and $\tilde{c}_R$ are found and we thus have complete descriptions of the enlarged left and right blocks in Fig. 4.1(b). Note that this step has doubled the size of the Hilbert space for the left and right blocks respectively.

Having computed the ground state of the 4 site superblock in Fig. 4.1(a), currently a 256 component vector,

$$|\psi\rangle = (v_1, v_2, \cdots, v_{256}), \tag{4.8}$$

we construct the RDM for the enlarged left block in Fig. 4.1(b)

$$\psi = \begin{array}{c} \\ |0,0,0,0\rangle \\ |0,0,0,1\rangle \\ \vdots \\ |1,1,1,1\rangle \end{array} \begin{array}{c} \begin{array}{cccc} |0,0,0,0\rangle & |0,0,0,1\rangle & \cdots & |1,1,1,1\rangle \end{array} \\ \begin{pmatrix} v_1 & v_2 & \cdots & v_{16} \\ v_{17} & v_{18} & & v_{32} \\ \vdots & & \ddots & \vdots \\ v_{240} & v_{241} & \cdots & v_{256} \end{pmatrix} \end{array}, \tag{4.9a}$$

$$\rho_L = \psi\psi^\dagger. \tag{4.9b}$$

Note that e.g. the state $|1,1,1,1\rangle$ for the left block means all dot and lead sites in the left block occupied. Diagonalizing ρ_L and keeping m column eigenstates u_α, conveniently collected in a matrix,

$$O = (u_1, u_2, \cdots, u_m), \tag{4.10}$$

we find the new left block matrices in a *truncated basis* by

$$\begin{aligned}
O^\dagger \tilde{H}_L O &\rightarrow H_L, && \text{(4.11a)}\\
O^\dagger \tilde{c}_L O &\rightarrow c_L, && \text{(4.11b)}\\
O^\dagger \tilde{P}_L O &\rightarrow P_L, && \text{(4.11c)}\\
O^\dagger \tilde{N}_i^{Dot} O &\rightarrow N_i^{Dot}, \quad i = 1, 2, && \text{(4.11d)}
\end{aligned}$$

with similar expressions for the right block. Note that if m is larger than the total number of states in the enlarged left block no truncation is performed,

and in that case all eigenstates of ρ_L should be kept. The truncation reduces to a basis shift in those instances.

With these truncated representations of the left and right blocks we may construct the superblock Hamiltonian consisting of the truncated left and right blocks, and two central sites described in their full basis, as shown in Fig. 4.1(c). The truncated left block is represented by the matrices in Eq. (4.11) each being $m \times m$, and hence superblock matrices are in general $4m^2 \times 4m^2$.

This completes the basic step, and we may repeat the above procedure until convergence to the infinite lead limit is reached. It may be difficult to determine when convergence is reached. We have chosen to iterate a fixed and sufficiently large number of times, see also Sect. 4.5.1.

4.3 Computing the ground state

In this setup it is not possible to use the same trick as for the Hubbard model, finding and calculating in the subspace of a given number of particles. Due to the open setup the number of particles in the system is determined by the chemical potential, and thus we cannot restrict the particle number in this setup. Therefore we have to compute the ground state of the entire superblock Hamiltonian rather than in a subspace.

4.4 Expectation values

Expectation values of operators are obtained in either of two ways as explained in Sect. 2.5. At the end of the DMRG calculation the left and right blocks are described by m DMRG states, and hence the superblock basis contains $4m^2$ states. Using the number operator for the dot as an example we find the expectation value

$$\tilde{N}_{Dot} = N_{Dot} \otimes \delta_{\text{environment}}, \tag{4.12a}$$

$$\langle \psi_0 | N_{Dot} | \psi_0 \rangle = \psi_0^\dagger \tilde{N}_{Dot} \psi_0, \tag{4.12b}$$

where $\tilde{N}_{Dot}$ is a $4m^2 \times 4m^2$ matrix and ψ_0 is the $4m^2$ component column ground state vector. Alternatively we may evaluate instead

$$\langle \psi_0 | \, N_{Dot} \, | \psi_0 \rangle = \mathrm{Tr} \left[\, \underline{\underline{\psi_0^\dagger}} N_{Dot} \underline{\underline{\psi_0}} \, \right], \tag{4.13}$$

where now $\underline{\underline{\psi_0}}$ is the $m \times m$ matrix given in Eq. (4.9a) and N_{Dot} is an $m \times m$ matrix. With either of these two methods we can thus calculate the occupation of the dot using DMRG for arbitrary but fixed parameter values U, V_i, and μ.

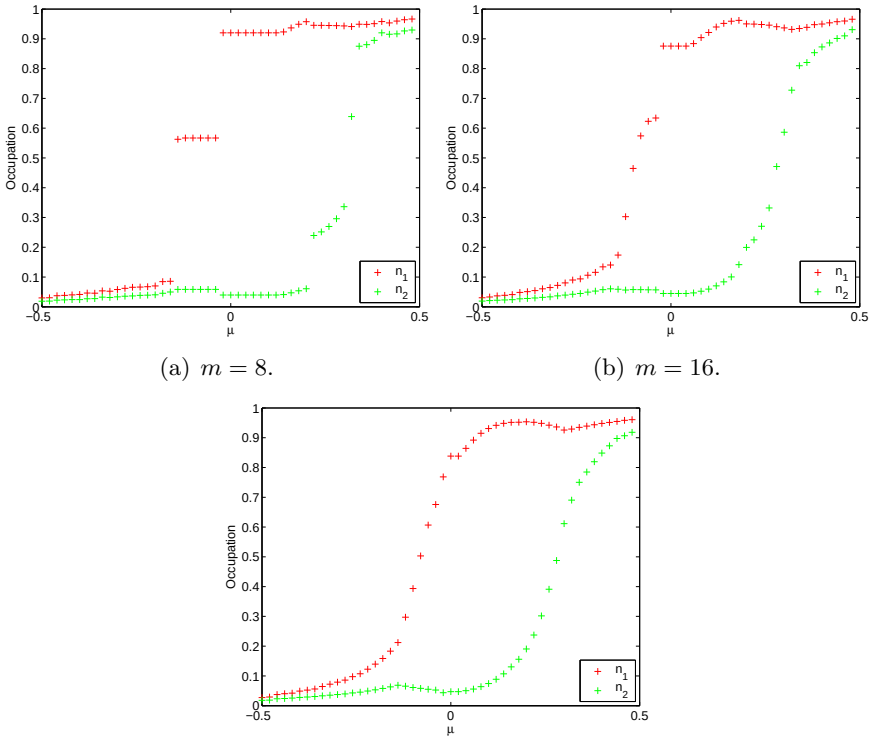

(a) $m = 8$. (b) $m = 16$.

(c) $m = 32$.

Figure 4.2: Occupations for various values of m. The occupations change qualitatively when increasing m to 32, indicating that 8 and 16 states are insufficient for this calculation. Parameter values used are $U = 0.2$ and $V_i = 0.25$. U, V_i, ϵ, and μ are given in units of t.

4.5 Results

In this section we present results obtained with our implementation of DMRG as described above. We have mainly been interested in reproducing data already presented by Berkovits. All calculations presented in this section were performed with $V_g = 0$. Initially we used $m = 8$ which quickly turned out to be insufficient to obtain accurate results. Also $m = 16$ turned out to be insufficient and after consulting with Professor Berkovits we ended up using $m = 32$. This turned out to be nearly sufficient, but also close to the capability of the available hardware. In Fig. 4.2 we show a typical improvement when increasing m, where it is clearly seen that the numerical irregularities are reduced when increasing m.

With $m = 32$ we have calculated the occupation of the levels on the dot as a function of the chemical potential. For each set of values U, V_i, and μ we have performed a full DMRG calculation of the occupation of the

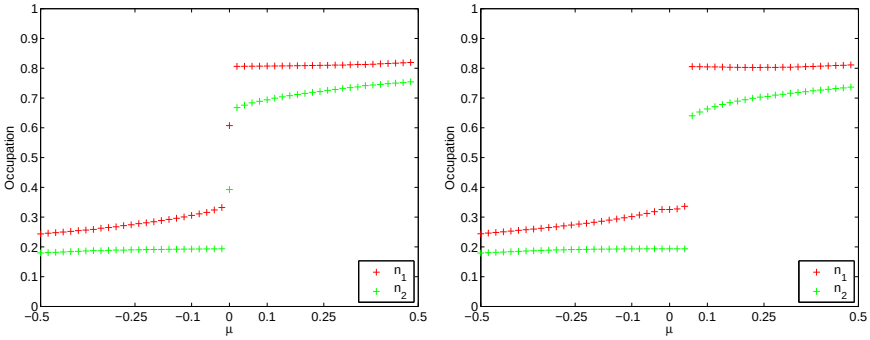

(a) $U = 0$, $V_i = 1$.

(b) $U = 0.1$, $V_i = 1$.

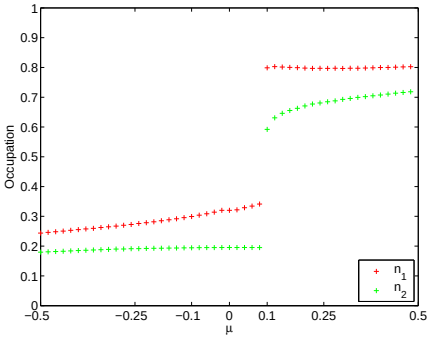

(c) $U = 0.2$, $V_i = 1$.

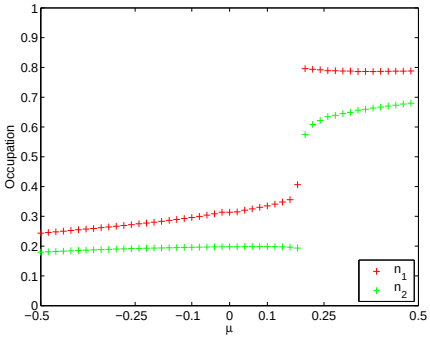

(d) $U = 0.4$, $V_i = 1$.

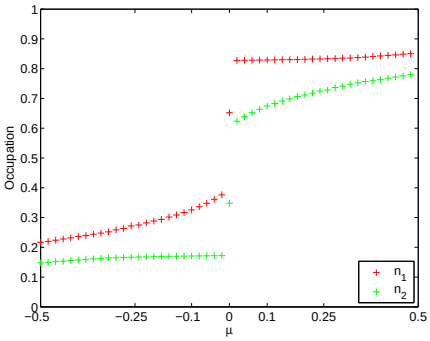

(e) $U = 0$, $V_i = 0.75$.

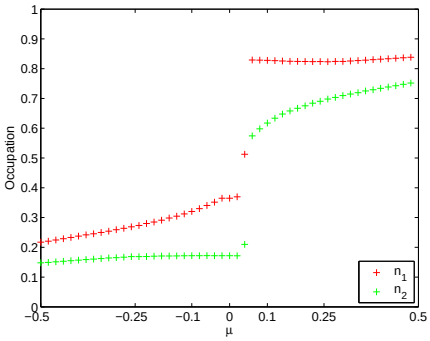

(f) $U = 0.1$, $V_i = 0.75$.

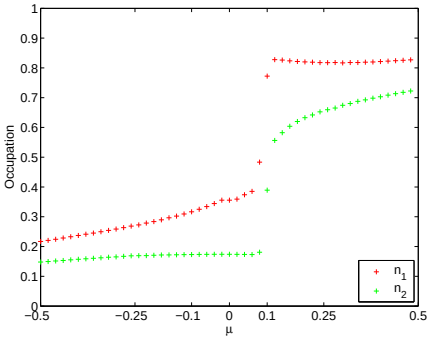

(g) $U = 0.2$, $V_i = 0.75$.

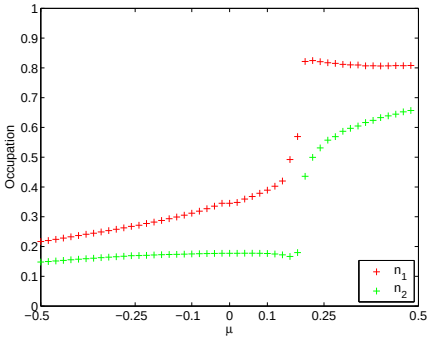

(h) $U = 0.4$, $V_i = 0.75$.

Figure 4.3: Occupations for $\epsilon = [-0.1, 0.1]$, $m = 32$ states, and 125 sites in the lead. The strong coupling V_i makes the filling of the levels occur at nearly the same energy, while the repulsion U pushes the filling of the levels upwards in energy. U, V_i, ϵ, and μ are given in units of t.

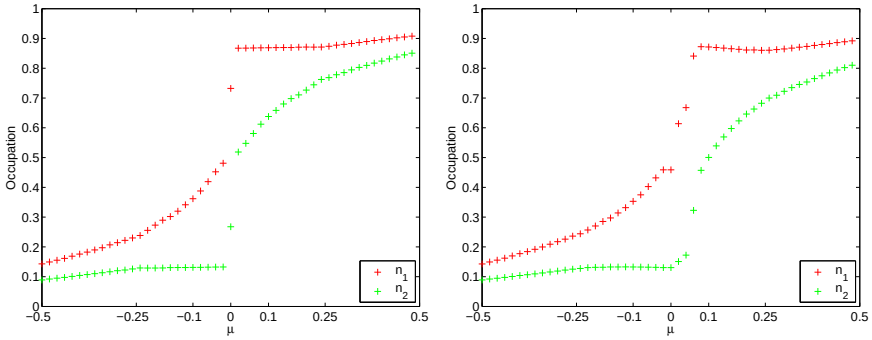

(a) $U = 0$, $V_i = 0.5$.

(b) $U = 0.1$, $V_i = 0.5$.

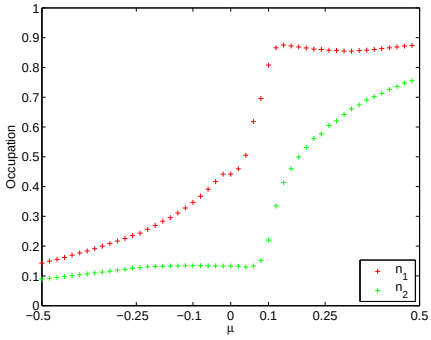

(c) $U = 0.2$, $V_i = 0.5$.

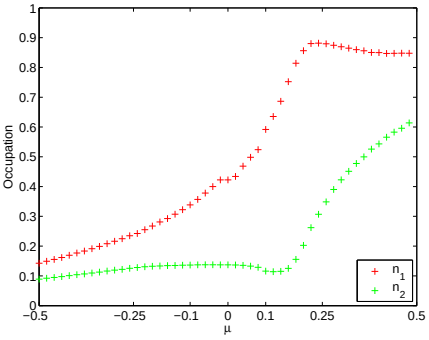

(d) $U = 0.4$, $V_i = 0.5$.

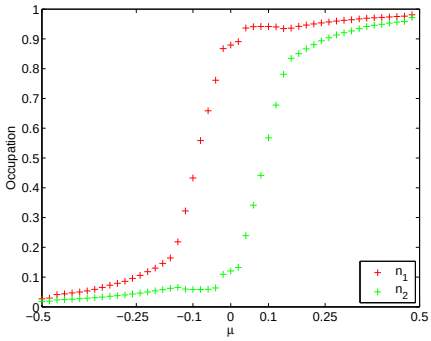

(e) $U = 0$, $V_i = 0.25$.

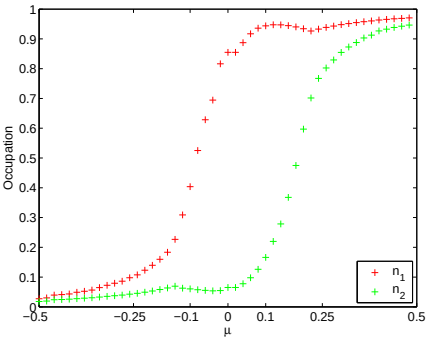

(f) $U = 0.1$, $V_i = 0.25$.

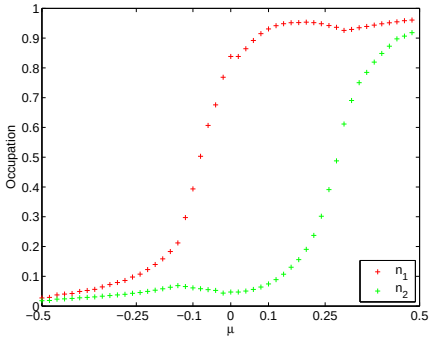

(g) $U = 0.2$, $V_i = 0.25$.

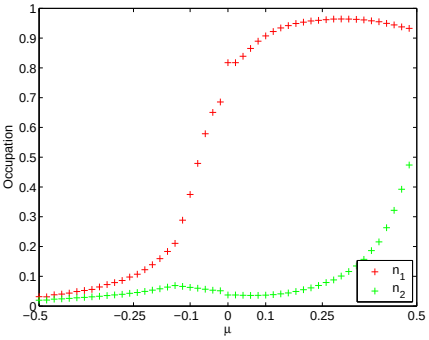

(h) $U = 0.4$, $V_i = 0.25$.

Figure 4.4: Occupations for $\epsilon = [-0.1, 0.1]$, $m = 32$ states, and 125 sites in the lead. The coupling V_i renormalizes the levels, while the repulsion U suppresses the filling of the second level. U, V_i, ϵ, and μ are given in units of t.

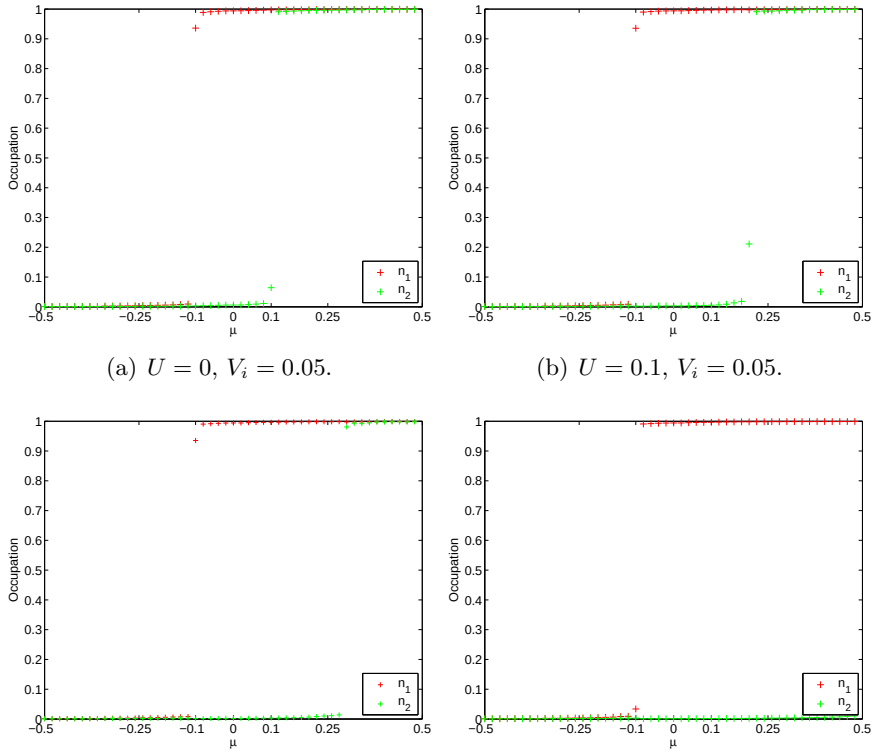

(a) $U = 0$, $V_i = 0.05$.

(b) $U = 0.1$, $V_i = 0.05$.

(c) $U = 0.2$, $V_i = 0.05$.

(d) $U = 0.4$, $V_i = 0.05$.

Figure 4.5: Occupations for $\epsilon = [-0.1, 0.1]$, $m = 32$ states, and 125 sites in the lead. The levels are essentially unchanged, but the repulsion U suppresses the filling of the second level to $\tilde{\epsilon}_2 = \epsilon_2 + U$. U, V_i, ϵ, and μ are given in units of t.

dot, obtaining occupations $n_1(\mu_i)$ and $n_2(\mu_i)$, and therefore the calculation of such graphs can be quite lengthy. Figures of the occupations of the single levels have been made for strong ($U = 0.4$), medium ($U = 0.2$), weak ($U = 0.1$), and non-interacting ($U = 0$) cases. We have collected figures with the same coupling to the leads, revealing the effect of increasing on-site interaction. The results are shown in Fig. 4.3, 4.4, and 4.5. Additionally in Fig. 4.6 we show the total occupation on the dot $n = n_1 + n_2$ for various interactions and couplings.

4.5.1 Convergence

To test the convergence of the algorithm to the infinite lead limit we have calculated occupations using lead lengths 75 and 125 for various couplings and on-site interactions, and computed the difference between these two sets

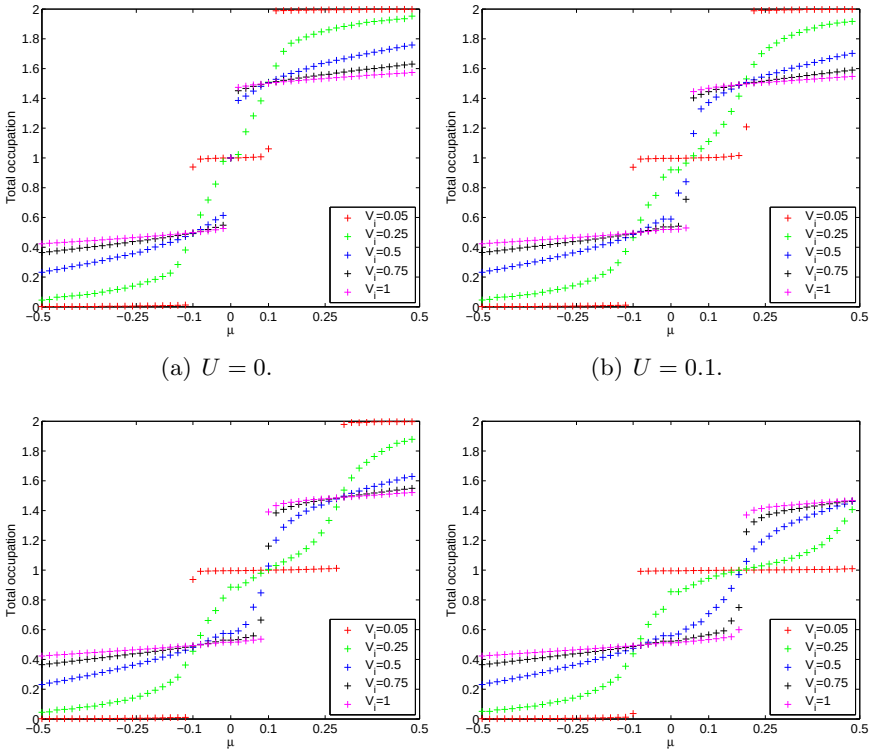

(a) $U = 0$. (b) $U = 0.1$.

(c) $U = 0.2$. (d) $U = 0.4$.

Figure 4.6: Total ocupations for $\epsilon = [-0.1, 0.1]$, $m = 32$ states, and 125 sites in the lead. For small U notice the transition from two dot levels when $V_i = 0.05$ to a single localized state when $V_i = 1$. U, V_i, ϵ, and μ are given in units of t.

of results.[1]

The majority of these results vary on the scale 10^{-3} so in these cases the algorithm has converged. There are however also cases where the scale is 10^{-2} making it more questionable if convergence really has been reached. Examining more carefully in which cases these larger deviations occur we find two cases: (i) When there are plateaus in the occupation, and (ii) when there is a μ-point *in* the step in occupation. The first case indicates that some of the numerical problems present with 75 sites in the lead are due to lacking convergence of the algorithm. The second case is quite understandable; if the position of the step in occupation moves even *slightly* when iterating further, a point located in the steep part of the step would move substantially. Either of the two however indicates lacking convergence to some degree.

[1] The length of the lead corresponds to the number of iterations in the DMRG algorithm, increasing the size of the lead in the left block by one site at each iteration.

An example is shown in Fig. 4.7 where the plateaus present with 75 sites in the lead are partly eliminated when increasing the lead length to 125 sites. Increasing the lead length to 200 sites gives practically no further improvements. In Fig. 4.7(d) we have plotted the difference in occupation for a calculation with 200 sites and a calculation with 125 sites in the lead. All differences are on the scale 10^{-3} and from this we conclude that convergence is achieved with 125 sites in the lead.

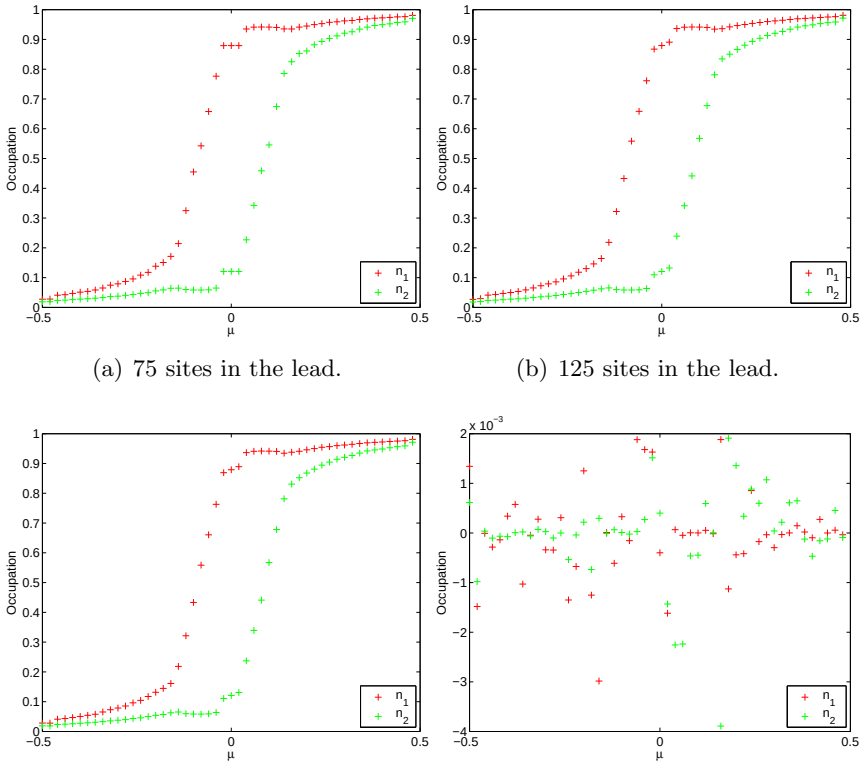

(a) 75 sites in the lead.

(b) 125 sites in the lead.

(c) 200 sites in the lead.

(d) Difference in occupations when using 200 and 125 sites in the lead.

Figure 4.7: Occupations for $\epsilon = [-0.1, 0.1]$, $V_i = 0.25$, $m = 32$ states, and 125 sites in the lead. The results are improved when using 125 rather than 75 sites in the lead. No further improvement is achieved by using 200 sites in the lead. U, V_i, ϵ, and μ are given in units of t.

4.5.2 Spectral function

To calculate the spectral function of the dot levels using DMRG methods we use the Lanczos method reviewed in Sec. 2.5.2, in particular a continued

fraction representation of the Green's functions

$$G_{a_i^\dagger a_i}(z) = \langle\psi_0|a_i^\dagger(z-H)^{-1}a_i|\psi_0\rangle, \tag{4.14a}$$

$$G_{a_i a_i^\dagger}(z) = \langle\psi_0|a_i(z+H)^{-1}a_i^\dagger|\psi_0\rangle, \tag{4.14b}$$

in a Lanczos basis where

$$G_{a_i^\dagger a_i}(z) = \cfrac{\langle\psi_0|a_i^\dagger a_i|\psi_0\rangle}{z-a_0-\cfrac{b_1^2}{z-a_1-\frac{b_2^2}{z-\cdots}}}, \tag{4.15a}$$

$$G_{a_i a_i^\dagger}(z) = \cfrac{\langle\psi_0|a_i a_i^\dagger|\psi_0\rangle}{z+a_0-\cfrac{b_1^2}{z+a_1-\frac{b_2^2}{z+\cdots}}}, \tag{4.15b}$$

We find the spectral function by

$$A(\omega) = -2\lim_{\eta\to 0^+}\mathrm{Im}\left(G_{a_i^\dagger a_i}(\omega+E_0+i\eta)+G_{a_i a_i^\dagger}(\omega-E_0+i\eta)\right). \tag{4.16}$$

In the previous calculations the DMRG basis was optimized only for the ground state of the system. To optimize the basis for properties of exited states as well we include at each step the first Lanczos vector as target state. When convergence to the infinite lead limit has been achieved we use 200 Lanczos states in the calculation of $G_{a_i^\dagger a_i}(\omega)$ and $G_{a_i a_i^\dagger}(\omega)$ in Eq. (4.15).

We have limited our calculations to $i = 1$. Note that the evaluation of $\langle\psi_0|a_1^\dagger a_1|\psi_0\rangle$ and $\langle\psi_0|a_1 a_1^\dagger|\psi_0\rangle$ requires matrix representations of the combined operators $a_1^\dagger a_1$ and $a_1 a_1^\dagger$ constructed and updated *throughout* the calculation, as explained in Sect. 2.5.1. We use different DMRG calculations to find $G_{a_1^\dagger a_1}$ and $G_{a_1 a_1^\dagger}$, since the DMRG basis has to be optimized to different additional target states in the two cases, namely the states $a_1|\psi_0\rangle$ and $a_1^\dagger|\psi_0\rangle$ respectively. In App. D we show what kind of convergence we expect based on a truncated representation of a continued fraction formally similar to the ones in Eq. (4.15). In Fig. 4.8 plots of the two terms in the spectral function are shown, $A_1 = G_{a_1^\dagger a_1} + G_{a_1 a_1^\dagger}$ for 3 values of η and $\mu = 2$. The plots are similar to the truncated continued fraction in App. D, but the known structure of the spectral function is not reproduced.

Based on work reported in the literature we expect that keeping more states would improve these calculations. We have not been able to target additional Lanczos states and maintain precision, which we expect is the major reason for the failure of these calculations. Wang *et al.* [2] use m from 100 and upwards, whereas we use $m \leq 32$. They consider a different model but we still expect the small m to be the major difficulty in these calculations.

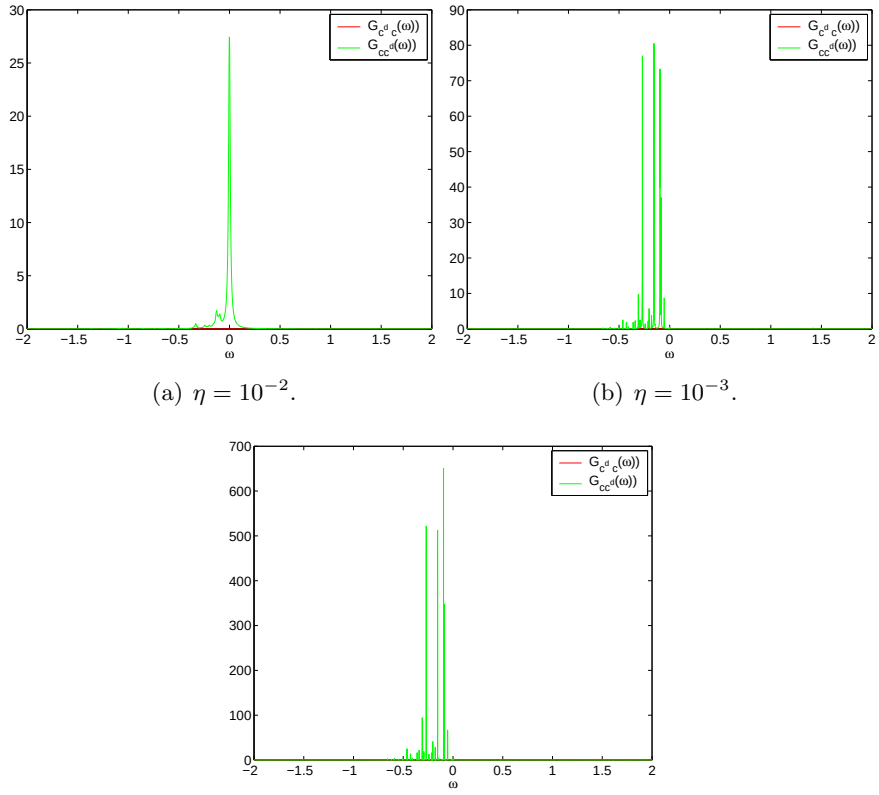

(a) $\eta = 10^{-2}$.

(b) $\eta = 10^{-3}$.

(c) $\eta = 10^{-4}$.

Figure 4.8: DMRG calculation of the spectral function, $A_1 = G_{a_1^\dagger a_1} + G_{a_1 a_1^\dagger}$, using $m = 32$ and 125 sites in the leads, $U = 0$, $\mu = 2$, and $V_i = 1$. The analytically known structure of $A_1(\omega)$ is not reproduced. U, V_i, ϵ, μ, and ω are given in units of t.

4.6 Interpretation

In this section we briefly comment on the results found using our DMRG implementation. We distinguish two different parameters, the coupling to the leads V_i and the on-site repulsion U.

For very weak coupling to the leads the levels of the dot are essentially unchanged, only the second level is renormalized. The filling of the first level occurs when the chemical potential crosses the energy of the level, and the filling of the second level occurs when the chemical potential reaches the renormalized energy $\tilde{\epsilon}_2 = \epsilon_2 + U$, as seen in Fig. 4.6. When the coupling is turned up there is a crossover to a single localized state on the dot, revealed by a sharp jump of unit magnitude in the total occupation, located between ϵ_1 and ϵ_2, as seen in Fig. 4.6(a).

When interactions and couplings both are turned up some features of

the non-interacting limit persist but due to the interactions the position of the jump in occupation of the second level and the localized state is shifted, as seen in Fig. 4.6(b)-4.6(d). All jumps are smeared by the interactions and for stronger interactions simple arguments are insufficient.

4.7 Analytic result

In the non-interacting limit it is possible to find analytic results for the occupation using Green's functions theory, [17, 18]. In this limit the Hamiltonian is

$$H = H_D + H_L + H_{DL}, \tag{4.17a}$$

$$H_D = \sum_{i=a}^{b} (\epsilon_i - V_g)\, a_i^\dagger a_i \equiv \sum_{i=a}^{b} \varepsilon_i a_i^\dagger a_i, \tag{4.17b}$$

$$H_L = -t \sum_{j=1}^{\infty} \left(c_j^\dagger c_{j+1} + c_{j+1}^\dagger c_j \right) + \varepsilon \sum_{j=1}^{\infty} c_j^\dagger c_j, \tag{4.17c}$$

$$H_{DL} = \sum_{i=a}^{b} V_i \left(a_i^\dagger c_1 + c_1^\dagger a_i \right). \tag{4.17d}$$

In order not to clutter up the notation we use indices a and b to denote the dot levels and $1, 2, \cdots$ to denote lead sites. Also in retarded Green's functions it is understood that a convergence should be included $\omega \to \omega + i\eta$.

We consider the full Green's functions on the dot generally defines as

$$G_{ij}^R(t-t') = -i\theta(t-t') \left\langle \left\{ a_i(t), a_j^\dagger(t') \right\} \right\rangle. \tag{4.18}$$

In App. E we show how the equations of motion (EOMs) for the relevant Green's functions are computed. In particular for G_{aa}^R we find the series of EOMs

$$(i\partial_t - \varepsilon_a) G_{aa}^R(t-t') = \delta(t-t') + V_a G_{1a}^R(t-t'), \tag{4.19a}$$

$$(i\partial_t - \varepsilon) G_{1a}^R(t-t') = V_a G_{aa}^R(t-t') + V_b G_{ba}^R(t-t') - tG_{2a}^R(t-t'), \tag{4.19b}$$

$$(i\partial_t - \varepsilon) G_{2a}^R(t-t') = -tG_{1a}^R(t-t') - tG_{3a}^R(t-t'), \tag{4.19c}$$

$$\vdots$$

$$(i\partial_t - \varepsilon) G_{ja}^R(t-t') = -tG_{j-1a}^R(t-t') - tG_{j+1a}^R(t-t'), \quad j \geq 2, \tag{4.19d}$$

where the hybrid Green's function is

$$G_{ja}^R(t-t') = -i\theta(t-t') \left\langle \left\{ c_j(t), a_a^\dagger(t') \right\} \right\rangle, \quad j \geq 2. \tag{4.20}$$

These EOMs can be understood by a relatively simple argument, taking G^R_{1a} as an example: From the first site in the lead there are three possible hoppings, to site a on the dot via hopping element V_a, to site b on the dot via hopping element V_b, and finally to site 2 in the lead via hopping element $-t$, and of course it is possible to stay on site 1, with energy ε.

Fourier transforming we thus find the EOMs

$$\begin{aligned}
(\omega-\varepsilon_a)G^R_{aa}(\omega) &= 1+V_aG^R_{1a}(\omega). && \text{(4.21a)}\\
(\omega-\varepsilon)G^R_{1a}(\omega) &= V_aG^R_{aa}(\omega)+V_bG^R_{ba}(\omega)-tG^R_{2a}(\omega). && \text{(4.21b)}\\
&\vdots\\
(\omega-\varepsilon)G^R_{ja}(\omega) &= -tG^R_{j-1a}(\omega)-tG^R_{j+1a}(\omega), \quad j\geq 2. && \text{(4.21c)}
\end{aligned}$$

Eq. (4.21a)-(4.21c) form a semi-infinite set of equations. In App. E we show that the final solutions for $G^R_{aa}(\omega)$ and $G^R_{bb}(\omega)$ are

$$\begin{aligned}
G^R_{aa}(\omega) &= \frac{1}{\omega-\varepsilon_a-\Sigma^R_{aa}(\omega)-\frac{\Sigma^R_{ab}(\omega)\Sigma^R_{ba}(\omega)}{\omega-\varepsilon_b-\Sigma^R_{bb}(\omega)}}, && \text{(4.22a)}\\
G^R_{bb}(\omega) &= \frac{1}{\omega-\varepsilon_b-\Sigma^R_{bb}(\omega)-\frac{\Sigma^R_{ba}(\omega)\Sigma^R_{ab}(\omega)}{\omega-\varepsilon_a-\Sigma^R_{aa}(\omega)}}. && \text{(4.22b)}
\end{aligned}$$

4.7.1 Occupation

Having found $G^R_{aa}(\omega)$ and $G^R_{bb}(\omega)$ it is possible to find the spectral function and hence the occupations of the levels. The relevant selfenergies are

$$\begin{aligned}
\Sigma^R_{aa}(\omega) &= V_a^2\tilde{G}^R_{11}(\omega), && \text{(4.23a)}\\
\Sigma^R_{bb}(\omega) &= V_b^2\tilde{G}^R_{11}(\omega), && \text{(4.23b)}\\
\Sigma^R_{ab}(\omega) &= V_aV_b\tilde{G}^R_{11}(\omega), && \text{(4.23c)}\\
\Sigma^R_{ba}(\omega) &= V_bV_a\tilde{G}^R_{11}(\omega), && \text{(4.23d)}
\end{aligned}$$

so that $\tilde{G}^R_{11}(\omega)$ essentially determines the complex structure of the self-energies. In App. E we show that $\tilde{G}^R_{11}$ can be expressed as

$$\tilde{G}^R_{11}(\omega) = \begin{cases} \frac{\omega/2t}{t}-i\frac{\sqrt{1-(\omega/2t)^2}}{t}, & |\omega|<2t,\\ \frac{\omega/2t-\mathrm{sign}(\omega)\sqrt{(\omega/2t)^2-1}}{t}, & |\omega|\geq 2t, \end{cases} \qquad (4.24)$$

and in Fig. 4.9(d) the real and imaginary part of $\tilde{G}^R_{11}$ are plotted.

In equilibrium the lesser Green's function generally defined as

$$G^<_{ij}(t) \equiv i\langle a_j^\dagger a_i(t)\rangle, \qquad (4.25)$$

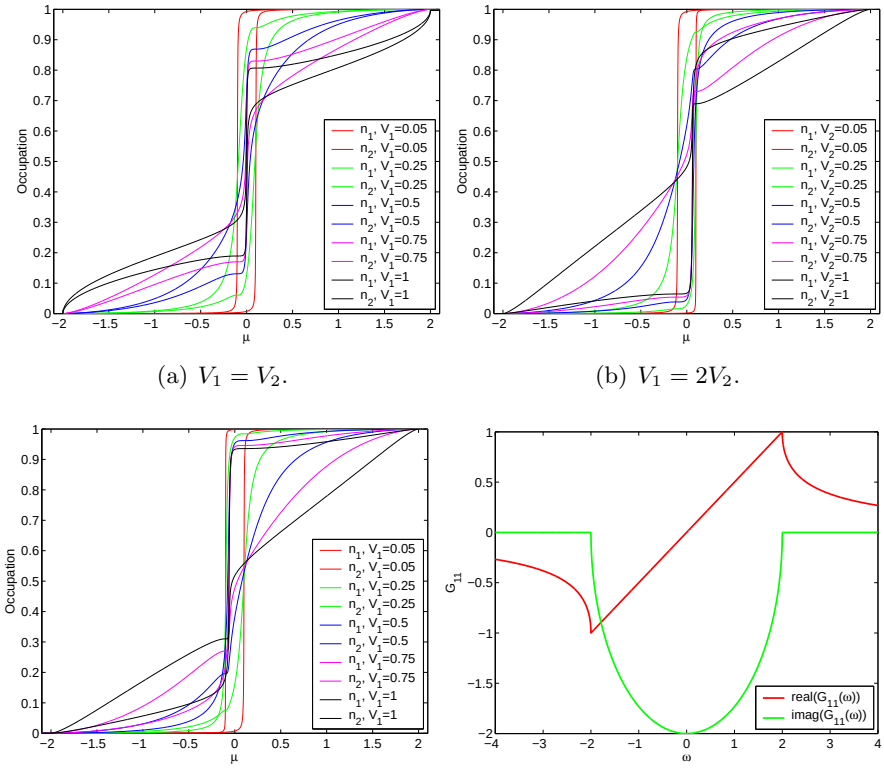

(a) $V_1 = V_2$. (b) $V_1 = 2V_2$.

(c) $V_2 = 2V_1$. (d) Real and imaginary part of $\tilde{G}_{11}$.

Figure 4.9: Occupations in the non-interacting case for $\epsilon = [-0.1, 0.1]$, computed using Green's function theory. U, V_i, ϵ, μ, and ω are given in units of t.

may be reexpressed using the Fluctuation Dissipation Theorem [18], p. 171. Particularly we find

$$G_{ii}^{<}(\omega) \;=\; in_F(\omega)A_{ii}(\omega), \tag{4.26}$$

where $n_F = (e^{-\beta(\mu-\omega)}+1)^{-1}$ is the Fermi distribution and A_{ii} is the spectral function for level i. Hence we can express the occupation of the dot level i by,

$$\begin{aligned} n_i \;&\equiv\; \left\langle a_i^\dagger a_i \right\rangle \\ &=\; -iG_{ii}^{<}(t=0) \\ &=\; -i\int_{-\infty}^{\infty}\frac{d\omega}{2\pi}G_{ii}^{<}(\omega) \\ &=\; \int_{-\infty}^{\infty}\frac{d\omega}{2\pi}n_F(\omega)A_{ii}(\omega). \end{aligned} \tag{4.27}$$

Using also the definition of the spectral function, $A_{ii}(\omega) = -2\mathrm{Im}G_{ii}^{R}(\omega)$, and the fact that in the zero temperature limit n_F is a step function at the

chemical potential, we find the final solution for the occupation,

$$n_i(\mu) \;=\; -\int_{-\infty}^{\mu} \frac{d\omega}{\pi} \mathrm{Im} G^R_{ii}(\omega), \quad \mu \leq 2t. \tag{4.28}$$

Note that with the parameter values we use, the renormalized levels remain within the band, but for generic parameter values this is not necessarily the case.

Expressing the occupations analytically involves finding the imaginary part of the Green's function, which yields very large expressions that do not simplify. Therefore we have performed these calculations numerically. Some results obtained are shown in Fig. 4.9 for various couplings to the lead.

4.7.2 Comparison

Having performed both analytic and DMRG calculations of the occupation of the dot as a function of chemical potential in the non-interacting limit we are able to benchmark DMRG. In Fig. 4.10 and 4.11 both DMRG and analytic results are plotted simultaneously, in rather consistency.

Calculations have been performed for $m = 8$, $m = 16$, and $m = 32$, which enables us to check if the deviations of the DMRG from the analytic result is caused by a too large truncation, or wether other problems are significant as well. The calculation with $m = 32$ still shows irregularities for certain values of μ, but the curves are generally very much better. The numerical problems were not completely solved by increasing the number of states kept to $m = 32$ but we expect that increasing m even further would solve the remaining.

However, based on the data presented here we conclude that indeed DMRG reproduces the analytic data quite well, with the largest deviations in the vicinity of the step in occupation. Even with $m = 8$ the resemblance of DMRG and analytic data is very clear, although also unphysical features caused by numerical problems are present. Considering that in this case the dot and (in principle) infinite lead is described using a total of 8 states the performance of DMRG is quite impressing.

4.8 Conclusions

We successfully implemented DMRG on a quantum dot coupled to a single lead in the semi-infinite lead limit. Using a setup identical to Berkovits's we performed DMRG calculations of the occupation of the dot for various couplings to the leads, both with and without on-site interaction.

Calculations similar to Berkovits's were performed using our implementation of DMRG. We explored the precision of DMRG versus the number of states kept and found that the precision of calculations depends heavily

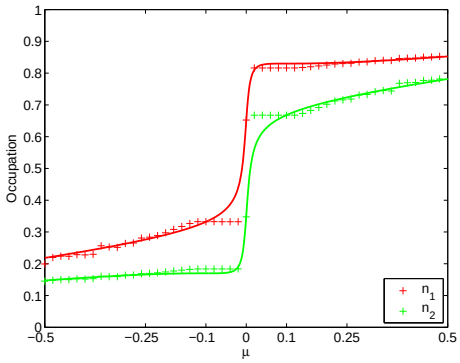

(a) $m = 8$, $V_i = 0.75$.

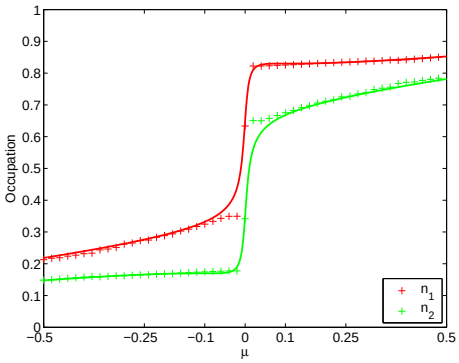

(b) $m = 16$, $V_i = 0.75$.

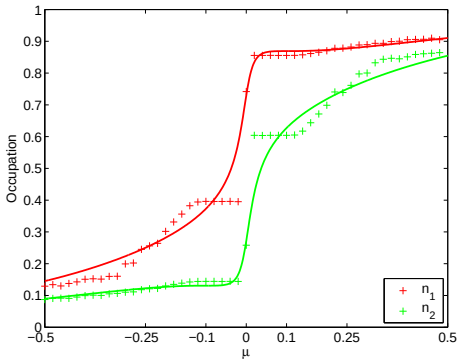

(c) $m = 8$, $V_i = 0.5$.

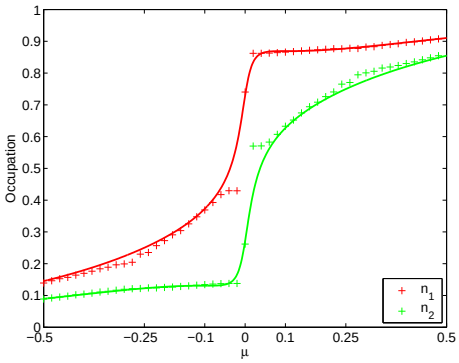

(d) $m = 16$, $V_i = 0.5$.

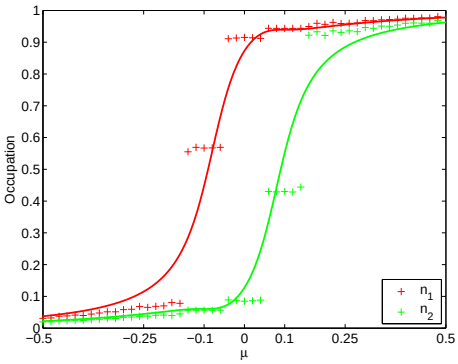

(e) $m = 8$, $V_i = 0.25$.

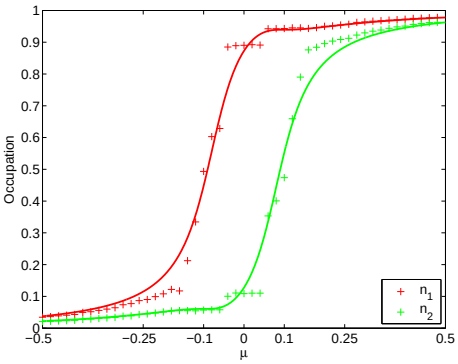

(f) $m = 16$, $V_i = 0.25$.

Figure 4.10: Comparison between analytic and DMRG results for $\epsilon = [-0.1, 0.1]$ and $U = 0$. Calculated with $m = 8$ and $m = 16$ states, and 250 and 175 sites in the lead respectively. Notice the improvement in the DMRG results when using $m = 16$ rather than $m = 8$. U, V_i, ϵ, and μ are given in units of t.

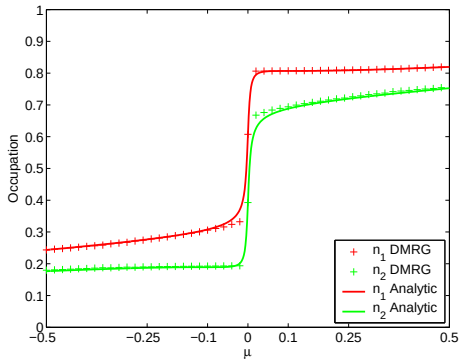

(a) $V_i = 1$.

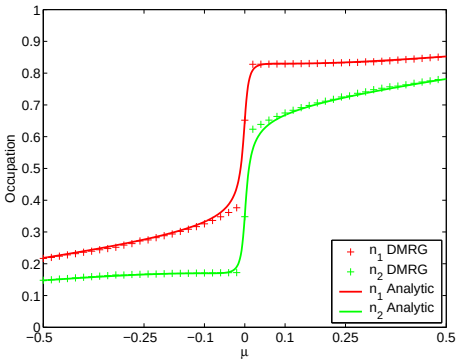

(b) $V_i = 0.75$.

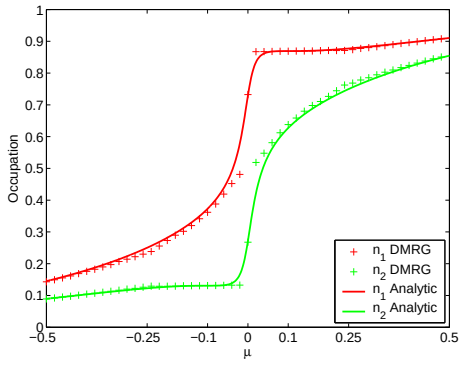

(c) $V_i = 0.5$.

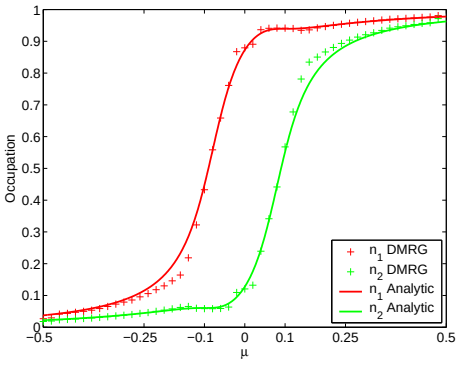

(d) $V_i = 0.25$.

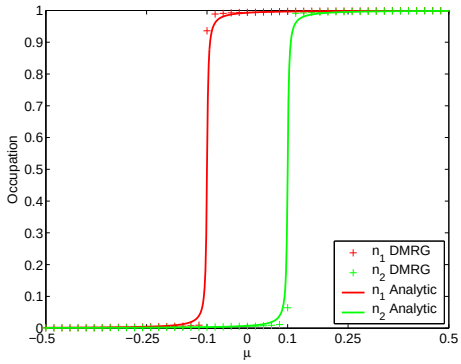

(e) $V_i = 0.05$.

Figure 4.11: Comparison between analytic and DMRG results for $\epsilon = [-0.1, 0.1]$ and $U = 0$. Calculated with $m = 32$ states, and 125 sites in the lead. The DMRG and analytic results agree very well with the largest deviations in the vicinity of the step. U, V_i, ϵ, and μ are given in units of t.

on m. In order to produce quality data we needed to use $m = 32$, which eliminated the majority of numerical problems. In the non-interacting limit we compared DMRG and analytic calculations and found the DMRG results quite accurate. This comparison was made for various couplings to the lead. Using even a very limited number of states the resemblance between DMRG and analytic results is very clear. Calculations for finite on-site repulsion were made for various couplings to the lead and we briefly commented on these results. We attempted a combined Lanczos and DMRG calculation of the spectral function of the dot, but were not successful, and discussed probable explanations for this.

Chapter 5

Quantum dot with two infinite leads

The natural setup when considering transport is a system connected to two leads. One such system studied by many people is a quantum dot coupled to one-dimensional leads in various configurations and for various parameters. Berkovits *et al.* have performed DMRG calculations on a setup in which a quantum dot is coupled to multiple leads calculating the charging for varying number of open channels [19].

In this section we use a simpler setup, performing DMRG calculations on a quantum dot coupled to two one-dimensional semi-infinite leads. Using as starting point the existing code for a quantum dot with a single lead, we have performed the most straightforward generalization to two leads. Using this we calculate the occupation of the dot versus chemical potential in the system. To approach transport we calculate the occupation of the biased dot varying the gate voltage. We use different chemical potentials for the two leads to simulate finite bias. In the non-interacting limit we calculate analytic Green's functions results to benchmark both sets of DMRG calculations. Finally we comment on the results calculated using our DMRG implementation.

5.1 Hamiltonian

Considering a quantum dot with N_{Dot} levels and treating the electrons as spinles the Hamiltonians are essentially the same as for the single lead case, only here there is an additional lead and couplings of this lead to the quantum dot

$$H_{Dot} = \sum_{i=1}^{N_{Dot}} (\epsilon_i - V_g) a_i^\dagger a_i + U \sum_{i>j}^{N_{Dot}} a_i^\dagger a_i a_j^\dagger a_j, \tag{5.1}$$

$$H_{Right\ Lead} = -t\sum_{j=1}^{\infty}(c_j^\dagger c_{j+1} + c_{j+1}^\dagger c_j), \tag{5.2a}$$

$$H_{Left\ Lead} = -t\sum_{j=-1}^{-\infty}(c_j^\dagger c_{j-1} + c_{j-1}^\dagger c_j), \tag{5.2b}$$

$$H_{DL} = \sum_{i=1}^{N_{Dot}}\Big(V_i^R(a_i^\dagger c_1 + c_1^\dagger a_i) + V_i^L(a_i^\dagger c_{-1} + c_{-1}^\dagger a_i)\Big), \tag{5.2c}$$

and including a chemical potential μ, the complete Hamiltonian is

$$H = H_{Dot} + H_{Lead} + H_{DL} - \mu\Big(\sum_{i=1}^{N_{Dot}} a_i^\dagger a_i + \sum_{j=1}^{\infty}\big(c_j^\dagger c_j + c_{-j}^\dagger c_{-j}\big)\Big). \tag{5.3}$$

All site matrices are identical to the single lead case, and we refer to Sect. 4.1 for details. Again we specialize to two dot levels, i.e. $N_{Dot} = 2$.

Hermiticity of H

Also here we find numerical imprecisions preventing the Hamiltonian from being completely hermitian. We eliminate these by replacing

$$\frac{H + H^\dagger}{2} \rightarrow H, \tag{5.4}$$

which enforces hermiticity on any matrix and hence should be used with caution, as explained in Sect. 3.1.

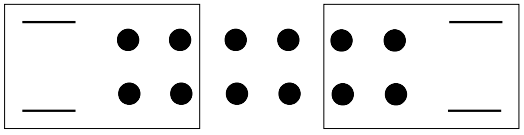

(a) Superblock setup for the quantum dot with 2 leads.

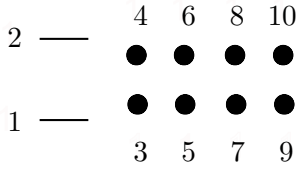

(b) Numbering of the left block basis states.

Figure 5.1: Superblock configuration and numbering of the basis states for the left block.

5.2 Superblock setup

We use a superblock setup, in which two leads connect two quantum dots as seen in Fig. 5.1(a). Note that this is not a real space picture but a convenient way to picturize the superblock setup. The numbering of the states we use,

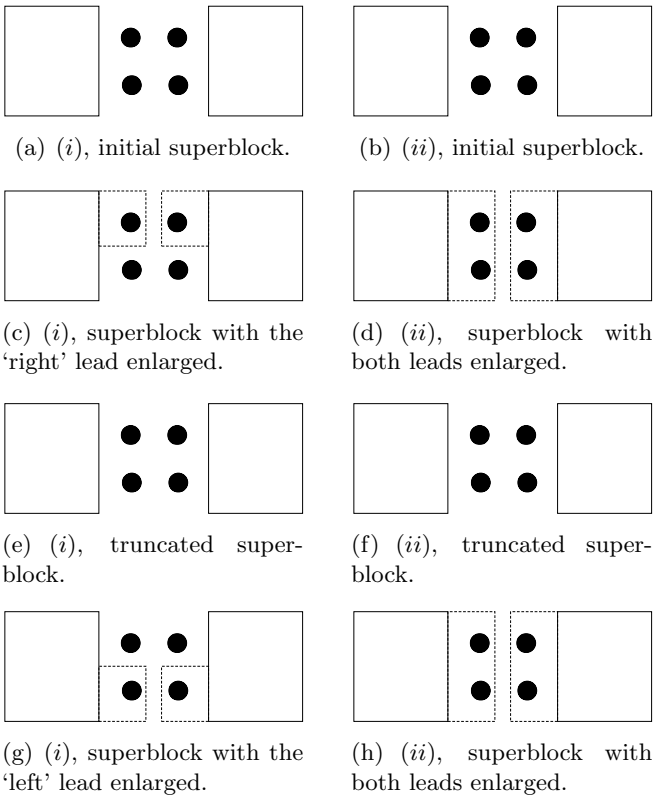

(a) (*i*), initial superblock.

(b) (*ii*), initial superblock.

(c) (*i*), superblock with the 'right' lead enlarged.

(d) (*ii*), superblock with both leads enlarged.

(e) (*i*), truncated superblock.

(f) (*ii*), truncated superblock.

(g) (*i*), superblock with the 'left' lead enlarged.

(h) (*ii*), superblock with both leads enlarged.

Figure 5.2: Two different methods of enlarging the leads.

illustrated in Fig. 5.1(b), is chosen in order to have an environment block that resembles the system block itself. The dot level i couples to the left and right leads via couplings V_i^L and V_i^R respectively, so there are a total of four different coupling parameters.

5.3 Infinite system sweep

The basic infinite system step is similar to the single lead setup. The difference is that here we have two leads and both should be enlarged. This can be done in several different ways, and we have considered two: (*i*) Including a site in *one* of the leads at each step and then alternate the lead that is enlarged, and (*ii*) including a site in *both* the leads at each step. The two methods are illustrated in Fig. 5.2.

Enlarging only one lead in the generic DMRG step the ground state of the superblock has to be computed twice as many times when building up a given lead length. A number of matrices are updated at each step, making the total computational time for diagonalization and updating matrices roughly

twice as long for a given lead length, when only enlarging one lead. Enlarging both leads at each step turned out to be approximately four times faster. Therefore we chose to use method (*ii*) and enlarge *both leads* at each DMRG step. The drawback of this choice is that the truncation performed at each step is larger, possibly reducing the overall precision. Unfortunately we did not have the time to test this. A careful comparison of the two possibilities should be performed before conclusions regarding the relative precision can be made.

5.4 Results

In this setup as in the previous two expectation values of operators can be obtained in two apparently different ways, as explained in Sect. 2.5 and 4.4.

We have performed calculations for various on-site interactions U and coupling to the leads $V_i^{L/R}$ with zero gate voltage $V_g = 0$. In this setup the superblock size – for fixed left and right block size m – is four times bigger than in the single lead case due to the two extra central sites in the superblock setup. Using the databars at DTU and equipped with generous amounts of patience we managed to use $m = 32$ in these calculations as well.[1] The occupations calculated are shown in Fig. 5.3 and 5.4. To expose the effect of on-site interaction we have collected figures with fixed coupling to the leads and varying U. Additionally in Fig. 5.6 we have plotted the total occupation of the dot $n(\mu) = n_1(\mu) + n_2(\mu)$.

5.4.1 Convergence

In order to test the convergence of the algorithm we have calculated the occupation of the dot using 125 and 200 sites in each lead. All these results differ on the scale of 10^{-3}, as seen in the example in Fig. 5.5, and hence convergence *is* reached using 125 sites in each lead.

5.5 Interpretation

In this section we briefly comment on the results presented in the previous section. We distinguish two different sets of parameters, the coupling to the leads $V_i^{L,R}$ and the on-site repulsion U. Generally we use weaker couplings to the leads in these calculations than in the single lead setup to keep the renormalized levels inside the band.

For very weak coupling to the leads the levels on the dot are essentially unchanged, only the second level is renormalized. The filling of the first level occurs when the chemical potential crosses the energy of the level, and

[1] Approximately 800 MB of memory is needed for these calculations. The total number of superblock states is $2^4 \times m^2 = 16384$.

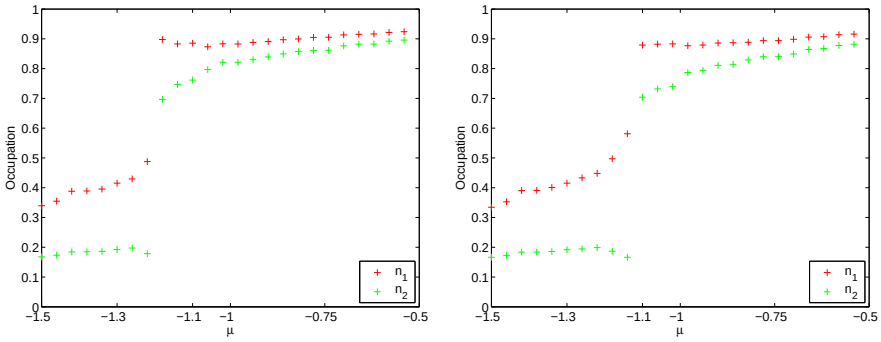

(a) $U = 0$, $V_i^{L/R} = 0.4$.

(b) $U = 0.1$, $V_i^{L/R} = 0.4$.

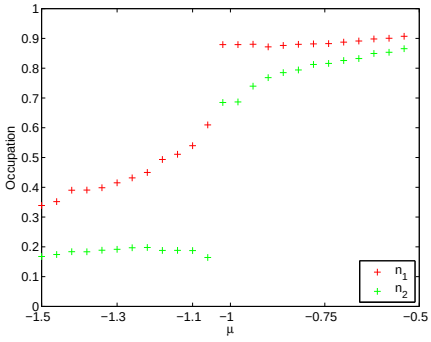

(c) $U = 0.2$, $V_i^{L/R} = 0.4$.

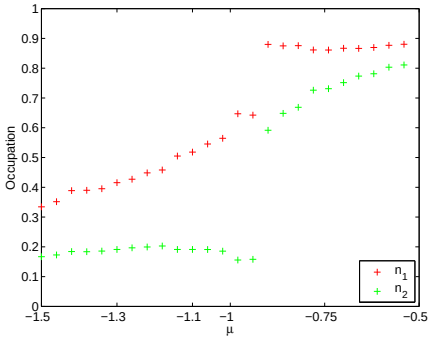

(d) $U = 0.4$, $V_i^{L/R} = 0.4$.

Figure 5.3: Occupations for $\epsilon = [-1.3, -1.1]$, $m = 32$ states, and 125 sites in the lead. The strong coupling $V_i^{L/R}$ makes the filling of the levels occur at nearly the same energy, while the repulsion U pushes the filling of the levels upwards in energy. U, $V_i^{L/R}$, ϵ, and μ are given in units of t.

the filling of the second level occurs when the chemical potential reaches the renormalized energy $\tilde{\epsilon}_2 = \epsilon_2 + U$, as seen in Fig. 5.4. When the coupling is turned up there is a crossover to a single localized state on the dot, revealed by a sharp jump of unit magnitude in the total occupation, located between ϵ_1 and ϵ_2, as seen in Fig. 5.6(a).

When interactions and couplings both are turned up some features of the non-interacting limit persist, as seen in Fig. 5.6(b)-5.6(d), but due to the interactions the position of the jump in occupation of the second level and the localized state is shifted. All jumps are smeared by the interactions and for stronger interactions simple arguments are insufficient.

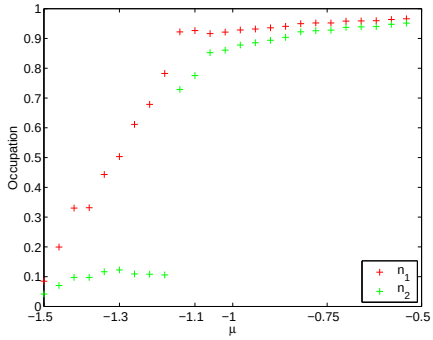

(a) $U = 0$, $V_i^{L/R} = 0.25$.

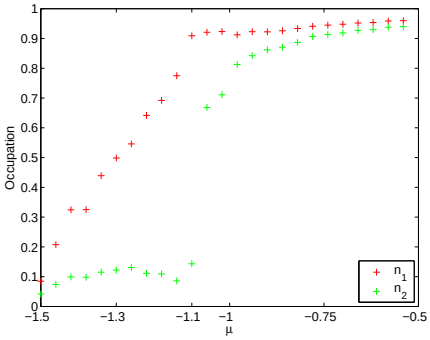

(b) $U = 0.1$, $V_i^{L/R} = 0.25$.

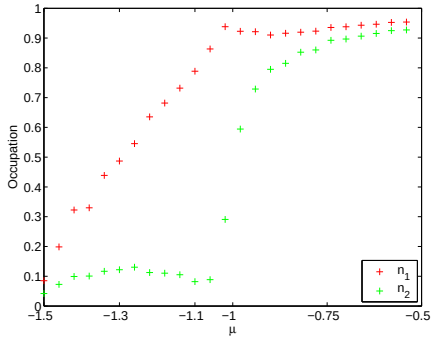

(c) $U = 0.2$, $V_i^{L/R} = 0.25$.

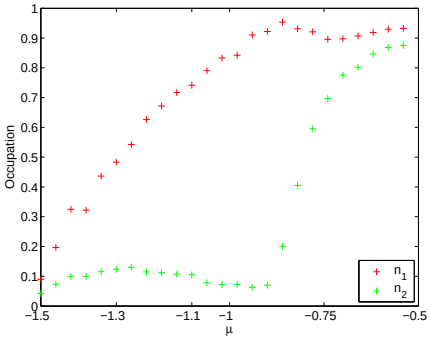

(d) $U = 0.4$, $V_i^{L/R} = 0.25$.

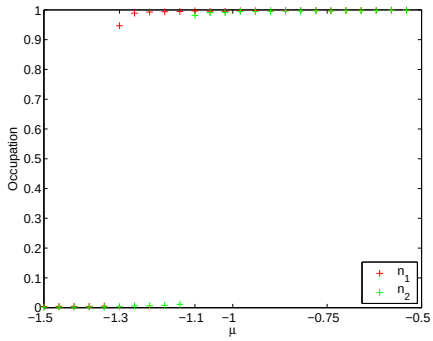

(e) $U = 0$, $V_i^{L/R} = 0.05$.

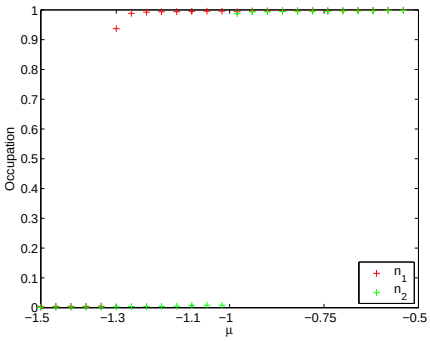

(f) $U = 0.1$, $V_i^{L/R} = 0.05$.

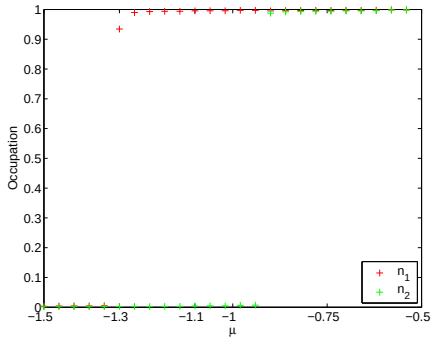

(g) $U = 0.2$, $V_i^{L/R} = 0.05$.

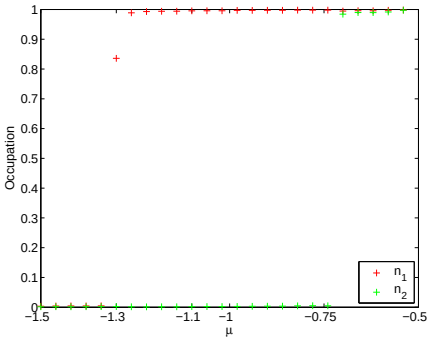

(h) $U = 0.4$, $V_i^{L/R} = 0.05$.

Figure 5.4: Occupations for $\epsilon = [-1.3, -1.1]$, $m = 32$ states, and 125 sites in the lead. The repulsion U suppresses the filling of the second level. U, $V_i^{L/R}$, ϵ, and μ are given in units of t.

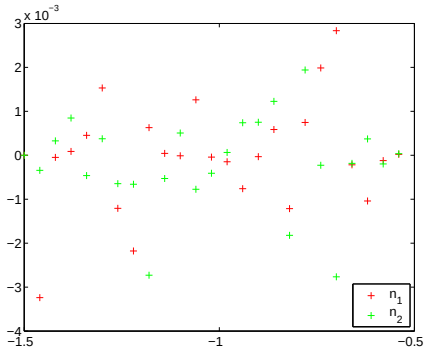

Figure 5.5: Difference in occupations for $\epsilon = [-1.3, -1.1]$, $V_i^{L/R} = 0.25$, $m = 32$ states, and 125 and 200 sites in each lead respectively. Notice the scale on which the two sets of occupations differ from each other.

5.6 Analytic result

In the non-interacting limit it is possible to calculate the occupations of the dot levels analytically using Green's functions theory [17, 18]. The Hamiltonian is

$$H = H_{Dot} + H_{Right\ Lead} + H_{Left\ Lead} + H_{DL,}, \tag{5.5a}$$

$$H_{Dot} = \sum_{i=a}^{b} (\epsilon_i - V_g) a_i^\dagger a_i \equiv \sum_i \varepsilon_a a_i^\dagger a_i, \tag{5.5b}$$

$$H_{Right\ Lead} = -t \sum_{j=1}^{\infty} (c_j^\dagger c_{j+1} + c_{j+1}^\dagger c_j) + \varepsilon \sum_{j=1}^{\infty} c_j^\dagger c_j, \tag{5.5c}$$

$$H_{Left\ Lead} = -t \sum_{j=-1}^{-\infty} (c_j^\dagger c_{j-1} + c_{j-1}^\dagger c_j) + \varepsilon \sum_{j=-1}^{-\infty} c_j^\dagger c_j, \tag{5.5d}$$

$$H_{DL} = \sum_{i=a}^{b} \left(V_i^R (a_i^\dagger c_1 + c_1^\dagger a_i) + V_i^L (a_i^\dagger c_{-1} + c_{-1}^\dagger a_i) \right). \tag{5.5e}$$

In order not to clutter up the notation we denote by a and b the dot levels and by $1, 2, \cdots$ the lead sites, and in retarded Green's functions the convergence factor $\omega \to \omega + i\eta$ is not written explicitly.

We seek the full Green's function for the dot levels generally defined as

$$G_{ij}^R(t - t') = -i\theta(t - t') \langle \{a_i(t), a_j^\dagger(t')\} \rangle. \tag{5.6}$$

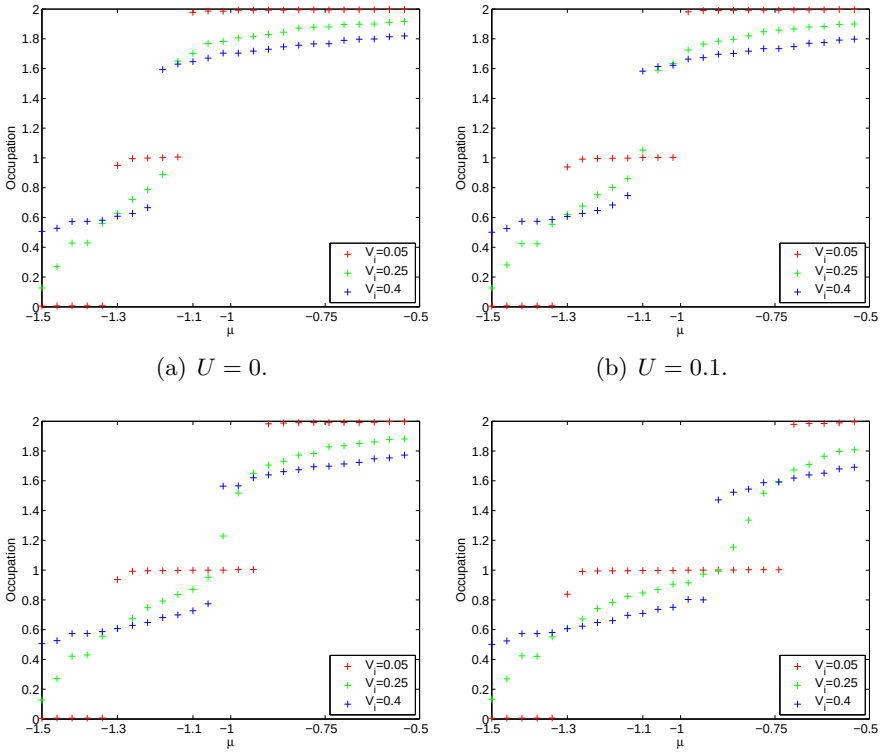

(a) $U = 0$. (b) $U = 0.1$.

(c) $U = 0.2$. (d) $U = 0.4$.

Figure 5.6: Total occupations for $\epsilon = [-1.3, -1.1]$, $m = 32$ states, and 125 sites in the lead. Notice the crossover to a single localized state when the coupling $V_i^{L/R}$ increases. U, $V_i^{L/R}$, ϵ, and μ are given in units of t.

In App. E we show how the EOM for G^R_{aa} are obtained,

$$
\begin{aligned}
(\omega - \varepsilon_a)G^R_{aa}(\omega) &= 1 + V^R_a G^R_{1a}(\omega) + V^L_a G^R_{-1a}(\omega), && \text{(5.7a)}\\
(\omega - \varepsilon)G^R_{1a}(\omega) &= V^R_a G^R_{aa}(\omega) + V^R_b G^R_{ba}(\omega) - tG^R_{2a}(\omega), && \text{(5.7b)}\\
(\omega - \varepsilon)G^R_{-1a}(\omega) &= V^L_a G^R_{aa}(\omega) + V^L_b G^R_{ba}(\omega) - tG^R_{-2a}(\omega), && \text{(5.7c)}\\
(\omega - \varepsilon)G^R_{2a}(\omega) &= -tG^R_{1a}(\omega) - tG^R_{3a}(\omega), && \text{(5.7d)}\\
(\omega - \varepsilon)G^R_{-2a}(\omega) &= -tG^R_{-1a}(\omega) - tG^R_{-3a}(\omega), && \text{(5.7e)}\\
&\vdots\\
(\omega - \varepsilon)G^R_{ja}(\omega) &= -tG^R_{j-1a}(\omega) - tG^R_{j+1a}(\omega), && \text{(5.7f)}\\
(\omega - \varepsilon)G^R_{-ja}(\omega) &= -tG^R_{-j+1a}(\omega) - tG^R_{-j-1a}(\omega), && \text{(5.7g)}
\end{aligned}
$$

and dropping the arguments the solution to this semi-infinite set of equations is

$$
\left[\omega - \varepsilon_a - \Sigma^R_{aa}\right] G^R_{aa} = 1 + \Sigma^R_{ab} G^R_{ba}. \qquad (5.8)
$$

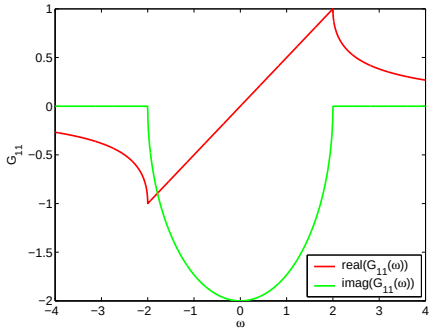

Figure 5.7: Plot of real and imaginary part of $\tilde{G}^R_{11}(\omega)$.

The selfenergy Σ^R_{ij} was found in App. E,

$$\Sigma^R_{ij} = \left(V^R_i V^R_j + V^L_i V^L_J\right) \tilde{G}^R_{11}, \tag{5.9a}$$

$$\tilde{G}^R_{11} = \frac{\omega/2t - \text{sign}(\omega)\sqrt{(\omega/2t)^2 - 1}}{t}, \tag{5.9b}$$

where $\tilde{G}^R_{11}$ is the full Green's function for the first site in the lead in absence of the quantum dot.

Similarly we find for G^R_{ba}

$$\left[\omega - \varepsilon_b - \Sigma^R_{bb}\right] G^R_{ba} = \Sigma^R_{ba} G^R_{aa}, \tag{5.10}$$

and hence the full solution for G^R_{aa},

$$G^R_{aa} = \frac{1}{\omega - \varepsilon_a - \Sigma^R_{aa} - \frac{\Sigma^R_{ab}\Sigma^R_{ba}}{\omega - \varepsilon_b - \Sigma^R_{bb}}}, \tag{5.11}$$

and similarly

$$G^R_{bb} = \frac{1}{\omega - \varepsilon_b - \Sigma^R_{bb} - \frac{\Sigma^R_{ba}\Sigma^R_{ab}}{\omega - \varepsilon_a - \Sigma^R_{aa}}}. \tag{5.12}$$

It should be mentioned that the single lead model *cannot* be mapped onto the two lead model by simply redefining the coupling constants, and hence the two models are indeed different.

5.6.1 Occupation

Having found $\tilde{G}^R_{11}(\omega)$ it is possible to find the spectral function and hence the occupations of the levels. The relevant selfenergies are

$$\Sigma^R_{aa}(\omega) = \left((V^R_a)^2 + (V^L_a)^2\right)\tilde{G}^R_{11}(\omega), \tag{5.13a}$$
$$\Sigma^R_{bb}(\omega) = \left((V^R_b)^2 + (V^L_b)^2\right)\tilde{G}^R_{11}(\omega), \tag{5.13b}$$
$$\Sigma^R_{ab}(\omega) = \left(V^R_a V^R_b + V^L_a V^L_b\right)\tilde{G}^R_{11}(\omega), \tag{5.13c}$$
$$\Sigma^R_{ba}(\omega) = \left(V^R_a V^R_b + V^L_a V^L_b\right)\tilde{G}^R_{11}(\omega), \tag{5.13d}$$

so that $\tilde{G}^R_{11}(\omega)$ essentially determines the complex structure of the selfenergies. In App. E we show that $\tilde{G}^R_{11}$ can be expressed as

$$\tilde{G}^R_{11}(\omega) = \begin{cases} \frac{\omega/2t}{t} - i\frac{\sqrt{1-(\omega/2t)^2}}{t}, & |\omega| < 2t, \\ \frac{\omega/2t - \mathrm{sign}(\omega)\sqrt{(\omega/2t)^2-1}}{t}, & |\omega| \geq 2t. \end{cases} \tag{5.14}$$

The occupation of the dot is found in exactly the same way as in the single lead setup in Sect. 4.7.1, using the Fluctuation Dissipation Theorem to rewrite the lesser Green's function

$$n_i(\mu) = \int_{-\infty}^{\mu} \frac{d\omega}{2\pi} A_i(\omega), \tag{5.15a}$$
$$A_i(\omega) \equiv -2\mathrm{Im}G^R_{ii}(\omega). \tag{5.15b}$$

Note that for the parameter values we use the renormalized levels remain within the band, but for other parameter values this might not be the case. Expresing the occupations analytically involves finding the imaginary part of the Green's function, which yields very large expressions that do not simplify, and we have therefore performed these calculations numerically for various combinations of couplings to the two leads, shown in Fig. 5.8.

5.6.2 Comparison

Having performed both exact Green's function and approximate DMRG calculations we are able to test the performance of DMRG in the non-interacting limit. In Fig. 5.9 both exact and DMRG results are plotted in rather consistency.

The agreement between the two is obvious, but there appear to be some numeric irregularities in the DMRG result, especially near the step in occupation. We expect that the majority of these problems would be eliminated by increasing the number of states kept at each DMRG step. There are two differences compared to the single lead setup, explaining the lesser precision: (i) For fixed number of states kept m the relative truncation in this setup is

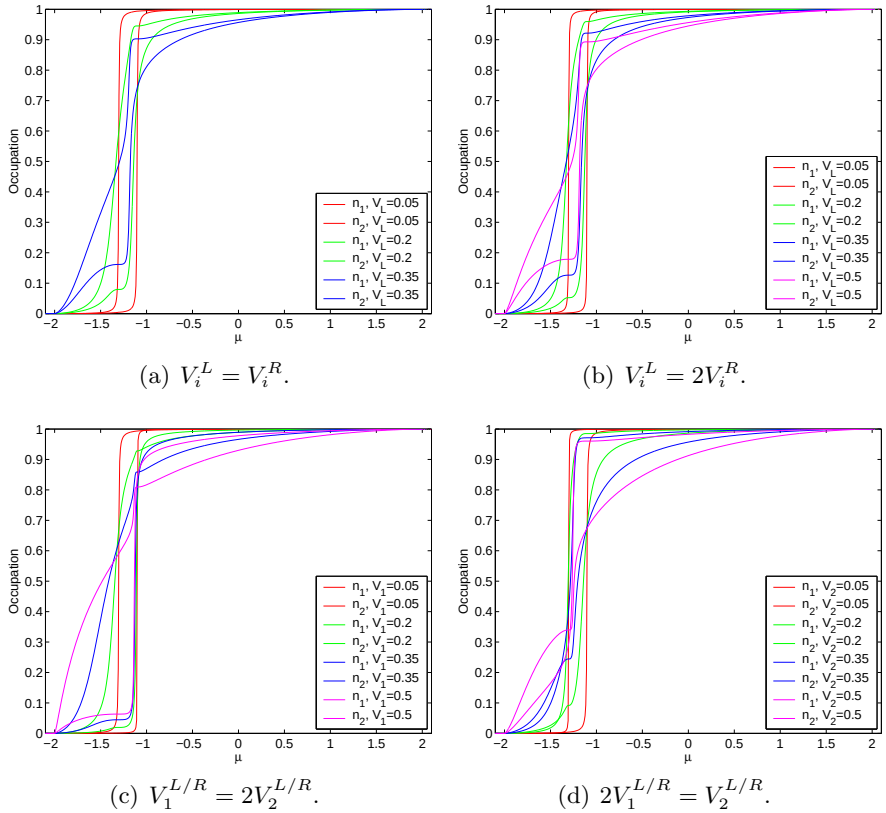

(a) $V_i^L = V_i^R$. (b) $V_i^L = 2V_i^R$.

(c) $V_1^{L/R} = 2V_2^{L/R}$. (d) $2V_1^{L/R} = V_2^{L/R}$.

Figure 5.8: Occupations in the non-interacting case for $\epsilon = [-1.3, -1.1]$, computed using Green's function theory. U, $V_i^{L/R}$, ϵ and μ are given in units of t.

bigger than in the single lead case. (*ii*) With the numbering of basis states used, the two leads in this setup are equivalent to a single lead with *only* next-nearest neighbor interactions. Thus this setup corresponds to a single lead setup with longer range interactions, which is computationally heavier, as argued in Sect. 2.6. Note, however, that enlarging only one lead at a time in the infinite system step might increase the precision, as discussed in Sect. 5.3.

5.7 Towards transport

To do transport using DMRG turned out to be unrealistic within the time limits of this project. However, to approach the subject we have calculated the occupation of the dot as a function of gate voltage when the chemical potentials of the two leads are different. We use the setup shown in Fig. 5.10.

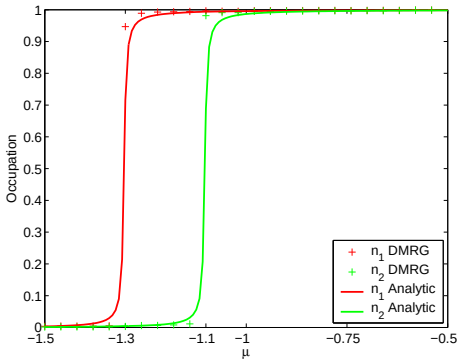

(a) $V_i^{L/R} = 0.05$.

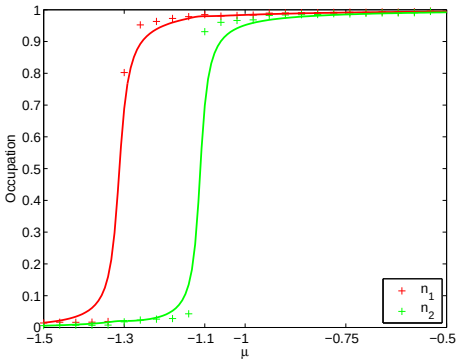

(b) $V_i^{L/R} = 0.1$.

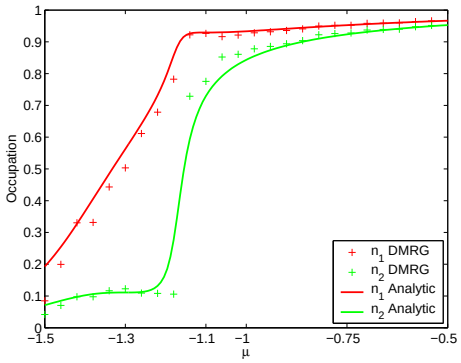

(c) $V_i^{L/R} = 0.25$.

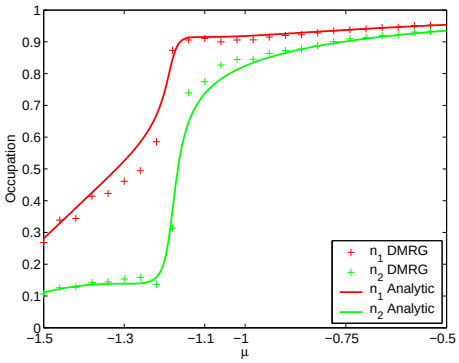

(d) $V_i^{L/R} = 0.3$.

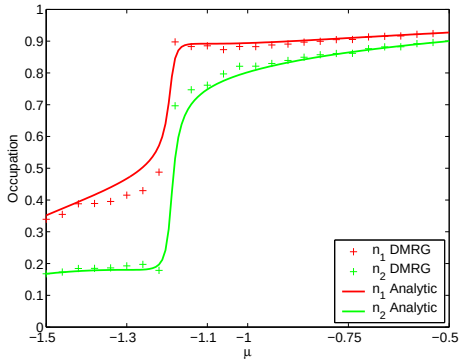

(e) $V_i^{L/R} = 0.4$.

Figure 5.9: Comparison between DMRG and analytic results for $\epsilon = [-1.3, -1.1]$, $m = 32$ states, and 125 sites in the lead. The agreement is fine but there are more numeric irregularities than in the single lead setup. U, $V_i^{L/R}$, ϵ, and μ are given in units of t.

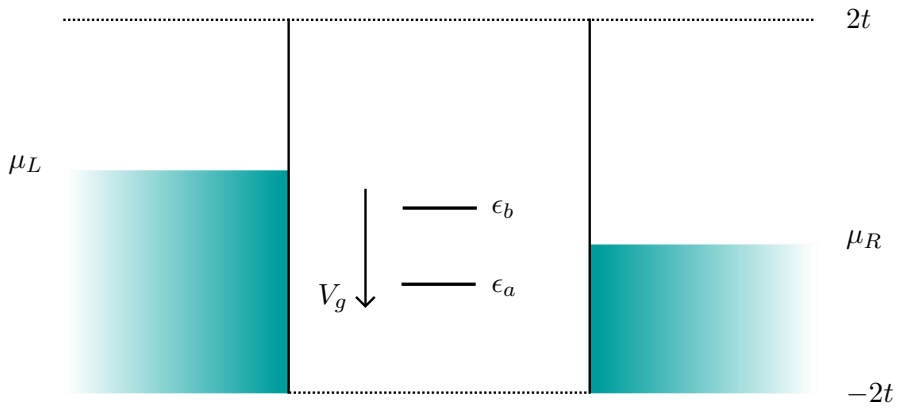

Figure 5.10: Biased quantum dot. Notice that we use indices a and b for the dot levels and $1, 2, \cdots$ for the lead sites and the different chemical potentials in the left and right leads.

5.7.1 Hamiltonian

The Hamiltonians are essentially unchanged, but the leads are assumed in equilibrium with different chemical potentials, μ_L and μ_R respectively, giving the total Hamiltonian

$$H = H_{Dot} + H_{Right\ Lead} + H_{Left\ Lead} + H_{DL} - \mu_R \sum_{j=1}^{\infty} c_j^\dagger c_j - \mu_L \sum_{j=1}^{\infty} c_{-j}^\dagger c_{-j}, \tag{5.16}$$

where H_{Dot}, $H_{Right\ Lead}$, $H_{Left\ Lead}$, and H_{DL} are given in Eq. (5.1) and (5.2a)-(5.2c).

5.7.2 Results

The DMRG implementation of the biased dot is essentially identical to the unbiased dot explained in Sect. 5.2 and 5.3 only here we distinguish different chemical potentials. We calculate the occupation of the dot versus gate voltage V_g for various couplings and on-site interactions. The parameter values used are $\mu_L = -\mu_R = 0.1$ and three different couplings $V_i^{L/R}$ between 0.5 and 0.05. For each set of parameters U, $V_i^{L/R}$, and V_g we do a full DMRG calculation of the occupation of the dot. In Fig. 5.11 and 5.12 we show plots of the occupation of the dot versus gate voltage calculated using DMRG. It should be noted that this calculation does not incorporate the finite bandwidth of this model, and hence allows filling of the dot even when the renormalized levels are outside the band. This contradicts energy conservation since there is no dissipation in this model.

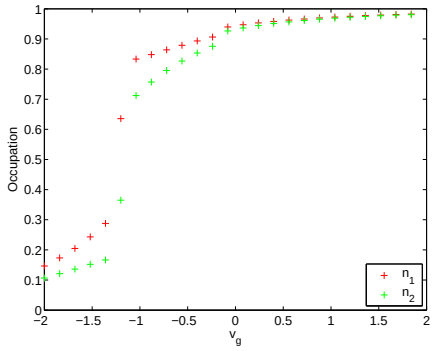

(a) $U = 0$, $V_i^{L/R} = 0.5$.

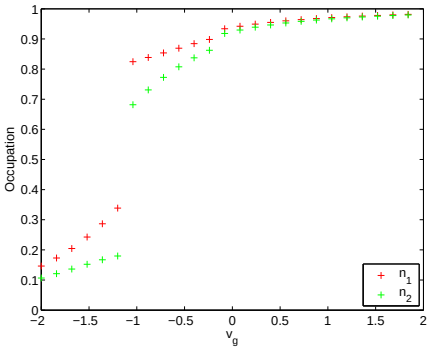

(b) $U = 0.1$, $V_i^{L/R} = 0.5$.

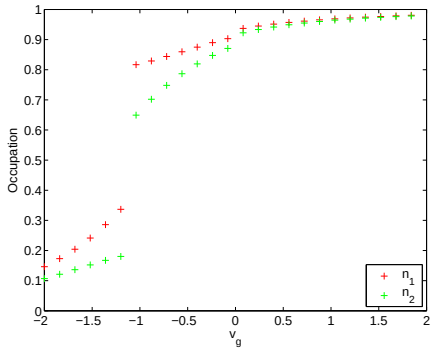

(c) $U = 0.2$, $V_i^{L/R} = 0.5$.

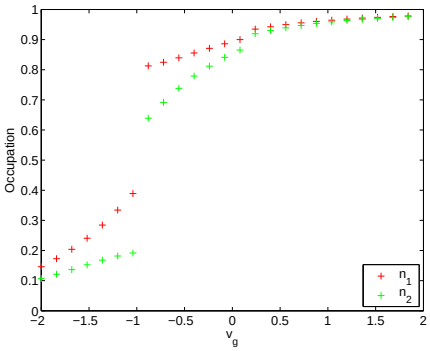

(d) $U = 0.4$, $V_i^{L/R} = 0.5$.

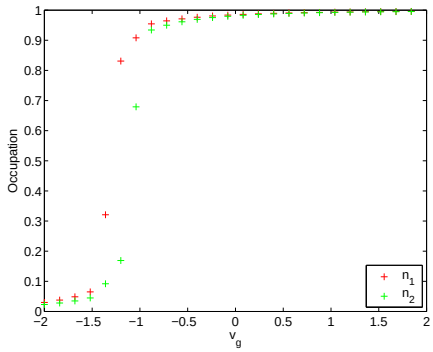

(e) $U = 0$, $V_i^{L/R} = 0.25$.

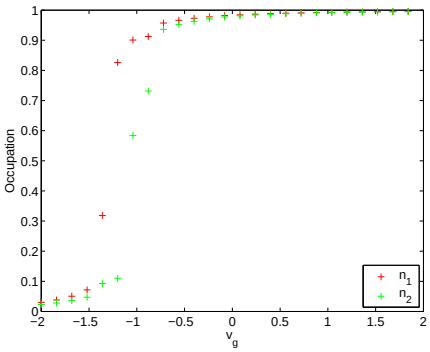

(f) $U = 0.1$, $V_i^{L/R} = 0.25$.

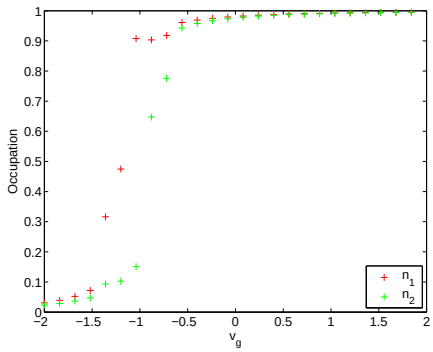

(g) $U = 0.2$, $V_i^{L/R} = 0.25$.

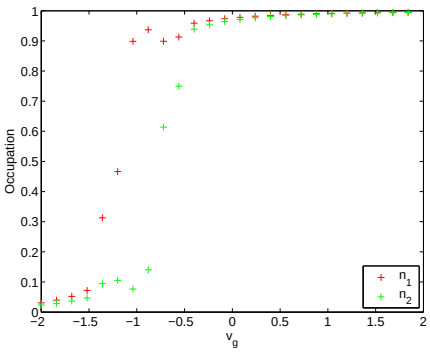

(h) $U = 0.4$, $V_i^{L/R} = 0.25$.

Figure 5.11: Occupations for $\epsilon = [-1.3, -1.1]$, $\mu_L = -\mu_R = 0.1$, $m = 32$ states, and 125 sites in the lead. U, $V_i^{L/R}$, ϵ, and V_g are given in units of t.

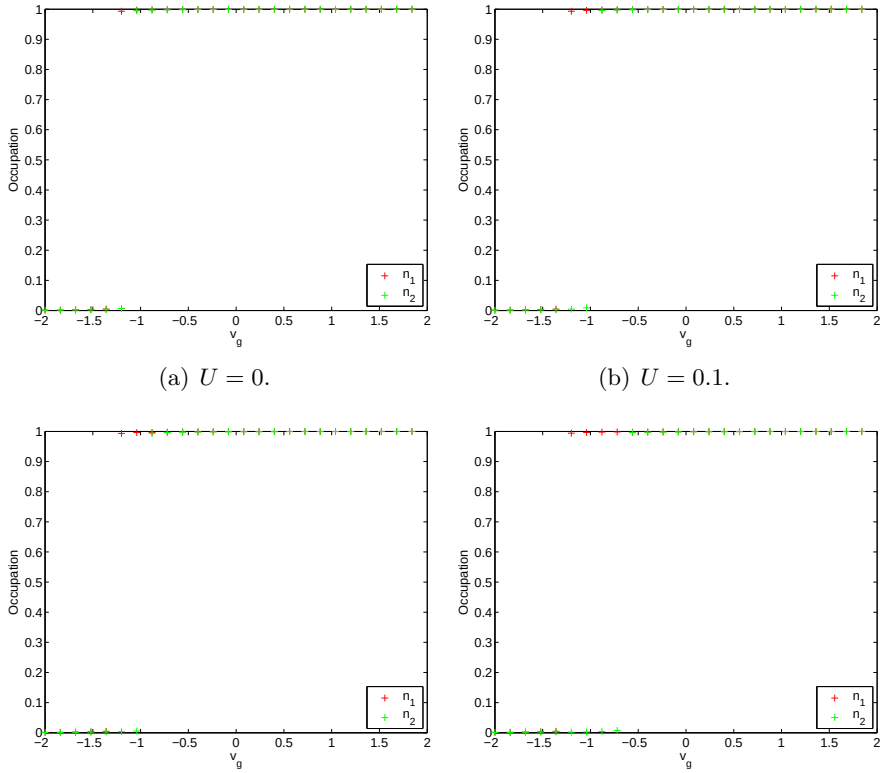

(a) $U = 0$. (b) $U = 0.1$.

(c) $U = 0.2$. (d) $U = 0.4$.

Figure 5.12: Occupations for $\epsilon = [-1.3, -1.1]$, $\mu_L = -\mu_R = 0.1$, $m = 32$ states, and 125 sites in the lead. U, $V_i^{L/R}$, ϵ, and V_g are given in units of t.

5.7.3 Analytic result

In the non-interacting limit we can calculate the occupation of the biased dot analytically, using again Green's function theory. The basic analysis is very similar to the analysis already presented, and again the convergence factor $\omega \to \omega + i\eta$ is not written explicitly. The EOM found in App. E can be written more intuitively in terms of the free Green's functions, $(g_i^R)^{-1} \equiv \omega - (\epsilon_i - V_g)$, and the selfenergies, $\Sigma_{ij}^R \equiv (V_i^L V_j^L + V_i^R V_j^R)\tilde{G}_{11}^R$,

$$\begin{aligned} \left[(g_a^R)^{-1} - \Sigma_{aa}^R)\right] G_{aa}^R &= 1 + \Sigma_{ab}^R G_{ba}^R \Rightarrow \\ \left[1 - g_a^R \Sigma_{aa}^R\right] G_{aa}^R &= g_a^R + g_a^R \Sigma_{ab}^R G_{ba}^R \Rightarrow \\ G_{aa}^R &= g_a^R + g_a^R \Sigma_{ab}^R G_{ba}^R + g_a^R \Sigma_{aa}^R G_{aa}^R. \end{aligned} \tag{5.17}$$

Similarly we find

$$G^R_{bb} = g^R_b + g^R_b \Sigma^R_{ba} G^R_{ab} + g^R_b \Sigma^R_{bb} G^R_{bb}, \tag{5.18a}$$
$$G^R_{ab} = g^R_a \Sigma^R_{aa} G^R_{ab} + g^R_a \Sigma^R_{ab} G^R_{bb}, \tag{5.18b}$$
$$G^R_{ba} = g^R_b \Sigma^R_{bb} G^R_{ba} + g^R_b \Sigma^R_{ba} G^R_{aa}. \tag{5.18c}$$

These equations are collected in matrix form,

$$\mathbf{G}^R = \mathbf{g}^R + \mathbf{g}^R \mathbf{\Sigma}^R \mathbf{G}^R, \tag{5.19}$$

where

$$\mathbf{G}^R = \begin{pmatrix} G^R_{aa} & G^R_{ab} \\ G^R_{ba} & G^R_{bb} \end{pmatrix}, \tag{5.20a}$$
$$\mathbf{g}^R = \begin{pmatrix} g^R_a & 0 \\ 0 & g^R_b \end{pmatrix}, \tag{5.20b}$$
$$\mathbf{\Sigma}^R = \begin{pmatrix} \Sigma^R_{aa} & \Sigma^R_{ab} \\ \Sigma^R_{ba} & \Sigma^R_{bb} \end{pmatrix}. \tag{5.20c}$$

Having verified that we can indeed write the Dyson equation for $\mathbf{G}^R$ Eq. (5.19) we can use a result from non-equilibrium Green's function theory,[2]

$$\mathbf{G}^< = \mathbf{G}^R \mathbf{\Sigma}^< \mathbf{G}^A, \tag{5.21}$$

where

$$G^A_{ij}(\omega, V_g) = \left(G^R_{ij}(\omega, V_g)\right)^*, \tag{5.22a}$$
$$\Sigma^<_{ij} = -2i\mathrm{Im}\big(\tilde{G}^R_{11}\big)\big(V^R_i V^R_j n^R_F(\omega) + V^L_i V^L_j n^L_F(\omega)\big). \tag{5.22b}$$

The notation $n^{L/R}_F(\omega)$ indicates that the chemical potential of the left and right leads are different,

$$n^{L/R}_F(\omega) = \frac{1}{e^{-\beta(\mu_{L/R}-\omega)}+1}, \tag{5.23}$$

and $\tilde{G}^R_{11}$ is again given by

$$\mathrm{Re}G^R_{11} = \frac{\omega/2t - \theta(|\omega|/2t-1)\mathrm{sign}(\omega)\sqrt{(\omega/2t)^2-1}}{t}, \tag{5.24a}$$
$$\mathrm{Im}G^R_{11} = \frac{-\theta(1-|\omega|/2t)\sqrt{1-(\omega/2t)^2}}{t}. \tag{5.24b}$$

[2] [18], p. 165-166. The derivation of this statement relies on the Keldysh formalism, defining generalized Green's functions on the Keldysh contour and extracting various real time Green's functions from this.

By matrix multiplication we find for the two levels on the dot,

$$G^<_{aa} = G^R_{aa}\Sigma^<_{aa}G^A_{aa} + G^R_{ab}\Sigma^<_{ba}G^A_{aa} + G^R_{aa}\Sigma^<_{ab}G^A_{ba} + G^R_{ab}\Sigma^<_{bb}G^A_{ba}, \quad (5.25a)$$
$$G^<_{bb} = G^R_{bb}\Sigma^<_{bb}G^A_{bb} + G^R_{ba}\Sigma^<_{ab}G^A_{bb} + G^R_{bb}\Sigma^<_{ba}G^A_{ab} + G^R_{ba}\Sigma^<_{aa}G^A_{ab}, \quad (5.25b)$$

where the retarded Green's functions were found in Sect. 5.6. Hence we may calculate the occupation of the dot in the standard way,

$$\begin{aligned} n_i(V_g) &\equiv \langle a_i^\dagger a_i \rangle \\ &= -iG^<_{ii}(t=0, V_g) \\ &= \int_{-\infty}^{\infty} \frac{d\omega}{2\pi i} G^<_{ii}(\omega, V_g). \end{aligned} \quad (5.26)$$

Plots of the occupation calculated using Eq. (5.26) as well as DMRG results are shown in Fig. 5.13. As discussed in App. F the spectral function, and hence $G^<$, may have δ-like peaks outside the band. Such peaks are very difficult to integrate numerically, and hence numerical imprecisions might be present in the numerical calculations of n_i for some values of V_g.

5.7.4 Comparison

Having calculated the occupation using both DMRG and analytic methods we are able to compare the two. In Fig. 5.13 we show both sets of results.

For small gate voltages these results agree quite well. There is however one feature of the analytic result that the DMRG results do not exhibit, namely the decrease of occupation when the gate voltage becomes sufficiently large to push the renormalized levels outside the band. The hopping matrix elements used in the DMRG calculation allows filling of the dot even when this is prohibited by energy conservation. Our DMRG implementation does not incorporate the finite bandwidth, explaining the deviation of the DMRG and analytic results. Probably a modification of the hopping matrix elements used in DMRG can remedy this.

Also in future calculations it would be interesting to use a finer grid of gate voltages near the unrenormalized level energies, and see if the DMRG results reproduce the detailed structure of the step-up in occupation.

5.7.5 Attempted current calculation

Naively one would expect that we might directly calculate $V_i^L\big(\langle a_i^\dagger c_1\rangle - \langle c_1^\dagger a_i\rangle\big)$ using DMRG, which apart from some factors is the static current through the dot,

$$J_L = \frac{ie}{\hbar}\sum_i V_i^L\big(\langle a_i^\dagger c_1\rangle - \langle c_1^\dagger a_i\rangle\big). \quad (5.27)$$

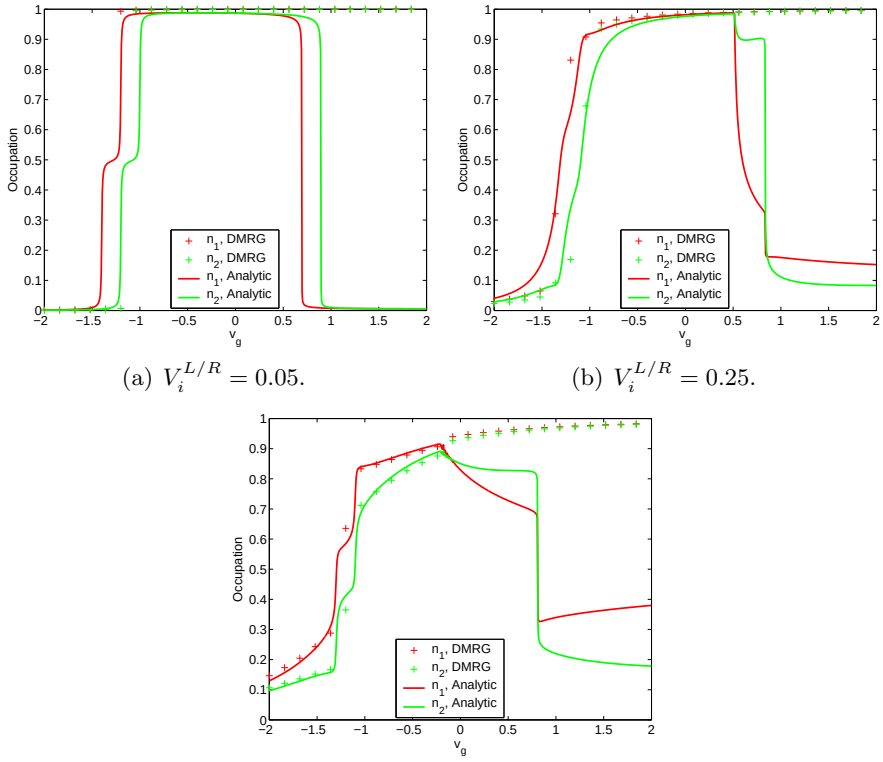

(a) $V_i^{L/R} = 0.05$.

(b) $V_i^{L/R} = 0.25$.

(c) $V_i^{L/R} = 0.5$.

Figure 5.13: Comparison between DMRG and analytic occupations for $\epsilon = [-1.3, -1.1]$, $\mu_L = -\mu_R = 0.1$, $m = 32$ states, and 125 sites in the lead. The large gate occupations are not reproduced by DMRG since we have not incorporated the finite band width in our implementation. U, $V_i^{L/R}$, ϵ, and V_g are given in units of t.

Very recently we experimented with this approach, but found it impossible to calculate the current, at least with this extremely simple approach. The DMRG results turned out to cancel identically, and the single contributions turned out to be real. In our DMRG approach there is no time dependence, which could explain this failure. Apparently the time dependence present in the Green's function result has been collapsed too soon. We consider current calculations as future work, and expect that more sophisticated methods are needed, [5, 6, 7].

5.8 Conclusions

Expanding on the implementation of Chap. 4 we have successfully implemented DMRG on a quantum dot coupled to two one-dimensional leads, in

the semi-infinite lead limit. We have performed virtually the same calculations as for the single lead setup, calculating the occupation of the dot as a function of chemical potential, for various couplings and on-site interactions and briefly commented on the results found. We compared DMRG to analytic data in the non-interacting limit, and found consistency, but to less extent than in the single lead case. We discussed possible explanations for this.

To take the first steps towards transport and to test the capability of DMRG we forced the dot out of equilibrium by using different chemical potentials in the left and right leads, calculating the occupation versus gate voltage on the dot. In the non-interacting limit we compared DMRG and analytic non-equilibrium Green's function results. For a limited range of gate voltages the two results are consistent, but the DMRG calculation does not reproduce the large gate behavior, when the renormalized dot levels are pushed outside the band. We explained the origin of this discrepancy and mentioned a possible solution.

Chapter 6

Single particle quantum mechanics

One very simple application of DMRG is on single particle quantum mechanics. Dealing with single particles does not really unlock the full potential of DMRG but the implementation is much simpler, making it a good starting point. This is due to the fact that the truncation usually performed via the reduced density matrix reduces to a simple projection of the wavefunction in this case.

In this section we follow Martín-Delgado *et al.* and calculate ground state energy and gap for a single particle on a tight binding chain in two different potentials using a simple DMRG implementation [20]. The article is pedagogical and well written and we will be brief in the explanation of the algorithm. For further details we refer to the article.[1]

6.1 Hamiltonian and matrices

The model considered is a single particle in a box experiencing a potential and represented classically by

$$H \;=\; p^2 + V(x), \tag{6.1}$$

where $V(x)$ is any potential. First we discretize the Hamiltonian by restricting x, $x_n = h(n - \frac{N+1}{2})$, where $n = 1, 2, \cdots, N$. The parameter h gives the size of the box in which the particle is confined, $\Delta x = x_N - x_1 = h(N-1)$. With these definitions the Hamiltonian becomes

$$H \;=\; \begin{cases} \frac{2}{h^2} + V(x_n), & n = m, \\ -\frac{1}{h^2}, & n = m \pm 1, \\ 0, & \text{otherwise.} \end{cases} \tag{6.2}$$

[1] For the historically interested, single particle quantum mechanics using DMRG is interesting since it was the failure of Wilson's numerical renormalization group on this type of problems that lead White to formulate DMRG.

Using an ordinary superblock setup we find the generic superblock Hamiltonian,

$$H_{SB} = \begin{pmatrix} H_L & -v_L & 0 & 0 \\ -v_L^\dagger & h_{CL} & -1/h^2 & 0 \\ 0 & -1/h^2 & h_{CR} & -v_R^\dagger \\ 0 & 0 & -v_R & H_R \end{pmatrix}, \tag{6.3}$$

where H_L and v_L represent the (possibly truncated) Hamiltonian of the left block and interaction of the left block with the first central site, and similar for the right block.

Due to the single particle nature of the problem each state is described by a single degree of freedom – and hence H_{SB} has dimensions $(2N_E + 2) \times (2N_E + 2)$, where N_E is the total number of target states for each block.

6.2 Algorithm

In this section we show that the eigenstates of the reduced density matrix (RDM) in the single particle problem reduces to a projection of the wavefunction, and review the DMRG algorithms.

6.2.1 RDM for single particle problems

In single particle problems the complete basis consists of single particle states, located at the different sites in the chain. To express the state of the superblock in terms of product states we need an enlarged basis of the superblock, containing both zero and two particle states. We use the notation of Noack and White and denote the states of the enlarged basis for the left block as

$$\begin{aligned} &\big|0\big\rangle_L, && \text{(6.4a)} \\ &\big|1\big\rangle_L = c_1^\dagger \big|0\big\rangle_L, && \text{(6.4b)} \\ &\quad\vdots \\ &\big|l\big\rangle_L = c_l^\dagger \big|0\big\rangle_L, && \text{(6.4c)} \end{aligned}$$

with similar definitions for the right block [2]. Index l denotes the rightmost site of the left block, so that the first site in the environment block is $l + 1$. Denoting additionally the ground state wavefunction

$$\big|\psi\big\rangle = (\psi_1, \psi_2, \cdots, \psi_l, \psi_{l+1}, \cdots, \psi_L), \tag{6.5}$$

where L is the total chain length we find the ground state matrix in the usual way,

$$\psi = \begin{pmatrix} 0 & \psi_{l+1} & \cdots & \psi_L \\ \psi_1 & 0 & & 0 \\ \vdots & & \ddots & \vdots \\ \psi_l & 0 & \cdots & 0 \end{pmatrix}, \tag{6.6}$$

where it is clearly seen that only one particle states enter. By matrix multiplication the reduced density matrix becomes

$$\rho = \psi\psi^\dagger = \begin{pmatrix} \sum_{j=l+1}^{L} \psi_j^2 & 0 & 0 & \cdots & 0 \\ 0 & \psi_1^2 & \psi_1\psi_2 & \cdots & \psi_1\psi_l \\ 0 & \psi_2\psi_1 & \psi_2^2 & \cdots & \psi_2\psi_l \\ \vdots & \vdots & \vdots & \ddots & \vdots \\ 0 & \psi_l\psi_1 & \psi_l\psi_2 & \cdots & \psi_l^2 \end{pmatrix}. \tag{6.7}$$

The spectrum of this matrix is very simple, containing only two non-zero eigenvalues, with the corresponding normalized eigenvectors

$$v_1 = (1, 0, \cdots, 0), \tag{6.8a}$$

$$v_2 = \frac{1}{\sqrt{\sum_{i=1}^{l} \psi_i^2}} (0, \psi_1, \psi_2, \cdots, \psi_l). \tag{6.8b}$$

The first eigenvector does not need to be considered since the only nonzero entry corresponds to a zero particle state. Hence the best state to retain for the left block is $(0, \psi_1, \psi_2, \cdots, \psi_l)$, given the ground state vector Eq. (6.5), or removing the zero particle state,

$$v = (\psi_1, \psi_2, \cdots, \psi_l) \tag{6.9}$$

As in Sect. 2.1 this derivation generalizes when targeting N_E states, i.e. targeting additionally $N_E - 1$ exited states, where you get N_E optimal states, conveniently collected in a matrix

$$O = \begin{pmatrix} \psi_{1,1} & \cdots & \psi_{1,N_E} \\ \psi_{2,1} & \cdots & \psi_{2,N_E} \\ \vdots & & \vdots \\ \psi_{l,1} & \cdots & \psi_{l,N_E} \end{pmatrix}. \tag{6.10}$$

6.2.2 Particle in a box

Targeting N_E states in the left and right blocks the superblock Hamiltonian can be written as in Eq. (6.3), where H_L and H_R are $N_E \times N_E$ matrices and

v_L and v_R are N_E component column vectors. Each eigenstate of the superblock is a $2N_E+2$ component vector. Denoting the N_E lowest eigenstates of the superblock Hamiltonian by

$$(\bar{\psi}_{L,i}, \psi_{CL,i}, \psi_{CR,i}, \bar{\psi}_{R,i}), \quad i = 1, 2, \cdots, N_E, \tag{6.11}$$

where $\bar{\psi}_{L/R,i}$ are vectors, we find the projection of each target state onto the enlarged left block by the set of vectors $(\bar{\psi}_{L,i}, \psi_{CL,i})$, as shown above. These states are orthonormalized explicitly.

Hence including the central state CL into the left block we have the truncation onto a N_E component DMRG basis given by the matrix

$$O \;=\; \begin{pmatrix} \bar{\psi}_{L,1} & \cdots & \bar{\psi}_{L,N_E} \\ \psi_{CL,1} & \cdots & \psi_{Cl,N_E} \end{pmatrix}, \tag{6.12}$$

or explicitly the new left block Hamiltonian

$$H'_L \;=\; O^\dagger \begin{pmatrix} H_L & -v_L \\ -v_L^\dagger & h_{CL} \end{pmatrix} O, \tag{6.13}$$

and the new interaction with the central site,

$$v'_{L,i} \;=\; \psi_{CL,i}, \quad i = 1, 2, \cdots, N_E. \tag{6.14}$$

This interaction is not found using DMRG arguments but by noting that $\psi_{CL,i}$ is the probability of finding the particle on the old central site for the state i.

We complete the generic DMRG step by renaming

$$v'_{L,i} \;\rightarrow\; v_{L,i}, \tag{6.15a}$$
$$H'_L \;\rightarrow\; H_L. \tag{6.15b}$$

Similar relations exist for the right block.

6.2.3 Infinite system sweep

We scale all arguments by h^2 to get consistency with [20]. We initialize the infinite system procedure by defining

$$H_L \;=\; \begin{pmatrix} 2 + h^2 V(x_1) & -1 \\ -1 & 2 + h^2 V(x_2) \end{pmatrix}, \tag{6.16a}$$
$$v_L \;=\; \begin{pmatrix} 0 \\ 1 \end{pmatrix}, \tag{6.16b}$$

and

$$h_{CL/CR} \;=\; 2 + h^2 V(x_{3/4}), \tag{6.17}$$

and similar expressions for the right block. Hence the initial superblock Hamiltonian is

$$H_{SB} = \begin{pmatrix} H_L & -v_L & 0 & 0 \\ -v_L^\dagger & 2+h^2V(x_3) & -1 & 0 \\ 0 & -1 & 2+h^2V(x_4) & -v_R^\dagger \\ 0 & 0 & -v_R & H_R \end{pmatrix}, \tag{6.18}$$

where the number of sites is $N = 6$.

At each step the left and right blocks are enlarged by one state and truncated as explained in the previous subsection. This is repeated until the total number of sites in the system reaches the desired value N. At each step all matrices for the left and right block should be stored. Note that the size of the box in which the particle is confined Δx is kept constant, only the number of allowed positions N is increased.

6.2.4 Finite system sweeps

In this part the number of sites in the system is kept constant, but the sizes of the left and right blocks are varied. The basic left to right step is enlarging the left block by one site and truncating as explained above. Then form a superblock using this enlarged left block, two central sites and a right block with one state less. This right block has been found and stored during the infinite system sweep.

This procedure is repeated until the right block consists of N_E states, i.e. until the description of the right block is exact. Then the roles of right and left are reversed and we iterate until the left block contains only N_E states. We repeat this zipping back and forth until convergence is reached, typically around 10 times.

6.3 Results

Using the algorithm described above and targeting only one exited state ($N_E = 2$) we are able to calculate the ground state energy and energy gap for various potentials. We have considered two different potentials, the harmonic potential and the double well potential,

$$V_{\text{harmonic}}(x) = x^2, \tag{6.19a}$$

$$V_{DW}(x) = -x^2 + Cx^4. \tag{6.19b}$$

A few results calculated using this DMRG scheme are shown in Tab. 6.1 for the harmonic potential and Tab. 6.3 for the double well potential. The corresponding data presented by Martín-Delgado *et al.* are shown in Tab. 6.2 and 6.4. It should be mentioned that these results require only modest computer power compared to the results presented in chapters 3, 4, and 5, as the superblock matrices in this setup are only 6×6.

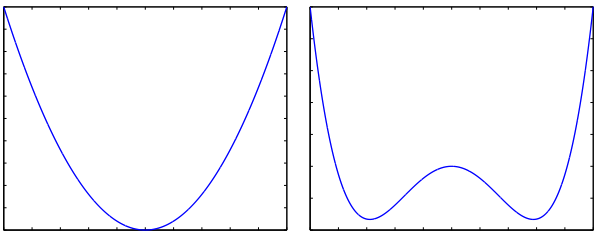

(a) $V(x) = x^2$. (b) $V(x) = -x^2 + Cx^4$.

Figure 6.1: Harmonic and double well potentials in arbitrary units.

N	h	$1 - E_0$	$3 - E_1$
1000	0.01	6.24989×10^{-6}	3.1243338×10^{-6}
5000	0.002	2.498×10^{-7}	1.2427×10^{-6}

Table 6.1: DMRG results for the harmonic potential.

N	h	$1 - E_0$	$3 - E_1$
1000	0.01	$6.24989(322) \times 10^{-6}$	$3.1243338(564) \times 10^{-6}$
5000	0.002	$2.498(36) \times 10^{-7}$	$1.2427(28) \times 10^{-6}$

Table 6.2: DMRG results from [20] for the harmonic potential.

C	N	h	E_0	Δ
1	1000	0.01	0.65764425361	2.176825710
0.6	20000	0.0005	0.39195261	1.6332847
0.06	60000	0.0005	-2.82363949	0.0072997661

Table 6.3: DMRG results for the double well potential.

C	N	h	E_0	Δ
1	1000	0.01	0.65764425361(29)	2.176825710(298)
0.6	20000	0.0005	0.39195261(873)	1.6332847(928)
0.06	60000	0.0005	-2.82363949(203)	0.0072997661(673)

Table 6.4: DMRG results from [20] for the double well potential.

6.3.1 Comparison

Our DMRG result agrees completely with the data presented by Martín-Delgado *et al.* and one could proceed and explore e.g. the continuum limit of single particle quantum mechanics. It is not the purpose of the present thesis to do that. Further details of the physics of these models can be found in [20].

6.4 Conclusions

In this section we used a simpler formulation of DMRG to calculate properties of a particle in a box, experiencing two different potentials. Results obtained with our implementation were compared to those presented by Martín-Delgado *et al.*, showing complete consistency.

We showed explicitly that in the single particle case the projection of DMRG, usually done via the reduced density matrix, reduces to a projection of the target state wavefunction, making the DMRG implementation much simpler. All the calculations presented here could have been performed using the full machinery of DMRG, defining the reduced density matrix, diagonalizing it, computing the retained eigenstates etc. The simplicity of the single particle DMRG makes it a good starting point for DMRG calculations.

Chapter 7

Future work

Implementing DMRG turned out to be much more difficult than understanding the theoretical framework. We spent long time learning the basic concepts of DMRG, setting up matrix representations of operators etc. Many extensions of basic DMRG have been proposed, either speeding up calculations or expanding the capability of DMRG. We have considered only a few such additional schemes.

In this chapter we discuss improvements of our implementation of DMRG as well as several extensions that enable calculations beyond basic DMRG. Some extensions are highly non-trivial and require thorough studies of the literature, while others are more straight forward.

7.1 Improvements

7.1.1 Quantum numbers

So far our implementation has not been focused on the use of quantum numbers to label the basis states, since this implies programmatic difficulties in MatLab. However, in all models we have considered there are a number of good quantum numbers that can be used to label the states, such as particle number and spin.

As explained in Sect. 2.4.1 the use of quantum numbers potentially speeds up the DMRG calculation substantially, due to the decomposition of the full Hilbert space into subspaces. Since storing small dense matrices is more efficient than storing large sparse matrices, also the memory required is reduced, making the use of quantum numbers inevitable if larger systems are to be considered, or more states are to be kept.

Efficient programming in MatLab implies using the internal matrix structure, organizing data in matrices and vectors. This has some obvious advantages in DMRG but there are also drawbacks; reordering of basis states in the superblock may sometimes be desirable. In MatLab such reorderings of superblock states are easily performed, according to various

criterions. A rearrangement of the superblock basis corresponds to a rearrangement of the basis of the individual blocks, and it is non-trivial to link these basis rearrangements to each other. Likewise it is difficult to organize the basis states of the individual blocks such that the superblock automatically is in quantum number block structure. Hence it is not trivial to identify and calculate in a given subspace of the superblock when using MatLab.

We expect that object oriented programming would facilitate the solution of these issues. A block object could contain relevant subspaces and a loop over quantum numbers could then construct a superblock Hamiltonian in a basis ordered according to quantum numbers. Of course this is also possible in MatLab but it is less obvious how to construct a fast routine incorporating these features.

7.1.2 Wave function transformations

The most time consuming part of the DMRG algorithm is computing the ground state of the superblock Hamiltonian. Usually an iterative scheme like the Lanczos or Davidson algorithm is used. Most implementations of such diagonalization schemes use an arbitrary starting vector for the iterative procedure, making many iterative steps necessary to converge to the ground state. If a good guess for the ground state can be provided a significantly smaller number of iterations are needed, speeding up the calculation.

In the DMRG scheme a good guess to the current ground state is the ground state vector from the previous iteration, since the two superblocks have almost identical configurations. To use this initial guess the basis of the ground state vector from the previous DMRG iteration must be shifted into the basis of the current iteration, as discussed in Sect. 2.4.2.

7.1.3 Programming language

We chose to do all programming in MatLab due to prior knowledge of that program. However it appears that many mathematical algorithms and packages exist for languages like Python and C++, facilitating implementations in these languages as well. Since most algorithms within these languages are based on fortran or C codes better performance could probably be achieved in either of these languages. Due to the limited time available we chose to continue using MatLab, but long term DMRG work is likely to benefit from using Python or C++. The block structure of DMRG appeals to object oriented programming, where a nice organization can be made, and we expect that organizing the code using quantum numbers is easier using objects, as mentioned in Sect. 7.1.1.

Storing matrices in MatLab is done in non-sparse multidimensional arrays that are initialized with a given fixed size. This is an inefficient and not very flexible way of storing data, since such storage arrays can only

hold matrices of a given size. In object oriented languages we expect that both efficient and flexible storage could be implemented, reducing memory requirements and increasing the flexibility of the program.

7.1.4 Diagonalization routine

As mentioned in Sect. 2.2.3 Noack and White [2] device a ground state computation scheme in which the construction of the full superblock Hamiltonian matrix can be avoided. Incorporating this would reduce memory requirements and speed up the ground state computation itself. Since the most time consuming part of the algorithm is the computation of the ground state of the superblock Hamiltonian a total speed up is expected.

It is our belief that this improvement is highly non-trivial and requires thorough studies of the Lanczos or Davidson methods, as well as construction of specialized diagonalization routines.

7.1.5 Further benchmarks

So far we have tested the performance of DMRG in the non-interacting limit for the various models. For the Hubbard model we have only benchmarked the ground state energy and the total spin of the ground state in the non-interacting limit. To test further the capability and precision of our DMRG implementations it would be interesting to compare DMRG calculations to analytics in the interacting cases. No complete solutions exist for arbitrary U in the various models but in certain limits perturbative results or simple approximations may apply, making it possible to explore the precision of DMRG in these limits.

A 'selfconsistent' test of DMRG, by comparing results calculated using different number of states m, would also be interesting. This requires more efficient implementations of DMRG, since we are not able to increase m very much further than the values used in this work. In the Hubbard model, where also exited states of the final superblock are considered it would be interesting to include these as target states in the DMRG calculation, and see if the description of the exited states of the final superblock is improved. Probably more than $m = 24$ states are needed since the general precision of DMRG decreases when more states are targeted. We expect future more efficient implementations of DMRG on the models considered in this work would enable us to perform such selfconsistent tests.

7.2 Extending the capability of DMRG

7.2.1 Transport

One interesting application would be to calculate transport properties of one-dimensional systems using DMRG. In this work we have only approached transport slightly in Sect. 5.7, where we used different chemical potentials in the left and right lead. We attempted to calculate the current using a very simple approach, which turned out to be insufficient.

Recently two articles on transport using DMRG appeared on the preprint archive, by White and Feiguin [6] and by Schmitteckert [5]. Both articles expand DMRG to include time evolution, and are hence able to calculate properties of strongly correlated system out of equilibrium. Schmitteckert argues that his method uses no further approximations than the DMRG truncation, making it very interesting. Both articles could provide a DMRG method for calculating transport, and would be interesting to study in further detail.

7.2.2 Phonons

One of the hot subjects these days is the coupling of electrons to phonons in various systems [21, 22, 23]. Many of these systems would be interesting to study using non-perturbative methods, but also very challenging to implement in DMRG. This is due to the fact that the Hilbert space of bosons is large (in principle infinite), and that DMRG performs poorly if a large Hilbert space is added at every step. Hence a mapping from the single site large bosonic Hilbert space onto multiple pseudo sites with small Hilbert spaces is needed in order for the DMRG to perform effectively, making bosonic Hilbert spaces more challenging to treat in DMRG. More information on treating bosonic Hilbert spaces in DMRG can be found in the work of Jeckelmann and White on the Holstein model [24].

7.2.3 Dynamic properties

Several schemes to calculate dynamical properties using DMRG have been proposed. We have used a very basic method in our attempt to calculate a spectral function using DMRG. The goal was to see if we could get some dynamical results using DMRG, rather than to get accurate results.

There are several candidates in the literature for efficient and precise calculations of dynamics using DMRG, among those Jeckelmann's Dynamical DMRG [7], Kühner and White's DMRG scheme in [25], Schmitteckert's non-equilibrium transport using DMRG [5] and White and Feiguin's real time evolution using DMRG in [6]. Any of those deserves attention on their own, and probably a thorough study of these methods would make accurate calculations of dynamics possible within the framework of DMRG.

Chapter 8

Summary and outlook

In the past decade DMRG has been established as a very powerful numerical tool, and today it is used by many groups around the world. In this section we summarize our work, give a short presentation of the current status of DMRG and discuss the perspectives of DMRG.

8.1 Summary

With this work we have taken the initial steps towards establishing DMRG as a tool within the Theoretical Nanotechnology group at MIC. We have successfully implemented ordinary DMRG on the one-dimensional Hubbard chain with zero and finite magnetic field, and on a two level quantum dot coupled to one and two semi-infinite leads.

For the Hubbard chain we used our implementation to calculate the energy, particle number and spin of the lowest eigenstates varying both length and on-site repulsion. We included a small magnetic field in the DMRG calculation, and studied the effect on the low energy properties of the model. In the non-interacting limit and with vanishing magnetic field we compared the DMRG ground state energies to analytical results and found very good agreement.

We calculated the occupation of the quantum dot as a function of chemical potential varying the coulomb interaction on the dot and couplings to the leads. With two leads we additionally made calculations on a biased dot, calculating the occupation versus gate voltage for different couplings and coulomb interactions. In the non-interacting limit analytic results were computed in both the single and double lead case, and we compared these to DMRG results and found good agreement when sufficiently many states were retained in the DMRG truncation. For the biased dot we found good agreement for small gate voltages, where the renormalized dot levels remain inside the band. For larger gate voltages analytic and DMRG results deviate qualitatively from each other since our DMRG algorithm does not incorporate the finite bandwidth in the model. Finally we attempted a

very simple calculation of the static current through the dot. However the method turned out to be insufficient for calculating the current.

A simpler version of DMRG on single particle quantum mechanics was reviewed, and we showed explicitly how the DMRG truncation reduces to a projection of the wavefunction. We implemented this on a particle in a box experiencing a potential, and calculated the ground state energy and energy gap. This implementation is simpler than the full DMRG implementation, making it a suitable starting point for DMRG calculations.

We reviewed the limitations of our implementations and considered possible solutions to these issues. Several improvements, rendering the code faster or more reliable were discussed, and a number of schemes extending the capability of DMRG was mentioned. Of particular interest to this work is extensions to calculate dynamical properties and transport.

8.2 Outlook

When studying DMRG a one year master project is very short time and this project leaves many open ends. Having no prior knowledge of DMRG we had to focus our attention on ordinary DMRG calculations before considering various extensions. We managed to get ordinary DMRG under control as well as consider a few extensions.

In the literature however the usage of DMRG has been extended to very different systems, ranging from *ab initio* quantum chemistry calculations over applications in high-energy physics to transport in nanostructures. The wide range of problems to which DMRG has already been applied indicates the versatility of the general idea; while White formulated DMRG for quantum lattice systems the general concept of optimizing some functional using DMRG ideas appears to apply in very many other cases. Obviously DMRG and its extensions constitute a very powerful and relevant numerical tool, undergoing continuous development.

Nanotechnology and properties of nanoscale physical systems is receiving much attention these years, theoretically as well as experimentally. In general nanoscale systems are strongly correlated and hence difficult to treat using standard methods. DMRG could turn out to be particularly interesting when treating these systems theoretically and might be predictive once parameters have been estimated from experiments.

When doing transport the usual setup is ideal non-interacting leads connecting the system of interest to large particle reservoirs, hence keeping the leads in equilibrium. However this distinction looses the physical rationale for some setups, particularly when the leads are one-dimensional such as carbon nanotubes and atomic wires, where the underlying Fermi liquid theory breaks down. Traditional methods are thus not able to properly handle such situations. Contrary DMRG is able to handle interactions also in the

leads, eliminating the distinction between non-interacting leads and an interaction region, and may therefore be able to give results for such system. It should be noted that setups using carbon nanotubes as leads are being used experimentally at MIC.

Recent developments of DMRG have been in the direction of transport and the calculation of dynamical properties. A number of methods have been proposed, particularly Schmitteckert calculates the transport through a quantum dot, formulated in terms of wavepackets evolving in time in a properly truncated DMRG Hilbert space [5].

Much work still remains before we are able to perform efficient transport calculations. We hope to continue this work in the direction of transport within the Ph.D. programme at DTU. The ultimate goal is to formulate and implement a transport theory using DMRG, and while ordinary DMRG is now mainly under control it is clear that this is a very challenging task, theoretically as well as numerically. Despite the many proposed schemes in the literature transport using DMRG is still an unsettled and active research area.

Appendix A

Observables

In this appendix we show explicitly the equivalence between the two methods of calculating observables within the DMRG. We denote by A any system operator.

Method 1

The first method uses

$$\begin{aligned} \langle A \rangle &= \mathrm{Tr}[\rho A] \\ &= \sum_{i,i'=1}^{m} \sum_{j=1}^{n} \psi_{ji}^{\dagger} A_{ii'} \psi_{i'j}, \end{aligned} \tag{A.1}$$

where A is described in the basis of the system block, m denotes the number of system states and n denotes the number of environment states.

Method 2

The second method is

$$\langle A \rangle = \sum_{k,l=1}^{mn} \psi_k^{\dagger} \tilde{A}_{kl} \psi_l, \tag{A.2}$$

where $\tilde{A} = A \otimes \delta_n$, i.e. the matrix representation of A is in the basis of the superblock, and ψ is the column superblock ground state vector. m denotes the number of system states and n denotes the number of environment states.

Equivalence

To show that the two apparently different methods are in fact identical we consider Eq. (A.1),

$$\langle A \rangle = \sum_{i,i'=1}^{m} \sum_{j=1}^{n} \psi_{ji}^{\dagger} A_{ii'} \psi_{i'j}, \tag{A.3}$$

where m denotes the number of system states and n denotes the number of environment states.

Using the construction of matrix $\underline{\underline{\psi}}$,

$$\underline{\underline{\psi}} = \begin{pmatrix} \psi_1 & \psi_2 & \cdots & \psi_n \\ \psi_{n+1} & \psi_{n+2} & \cdots & \psi_{2n} \\ \vdots & & & \vdots \\ \psi_{(m-1)n+1} & \psi_{(m-1)n+2} & \cdots & \psi_{mn} \end{pmatrix}, \tag{A.4}$$

we rewrite this in terms of the vector ψ,

$$\psi_{i'j} = \psi_{(i'-1)n+j}, \tag{A.5a}$$

$$\psi^\dagger_{ji} = \psi^*_{j+(i-1)n}, \tag{A.5b}$$

where m denotes the total number of states in the system block and n denotes the total number of states in the environment block.

Writing out in detail Eq. (A.2) gives

$$\begin{aligned} \langle A \rangle &= \psi^\dagger (A \otimes \delta_n) \psi \\ &= \begin{pmatrix} \psi^*_1 & \cdots & \psi^*_{mn} \end{pmatrix} \begin{pmatrix} A_{11}\delta_n & A_{12}\delta_n & \cdots & A_{1m}\delta_n \\ A_{21}\delta_n & A_{22}\delta_n & \cdots & A_{2m}\delta_n \\ \vdots & \vdots & & \vdots \\ A_{m1}\delta_n & A_{m2}\delta_n & \cdots & A_{mm}\delta_n \end{pmatrix} \begin{pmatrix} \psi_1 \\ \vdots \\ \psi_{mn} \end{pmatrix}, \end{aligned} \tag{A.6}$$

where δ_n is an $n \times n$ unit matrix in the Hilbert space of the environment. Multiplying $\psi^\dagger$ and $A \otimes \delta_n$ gives an $m \cdot n$ component row vector. A careful index analysis reveals that the vector can be written

$$\left[\psi^\dagger (A \otimes \delta_n)\right]_{j+(i'-1)n} = \sum_{i=1}^{m} \psi^*_{j+(i-1)n} A_{ii'}, \tag{A.7}$$

with $j = 1, 2, \cdots, n$ and $i' = 1, 2, \cdots, m$. Hence the final multiplication in Eq. (A.6),

$$\langle A \rangle = \sum_k \left[\psi^\dagger (A \otimes \delta_n)\right]_k \psi_k, \tag{A.8}$$

where $k = j + (i' - 1)n$, yields

$$\langle A \rangle = \sum_{i,i'=1}^{m} \sum_{j=1}^{n} \psi^*_{j+(i-1)n} A_{ii'} \psi_{(i'-1)n+j}, \tag{A.9}$$

or using Eq. (A.5),

$$\langle A \rangle = \sum_{i,i',j} \psi^\dagger_{ji} A_{ii'} \psi_{i'j}, \tag{A.10}$$

and hence the two methods differ only by arrangement of the data.

Applications

Which of the two methods is most conveniently used depends on the representation of the data. The eigenstate routines used in this work returns eigenstates in column vector form and hence in some cases the second method is most favorable. Also when calculating properties of the superblock *only* the second method is applicable.

The first method is most favorable when calculating properties of the system throughout the DMRG calculation since the state matrix $\underline{\underline{\psi}}$ and operator matrix A is constructed at each step anyway, and hence the expectation value can be found very fast by matrix multiplication.

Appendix B

Properties of the Lanczos basis

In this appendix we demonstrate explicitly the orthogonality of the Lanczos basis.

B.1 Definition

The Lanczos basis is defined by

$$\big|f_{n+1}\big\rangle \;=\; H\big|f_n\big\rangle - a_n\big|f_n\big\rangle - b_n^2\big|f_{n-1}\big\rangle, \tag{B.1}$$

where

$$a_n \;=\; \frac{\big\langle f_n\big|H\big|f_n\big\rangle}{\big\langle f_n\big|f_n\big\rangle}, \tag{B.2a}$$

$$b_n^2 \;=\; \frac{\big\langle f_n\big|f_n\big\rangle}{\big\langle f_{n-1}\big|f_{n-1}\big\rangle}, \tag{B.2b}$$

$$\big|f_0\big\rangle \;=\; A\big|\psi_0\big\rangle, \tag{B.2c}$$

$$b_0^2 \;=\; 0, \tag{B.2d}$$

and where A is the operator for which we want to construct the basis.

B.2 Orthogonality of basis

First we demonstrate orthogonality for the first Lanczos basis states.

$\big|f_1\big\rangle$**:**

$$\big|f_1\big\rangle \;=\; H\big|f_0\big\rangle - a_0\big|f_0\big\rangle, \tag{B.3a}$$

$$\big\langle f_0\big|f_1\big\rangle \;=\; \big\langle f_0\big|H\big|f_0\big\rangle - a_0\big\langle f_0\big|f_0\big\rangle = 0, \tag{B.3b}$$

using $a_0 = \big\langle f_0\big|H\big|f_0\big\rangle / \big\langle f_0\big|f_0\big\rangle$.

$|f_2\rangle$:

$$|f_2\rangle = H|f_1\rangle - a_1|f_1\rangle - b_1^2|f_0\rangle, \tag{B.4a}$$
$$\langle f_1|f_2\rangle = \langle f_1|H|f_1\rangle - a_1\langle f_1|f_1\rangle - b_1^2\langle f_1|f_0\rangle = 0, \tag{B.4b}$$

using $\langle f_1|f_0\rangle = (\langle f_0|f_1\rangle)^\dagger = 0$ and $a_1 = \langle f_1|H|f_1\rangle/\langle f_1|f_1\rangle$. Also

$$\langle f_0|f_2\rangle = \langle f_0|H|f_1\rangle - a_1\langle f_0|f_1\rangle - b_1^2\langle f_0|f_0\rangle. \tag{B.5}$$

Using $\langle f_0|H = \langle f_1| + a_0\langle f_0|$ gives

$$\langle f_0|f_2\rangle = \langle f_1|f_1\rangle + a_0\langle f_0|f_1\rangle - b_1^2\langle f_0|f_0\rangle = 0 \tag{B.6}$$

using $b_1^2 = \langle f_1|f_1\rangle/\langle f_0|f_0\rangle$.

$|f_3\rangle$:

$$|f_3\rangle = H|f_2\rangle - a_2|f_2\rangle - b_2^2|f_1\rangle, \tag{B.7a}$$
$$\langle f_2|f_3\rangle = \langle f_2|H|f_2\rangle - a_2\langle f_2|f_2\rangle - b_2^2\langle f_2|f_1\rangle = 0, \tag{B.7b}$$

using the orthogonality of $|f_2\rangle$ and $|f_1\rangle$.

$$\begin{aligned}\langle f_1|f_3\rangle &= \langle f_1|H|f_2\rangle - a_2\langle f_1|f_2\rangle - b_2^2\langle f_1|f_1\rangle \\ &= \langle f_2|f_2\rangle + a_1\langle f_1|f_2\rangle + b_1^2\langle f_0|f_2\rangle - b_2^2\langle f_1|f_1\rangle \\ &= 0,\end{aligned} \tag{B.8}$$

using previous results and $b_2^2 = \langle f_2|f_2\rangle/\langle f_1|f_1\rangle$.

$$\begin{aligned}\langle f_0|f_3\rangle &= \langle f_0|H|f_2\rangle - a_2\langle f_0|f_2\rangle - b_2^2\langle f_0|f_1\rangle \\ &= \langle f_1|f_2\rangle + a_0\langle f_0|f_2\rangle = 0,\end{aligned} \tag{B.9}$$

using $\langle f_0|H = \langle f_1| + a_0\langle f_0|$ and previous results.

Thus the first few Lanczos vectors are orthogonal. Next we consider orthogonality of Lanczos state $n+1$ for $n \geq 3$,

$$|f_{n+1}\rangle = H|f_n\rangle - a_n|f_n\rangle - b_n^2|f_{n-1}\rangle, \tag{B.10a}$$
$$\begin{aligned}\langle f_n|f_{n+1}\rangle &= \langle f_n|H|f_n\rangle - a_n\langle f_n|f_n\rangle - b_n^2\langle f_n|f_{n-1}\rangle \\ &= -b_n^2(\langle f_{n-1}|f_n\rangle)^\dagger.\end{aligned} \tag{B.10b}$$

Hence orthogonality of state $n+1$ with state n depends on the orthogonality of state n with state $n-1$. Since n is arbitrarily chosen orthogonality of state n with state $n-1$ depends of orthogonality of state $n-1$ with state $n-2$ and so on.

Thus since the first few Lanczos basis states are orthogonal we have shown that the full Lanczos basis satisfies,

$$\langle f_m|f_n\rangle = 0, \quad m = n \pm 1. \tag{B.11}$$

Similarly we consider

$$\begin{aligned}\langle f_{n-1}|f_{n+1}\rangle &= \langle f_{n-1}|H|f_n\rangle - a_n\langle f_{n-1}|f_n\rangle - b_n^2\langle f_{n-1}|f_{n-1}\rangle \\ &= \langle f_n|f_n\rangle + a_{n-1}\langle f_{n-1}|f_n\rangle + b_{n-1}^2\langle f_{n-2}|f_n\rangle - \langle f_n|f_n\rangle \\ &= b_{n-1}^2\langle f_{n-2}|f_n\rangle, \end{aligned} \tag{B.12}$$

since above we showed that $\langle f_{n-1}|f_n\rangle = 0$. Hence orthogonality of state $n-1$ with state $n+1$ depends on orthogonality of state $n-2$ with state n. Considering $\langle f_{n-2}|f_n\rangle$ we find that it depends on $\langle f_{n-3}|f_{n-1}\rangle$ etc. and hence since the first Lanczos vectors satisfy this relation we have shown that

$$\langle f_m|f_n\rangle = 0, \quad m = n \pm 2. \tag{B.13}$$

Continuing this scheme we may show that

$$\langle f_m|f_n\rangle = 0, \quad m = n \pm 3, \tag{B.14a}$$
$$\langle f_m|f_n\rangle = 0, \quad m = n \pm 4, \tag{B.14b}$$
$$\vdots$$

and hence all in all,

$$\langle f_m|f_n\rangle = \langle f_n|f_n\rangle\delta_{m,n}. \tag{B.15}$$

Appendix C

Anticommutation and matrices

In this appendix we demonstrate in detail the properties of the fermionic sign operator P and (anti)commutation rules for fermionic operators and bosonic operators in the context of matrix representations. For further details regarding matrix P we refer to [26]. To be specific we use the Hubbard chain as example.

C.1 Matrices

We use two fermionic and a bosonic operator as examples and use a site basis defined by $|0\rangle$, $|\uparrow\rangle \equiv c_\uparrow^\dagger |0\rangle$, $|\downarrow\rangle \equiv c_\downarrow^\dagger |0\rangle$ and $|\uparrow\downarrow\rangle \equiv c_\uparrow^\dagger c_\downarrow^\dagger |0\rangle$. In this basis we find the matrix representations

$$c_\uparrow = \begin{pmatrix} 0 & 1 & 0 & 0 \\ 0 & 0 & 0 & 0 \\ 0 & 0 & 0 & 1 \\ 0 & 0 & 0 & 0 \end{pmatrix}, \tag{C.1a}$$

$$c_\downarrow = \begin{pmatrix} 0 & 0 & 1 & 0 \\ 0 & 0 & 0 & -1 \\ 0 & 0 & 0 & 0 \\ 0 & 0 & 0 & 0 \end{pmatrix}, \tag{C.1b}$$

$$N = \begin{pmatrix} 0 & 0 & 0 & 0 \\ 0 & 1 & 0 & 0 \\ 0 & 0 & 1 & 0 \\ 0 & 0 & 0 & 2 \end{pmatrix}, \tag{C.1c}$$

while the matrix representation of the fermionic sign operator is

$$P = \begin{pmatrix} 1 & 0 & 0 & 0 \\ 0 & -1 & 0 & 0 \\ 0 & 0 & -1 & 0 \\ 0 & 0 & 0 & 1 \end{pmatrix}. \tag{C.2}$$

C.2 Anticommutators

First it should be noted that the site operators themselves, (C.1a) and (C.1b), satisfy the correct anticommutation relations, $c_\sigma c^\dagger_{\tilde{\sigma}} + c^\dagger_{\tilde{\sigma}} c_\sigma = \delta_{\sigma,\tilde{\sigma}}$. Here we show how to maintain these relations when expanding the basis to several sites.

First we expand the basis of operators $c_{1\sigma}$ and $c_{2\sigma}$ to the basis of both sites,

$$\tilde{c}_{1\sigma} = c_{1\sigma} \otimes \delta_2, \tag{C.3a}$$
$$\tilde{c}_{2\sigma} = P_1 \otimes c_{2\sigma}, \tag{C.3b}$$

or more specifically

$$\begin{aligned} \tilde{c}_{1\uparrow} &= c_{1\uparrow} \otimes \delta_2 \\ &= \begin{pmatrix} 0 & \delta_2 & 0 & 0 \\ 0 & 0 & 0 & 0 \\ 0 & 0 & 0 & \delta_2 \\ 0 & 0 & 0 & 0 \end{pmatrix}, \end{aligned} \tag{C.4}$$

and

$$\begin{aligned} \tilde{c}_{2\uparrow} &= P_1 \otimes c_{2\uparrow} \\ &= \begin{pmatrix} c_{2\uparrow} & 0 & 0 & 0 \\ 0 & -c_{2\uparrow} & 0 & 0 \\ 0 & 0 & -c_{2\uparrow} & 0 \\ 0 & 0 & 0 & c_{2\uparrow} \end{pmatrix}. \end{aligned} \tag{C.5}$$

We use a compact notation in which entries of matrices can themselves be matrices, and thus Eq. (C.4) and (C.5) are 16×16 matrices. Ordinary

matrix multiplication yields

$$\begin{aligned}\tilde{c}_{1\uparrow}\tilde{c}^{\dagger}_{2\uparrow}+\tilde{c}^{\dagger}_{2\uparrow}\tilde{c}_{1\uparrow} &= \begin{pmatrix}0&\delta_2&0&0\\0&0&0&0\\0&0&0&\delta_2\\0&0&0&0\end{pmatrix}\begin{pmatrix}c^{\dagger}_{2\uparrow}&0&0&0\\0&-c^{\dagger}_{2\uparrow}&0&0\\0&0&-c^{\dagger}_{2\uparrow}&0\\0&0&0&c^{\dagger}_{2\uparrow}\end{pmatrix}\\ &\quad+\begin{pmatrix}c^{\dagger}_{2\uparrow}&0&0&0\\0&-c^{\dagger}_{2\uparrow}&0&0\\0&0&-c^{\dagger}_{2\uparrow}&0\\0&0&0&c^{\dagger}_{2\uparrow}\end{pmatrix}\begin{pmatrix}0&\delta_2&0&0\\0&0&0&0\\0&0&0&\delta_2\\0&0&0&0\end{pmatrix}\\ &= \begin{pmatrix}0&[c^{\dagger}_{2,\uparrow},\delta_2]&0&0\\0&0&0&0\\0&0&0&-[c^{\dagger}_{2,\uparrow},\delta_2]\\0&0&0&0\end{pmatrix},\end{aligned} \tag{C.6}$$

where

$$\begin{aligned}[c^{\dagger}_{2,\uparrow},\delta_2] &= \begin{pmatrix}0&0&0&0\\1&0&0&0\\0&0&0&0\\0&0&1&0\end{pmatrix}\begin{pmatrix}1&0&0&0\\0&1&0&0\\0&0&1&0\\0&0&0&1\end{pmatrix}-\begin{pmatrix}1&0&0&0\\0&1&0&0\\0&0&1&0\\0&0&0&1\end{pmatrix}\begin{pmatrix}0&0&0&0\\1&0&0&0\\0&0&0&0\\0&0&1&0\end{pmatrix}\\ &= \begin{pmatrix}0&0&0&0\\0&0&0&0\\0&0&0&0\\0&0&0&0\end{pmatrix}.\end{aligned} \tag{C.7}$$

Thus indeed we find $\tilde{c}_{1\uparrow}\tilde{c}^{\dagger}_{2\uparrow}+\tilde{c}^{\dagger}_{2\uparrow}\tilde{c}_{1\uparrow}=0$. Had we used δ_1 instead of P_1 this would not have been the case.

Similarly we may consider

$$\begin{aligned}\tilde{c}_{2\uparrow}\tilde{c}^{\dagger}_{2\uparrow}+\tilde{c}^{\dagger}_{2\uparrow}\tilde{c}_{2\uparrow} &= \begin{pmatrix}c_{2\uparrow}&0&0&0\\0&-c_{2\uparrow}&0&0\\0&0&-c_{2\uparrow}&0\\0&0&0&c_{2\uparrow}\end{pmatrix}\begin{pmatrix}c^{\dagger}_{2\uparrow}&0&0&0\\0&-c^{\dagger}_{2\uparrow}&0&0\\0&0&-c^{\dagger}_{2\uparrow}&0\\0&0&0&c^{\dagger}_{2\uparrow}\end{pmatrix}\\ &\quad+\begin{pmatrix}c^{\dagger}_{2\uparrow}&0&0&0\\0&-c^{\dagger}_{2\uparrow}&0&0\\0&0&-c^{\dagger}_{2\uparrow}&0\\0&0&0&c^{\dagger}_{2\uparrow}\end{pmatrix}\begin{pmatrix}c_{2\uparrow}&0&0&0\\0&-c_{2\uparrow}&0&0\\0&0&-c_{2\uparrow}&0\\0&0&0&c_{2\uparrow}\end{pmatrix}\\ &= \begin{pmatrix}\{c^{\dagger}_{2\uparrow},c_{2\uparrow}\}&0&0&0\\0&\{c^{\dagger}_{2\uparrow},c_{2\uparrow}\}&0&0\\0&0&\{c^{\dagger}_{2\uparrow},c_{2\uparrow}\}&0\\0&0&0&\{c^{\dagger}_{2\uparrow},c_{2\uparrow}\}\end{pmatrix},\end{aligned} \tag{C.8}$$

where

$$\{c_{2\uparrow}^\dagger, c_{2\uparrow}\} = \begin{pmatrix} 0 & 1 & 0 & 0 \\ 0 & 0 & 0 & 0 \\ 0 & 0 & 0 & 1 \\ 0 & 0 & 0 & 0 \end{pmatrix} \begin{pmatrix} 0 & 0 & 0 & 0 \\ 1 & 0 & 0 & 0 \\ 0 & 0 & 0 & 0 \\ 0 & 0 & 1 & 0 \end{pmatrix} + \begin{pmatrix} 0 & 0 & 0 & 0 \\ 1 & 0 & 0 & 0 \\ 0 & 0 & 0 & 0 \\ 0 & 0 & 1 & 0 \end{pmatrix} \begin{pmatrix} 0 & 1 & 0 & 0 \\ 0 & 0 & 0 & 0 \\ 0 & 0 & 0 & 1 \\ 0 & 0 & 0 & 0 \end{pmatrix}$$
$$= \begin{pmatrix} 1 & 0 & 0 & 0 \\ 0 & 1 & 0 & 0 \\ 0 & 0 & 1 & 0 \\ 0 & 0 & 0 & 1 \end{pmatrix}, \tag{C.9}$$

and hence indeed $\{\tilde{c}_{2\uparrow}, \tilde{c}_{2\uparrow}^\dagger\} = 1$. Perhaps it should be pointed out that this property would be maintained even if one had used δ_1 instead of the correct P_1.

It should be noted that the fermionic sign matrix for sites 1 and 2 is

$$P_{12} = P_1 \otimes P_2$$
$$= \begin{pmatrix} P_2 & 0 & 0 & 0 \\ 0 & -P_2 & 0 & 0 \\ 0 & 0 & -P_2 & 0 \\ 0 & 0 & 0 & P_2 \end{pmatrix}, \tag{C.10}$$

where it is clear that an odd total number of particles on sites 1 and 2 gives a sign, while an even total number of particles does not.

C.3 Commutators

The number operator (C.1c) is diagonal – and remains diagonal after enlargement of the basis. Diagonal matrices commute – and hence so does the number operators before and after enlarging the basis. Hence any commutation relations of diagonal matrices are preserved in the proces of enlarging the basis. Note that we use δ and not P when enlarging the Hilbert space for bosonic operators.

Appendix D

Truncation of a continued fraction

To explore what kind of convergence we can expect for the DMRG calculation of the spectral function in Sect. 4.5.2 we consider the selfenergy used in Sect. 4.7. For the selfenergy we have both an exact result and a continued fraction we can truncate and hence we can compare the two. Writing explicitly $\omega + i\eta$ we have

$$\begin{aligned} \Sigma^R(\omega) &\equiv V^2 G^R(\omega), \\ G^R(\omega) &= \frac{1}{\omega + i\eta - \epsilon - \frac{t^2}{\omega + i\eta - \epsilon - \cdots}} \\ &= \frac{(\omega + i\eta - \epsilon) - \mathrm{sign}(\omega - \epsilon)\sqrt{(\omega + i\eta - \epsilon)^2 - 4t^2}}{2t^2}. \end{aligned} \tag{D.1}$$

Truncating the continued fraction and comparing to the exact result leads to Fig. D.1. The value of η is chosen fairly large, $\eta = 0.01$ to broaden the δ-peaks.

The structure of the Lanczos method is similar to the continued fraction and hence we expect this kind of convergence when calculating $\langle c_i c_i^\dagger \rangle$ and $\langle c_i^\dagger c_i \rangle$ for increased number of Lanczos coefficients a_i and b_i^2.

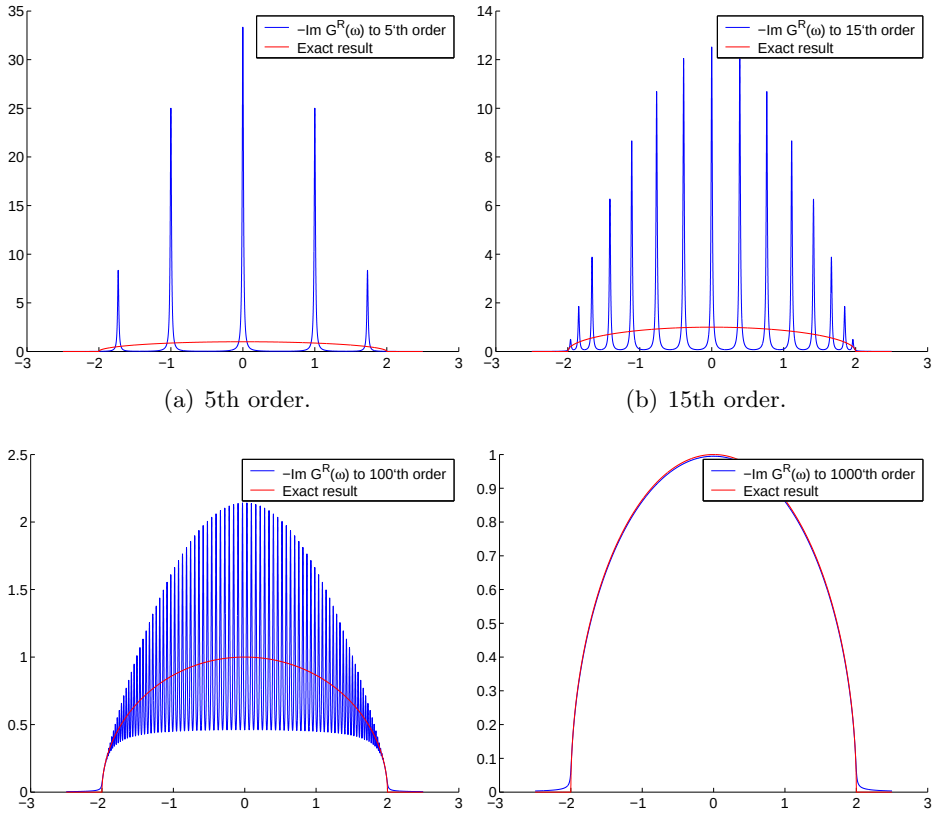

(a) 5th order.

(b) 15th order.

(c) 100th order.

(d) 1000th order.

Figure D.1: Imaginary part of $-G^R(\omega)$ for $\epsilon = 0$ and $\eta = 0.01$.

Appendix E

Equation Of Motion Technique

Here we derive the Equations Of Motion (EOM) for the dot and lead Green's functions in the two cases relevant for this thesis. In this appendix a convergence factor $\omega \to \omega + i\eta$ is understood, but not explicitly written, n retarded Green's functions .

E.1 Quantum dot with single infinite lead

The Hamiltonian for this setup is

$$H = H_D + H_L + H_{DL}, \tag{E.1a}$$

$$H_D = \sum_{i=a}^{b} (\epsilon_i - V_g)\, a_i^\dagger a_i \equiv \sum_{i=a}^{b} \varepsilon_i a_i^\dagger a_i, \tag{E.1b}$$

$$H_L = -t \sum_{j=1}^{\infty} \left(c_j^\dagger c_{j+1} + c_{j+1}^\dagger c_j \right) + \varepsilon \sum_{j=1}^{\infty} c_j^\dagger c_j, \tag{E.1c}$$

$$H_{DL} = \sum_{i=a}^{b} V_i \left(a_i^\dagger c_1 + c_1^\dagger a_i \right). \tag{E.1d}$$

In order not to clutter up the notation we denote by a and b the dot levels and by $1, 2, \cdots$ the lead sites.

The Green's function for the dot levels is generally defined as

$$G_{ij}^R(t-t') = -i\theta(t-t') \left\langle \left\{ a_i(t), a_j^\dagger(t') \right\} \right\rangle. \tag{E.2}$$

We seek the EOM for $G_{ij}^R(t-t')$, and consider

$$\begin{aligned} i\partial_t G_{ij}^R(t-t') &= \delta(t-t') \left\langle \left\{ a_i(t), a_j^\dagger(t) \right\} \right\rangle + \theta(t-t') \left\langle \left\{ \partial_t a_i(t), a_j^\dagger(t') \right\} \right\rangle \\ &= \delta(t-t')\delta_{ij} + \theta(t-t') \left\langle \left\{ \partial_t a_i(t), a_j^\dagger(t') \right\} \right\rangle. \end{aligned} \tag{E.3}$$

The time derivative of an operator in the Schrödinger picture is

$$\begin{aligned}\partial_t a_i(t) &= \partial_t \left(e^{iHt} a_i e^{-iHt}\right) \\ &= e^{iHt}\left(iHa_i - ia_iH + \partial_t a_i\right) e^{-iHt} \\ &= i\left[H, a_i\right](t), \end{aligned} \tag{E.4}$$

where we used that a_i has no explicit time dependence, and where H is the full Hamiltonian of the system. Hence we find

$$\begin{aligned}[H, a_i] &= [H_D, a_i] + [H_{DL}, a_i], \\ [H_D, a_i] &= \sum_j \varepsilon_j \left[a_j^\dagger a_j, a_i\right] \\ &= \sum_j \varepsilon_j \left(a_j^\dagger \{a_j, a_i\} - \{a_j^\dagger, a_i\} a_j\right) \\ &= -\varepsilon_i a_i, \end{aligned} \tag{E.5a}$$

$$\begin{aligned}[H_{DL}, a_i] &= \sum_j V_j \left[a_j^\dagger c_1 + c_1^\dagger a_j, a_i\right] \\ &= \sum_j V_j \left(a_j^\dagger \{c_1, a_i\} - \{a_j^\dagger, a_i\} c_1 + c_1^\dagger \{a_j, a_i\} - \{c_1^\dagger, a_i\} a_j\right) \\ &= -V_i c_1. \end{aligned} \tag{E.5b}$$

Thus the EOM for $G_{ij}^R(t-t')$ becomes

$$\begin{aligned} i\partial_t G_{ij}^R(t-t') &= \delta(t-t')\delta_{ij} - \varepsilon_i i\theta(t-t')\left\langle\left\{a_i(t), a_j^\dagger(t')\right\}\right\rangle \\ &\quad - V_i i\theta(t-t')\left\langle\left\{c_1(t), a_j^\dagger(t')\right\}\right\rangle \\ &\equiv \delta(t-t')\delta_{ij} + \varepsilon_i G_{ij}^R(t-t') + V_i G_{1j}^R(t-t'), \end{aligned} \tag{E.6}$$

where the hybrid Green's function G_{1j}^R was defined.

Fourier transformation thus yields,

$$\begin{aligned} &(i\partial_t - \varepsilon_i) \int_{-\infty}^{\infty} \frac{d\omega}{2\pi} G_{ij}^R(\omega) e^{-i\omega(t-t')} = \\ &\qquad \delta(t-t')\delta_{ij} + V_i \int_{-\infty}^{\infty} \frac{d\omega}{2\pi} G_{ij}^R(\omega) e^{-i\omega(t-t')} \Leftrightarrow \\ &\int_{-\infty}^{\infty} \frac{d\omega}{2\pi} (\omega - \varepsilon_i) G_{ij}^R(\omega) e^{-i\omega(t-t')} = \\ &\qquad \int_{-\infty}^{\infty} \frac{d\omega}{2\pi} (\delta_{ij} + V G_{ij}^R(\omega)) e^{-i\omega(t-t')}, \end{aligned} \tag{E.7}$$

so that in fourier space we find the EOM

$$(\omega - \varepsilon_i) G_{ij}^R(\omega) = \delta_{ij} + V_i G_{1j}^R(\omega). \tag{E.8}$$

We also need the EOM for G^R_{1j}, found similarly,

$$\begin{aligned} i\partial_t G^R_{1j}(t-t') &= \delta(t-t')\langle\{c_1(t), a_j^\dagger(t)\}\rangle + \theta(t-t')\langle\{\partial_t c_1(t), a_j^\dagger(t')\}\rangle \\ &= \theta(t-t')\langle\{\partial_t c_1(t), a_j^\dagger(t')\}\rangle. \end{aligned} \tag{E.9}$$

The time derivative of $c_1(t)$ is,

$$\begin{aligned} [H, c_1] &= [H_L, c_1] + [H_{DL}, c_1]\,, \\ [H_L, c_1] &= \varepsilon \sum_j \left[c_j^\dagger c_j, c_1\right] - t\sum_j \left[c_j^\dagger c_{j+1} + c_{j+1}^\dagger c_j, c_1\right] \\ &= \varepsilon \sum_j \left(c_j^\dagger\{c_j, c_1\} - \{c_j^\dagger, c_1\}c_j\right) \\ &\quad -t\sum \left(c_j^\dagger\{c_{j+1}, c_1\} - \{c_j^\dagger, c_1\}c_{j+1} + c_{j+1}^\dagger\{c_j, c_1\} - \{c_{j+1}^\dagger, c_1\}c_j\right) \\ &= -\varepsilon c_1 + t c_2, \end{aligned} \tag{E.10a}$$

$$\begin{aligned} [H_{DL}, c_1] &= \sum_j V_j \left[a_j^\dagger c_1 + c_1^\dagger a_j, c_1\right] \\ &= \sum_j V_j \left(a_j^\dagger\{c_1, c_1\} - \{a_j^\dagger, c_1\}c_1 + c_1^\dagger\{a_j, c_1\} - \{c_1^\dagger, c_1\}a_j\right) \\ &= -\sum_j V_j a_j, \end{aligned} \tag{E.10b}$$

and hence

$$\begin{aligned} i\partial_t G^R_{1j}(t-t') &= -\varepsilon i\theta(t-t')\langle\{c_1(t), a_j^\dagger(t')\}\rangle \\ &\quad -t\left(-i\theta(t-t')\langle\{c_2(t), a_j^\dagger(t')\}\rangle\right) \\ &\quad -\sum_i V_i i\theta(t-t')\langle\{a_i(t), a_j^\dagger(t')\}\rangle. \end{aligned} \tag{E.11}$$

Fourier transforming we find

$$(\omega - \varepsilon)G^R_{1j}(\omega) = -tG^R_{2j}(\omega) + \sum_i V_i G^R_{ij}(\omega). \tag{E.12}$$

Yet another hybrid Green's function has been introduced, and trying to find the EOM for G^R_{2j} introduces yet another hybrid Green's function and the equations never close.

All these EOMs can be understood by the following simple argument, taking e.g. G^R_{1j} as an example: From the first site in the lead there are limited number of possibilities of propagating. You can either stay, giving a term ε, or jump to the dot, via couplings V_i, or jump to the second site in the lead via coupling $-t$, hence the EOM in Eq. (E.12).

Solution

We specialize to the case $ij = aa$, and consider solutions to increasing order of hybrid Green's functions.

Finite order

0th order: With $G^R_{1a} = 0$ we find from Eq. (E.8)

$$G^R_{aa} = \frac{1}{\omega - \varepsilon_a} = g^R_a, \tag{E.13}$$

which is the well known free result.

1st order: Here $G^R_{2a} = 0$ and hence we find from Eq. (E.8) and (E.12)

$$\begin{aligned} G^R_{1a} &= \frac{V_a}{\omega - \varepsilon} G^R_{aa} + \frac{V_b}{\omega - \varepsilon} G^R_{ba} \Rightarrow \\ G^R_{aa} &= \frac{1}{\omega - \varepsilon_a - \frac{V_a^2}{\omega - \varepsilon}} + \frac{\frac{V_a V_b}{\omega - \varepsilon}}{\omega - \varepsilon_a - \frac{V_a^2}{\omega - \varepsilon}} G^R_{ba}. \end{aligned} \tag{E.14}$$

To this order we may define selfenergies

$$\Sigma^R_{1,aa} = \frac{V_a^2}{\omega - \varepsilon}, \tag{E.15a}$$

$$\Sigma^R_{1,ab} = \frac{V_a V_b}{\omega - \varepsilon}. \tag{E.15b}$$

2nd order: Here $G^R_{3a} = 0$,

$$\begin{aligned} G^R_{2a} &= \frac{-t}{\omega - \varepsilon} G^R_{1a} \Rightarrow \\ G^R_{1a} &= \frac{V_a}{\omega - \varepsilon - \frac{t^2}{\omega - \varepsilon}} G^R_{aa} + \frac{V_b}{\omega - \varepsilon - \frac{t^2}{\omega - \varepsilon}} G^R_{ba} \Rightarrow \\ G^R_{aa} &= \frac{1}{\omega - \varepsilon_a - \frac{V_a^2}{\omega - \varepsilon - \frac{t^2}{\omega - \varepsilon}}} + \frac{\frac{V_a V_b}{\omega - \varepsilon - \frac{t^2}{\omega - \varepsilon}}}{\omega - \varepsilon_a - \frac{V_a^2}{\omega - \varepsilon - \frac{t^2}{\omega - \varepsilon}}} G^R_{ba}, \end{aligned} \tag{E.16}$$

and again we may define selfenergies,

$$\Sigma^R_{2,aa} = \frac{V_a^2}{\omega - \varepsilon - \frac{t^2}{\omega - \varepsilon}}, \tag{E.17a}$$

$$\Sigma^R_{2,ab} = \frac{V_a V_b}{\omega - \varepsilon - \frac{t^2}{\omega - \varepsilon}}. \tag{E.17b}$$

Infinite order

It is easy to see that to infinite order we find

$$G^R_{aa} = \frac{1}{\omega - \varepsilon_a - \frac{V_a^2}{\omega-\varepsilon-\frac{t^2}{\omega-\varepsilon-\cdots}}} + \frac{\frac{V_aV_b}{\omega-\varepsilon-\frac{t^2}{\omega-\varepsilon-\cdots}}}{\omega - \varepsilon_a - \frac{V_a^2}{\omega-\varepsilon-\frac{t^2}{\omega-\varepsilon-\cdots}}} G^R_{ba}, \quad \text{(E.18)}$$

and hence selfenergies

$$\Sigma^R_{\infty,aa} = \frac{V_a^2}{\omega - \varepsilon - \frac{t^2}{\omega-\varepsilon-\cdots}}, \quad \text{(E.19a)}$$

$$\Sigma^R_{\infty,ab} = \frac{V_aV_b}{\omega - \varepsilon - \frac{t^2}{\omega-\varepsilon-\cdots}}. \quad \text{(E.19b)}$$

Defining the selfenergy and the Green's function for the first site in the lead in absence of the quantum dot,

$$\Sigma^R \equiv V^2\tilde{G}^R_{11}, \quad \text{(E.20a)}$$

$$\tilde{G}^R_{11} = \frac{1}{\omega - \varepsilon - \frac{t^2}{\omega-\varepsilon-\cdots}}, \quad \text{(E.20b)}$$

we can restate Eq. (E.18) like

$$G^R_{aa} = \frac{1}{\omega - \varepsilon_a - \Sigma^R_{aa}} + \frac{\Sigma^R_{ab}}{\omega - \varepsilon_a - \Sigma^R_{aa}} G^R_{ba}. \quad \text{(E.21)}$$

In order to solve for G^R_{aa} we need to find G^R_{ba}. This is done similarly to G^R_{aa},

$$G^R_{ba} = \frac{\Sigma^R_{ba}}{\omega - \varepsilon_b - \Sigma^R_{bb}} G^R_{aa}, \quad \text{(E.22)}$$

and hence the final solution is

$$G^R_{aa}(\omega) = \frac{1}{\omega - \varepsilon_a - \Sigma^R_{aa}(\omega) - \frac{\Sigma^R_{ab}(\omega)\Sigma^R_{ba}(\omega)}{\omega-\varepsilon_b-\Sigma^R_{bb}(\omega)}}. \quad \text{(E.23)}$$

The solution for G^R_{bb} is found analogously,

$$G^R_{bb}(\omega) = \frac{1}{\omega - \varepsilon_b - \Sigma^R_{bb}(\omega) - \frac{\Sigma^R_{ba}(\omega)\Sigma^R_{ab}(\omega)}{\omega-\varepsilon_a-\Sigma^R_{aa}(\omega)}}. \quad \text{(E.24)}$$

Finally using the selfsimilarity of $\tilde{G}^R_{11}$ we find the closed formal solution,

$$\begin{aligned}
\tilde{G}^R_{11} &= \frac{1}{\omega - \varepsilon - t^2\tilde{G}^R_{11}} \\
&= \frac{1}{(g^R)^{-1} - t^2\tilde{G}^R_{11}} \Rightarrow \\
t^2 g^R(\tilde{G}^R_{11})^2 - \tilde{G}^R_{11} + g^R &= 0 \Rightarrow \\
\tilde{G}^R_{11} &= \frac{1 \pm \sqrt{1 - 4t^2(g^R)^2}}{2t^2 g^R} \\
&= \frac{(g^R)^{-1} \pm (g^R)^{-1}\sqrt{1 - 4t^2(g^R)^2}}{2t^2},
\end{aligned} \tag{E.25}$$

where the free Green's function $g^R = 1/(\omega - \epsilon)$ was introduced. In the limit of vanishing hopping element, $t \to 0$, we expect to find the free result, and hence using L'Hospitals rule we find

$$\begin{aligned}
\lim_{t\to 0} \frac{1 \pm (g^R)^{-1}\sqrt{1 - 4t^2(g^R)^2}}{2t^2} &\sim \lim_{t\to 0} \mp (g^R)^{-1} \frac{(g^R)^2}{\sqrt{1 - 4t^2(g^R)^2}} \\
&= \mp g^R,
\end{aligned} \tag{E.26}$$

In our case lead energies vanish, $\epsilon = 0$, and hence $(g^R)^{-1} = \omega$. Thus we find the solution,

$$\begin{aligned}
\tilde{G}^R_{11} &= \frac{\omega/2t - \omega/2t\sqrt{1 - 4t^2/\omega^2}}{t} \\
&= \frac{\omega/2t - \mathrm{sign}(\omega)\sqrt{(\omega/2t)^2 - 1}}{t}.
\end{aligned} \tag{E.27}$$

In all the above equations we have ignored the infinitesimal imaginary convergence factor $i\eta$. Putting in by hand $\omega \to \omega + i\eta$ the plot of the real and imaginary part of the Green's function $\tilde{G}^R_{11}$ is shown in Fig. E.1.

It should be noted that the real and imaginary parts of $\tilde{G}^R_{11}(\omega)$ are given by

$$\mathrm{Re}\tilde{G}^R_{11} = \frac{\omega/2t - \theta(|\omega|/2t - 1)\mathrm{sign}(\omega)\sqrt{(\omega/2t)^2 - 1}}{t}, \tag{E.28a}$$

$$\mathrm{Im}\tilde{G}^R_{11} = \frac{-\theta(1 - |\omega|/2t)\sqrt{1 - (\omega/2t)^2}}{t}, \tag{E.28b}$$

where there is *no* hidden $i\eta$.

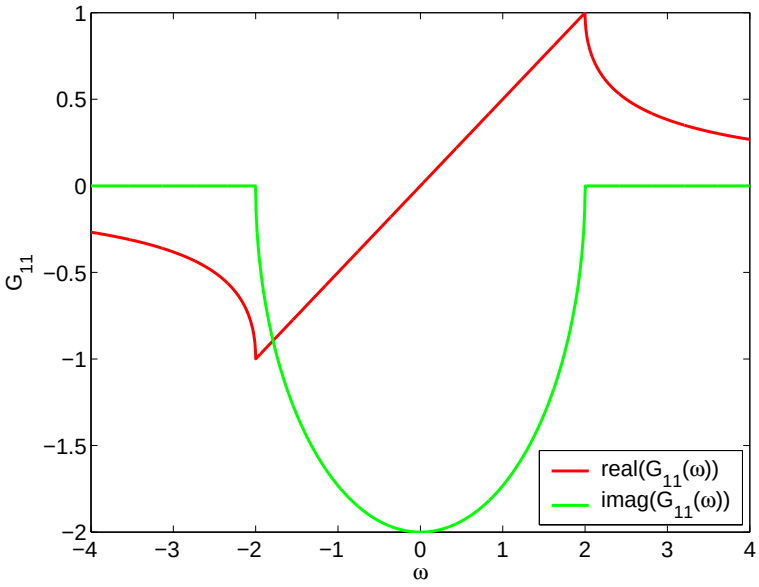

Figure E.1: Plot of real and imaginary part of $\tilde{G}^R_{11}(\omega)$.

E.2 Quantum dot with two infinite leads

Here the Hamiltonian is

$$H = H_{Dot} + H_{Right\ Lead} + H_{Left\ Lead} + H_{DL}, \tag{E.29a}$$

$$H_{Dot} = \sum_{i=a}^{b} (\epsilon_i - V_g) a_i^\dagger a_i \equiv \sum_i \varepsilon_a a_i^\dagger a_i, \tag{E.29b}$$

$$H_{Right\ Lead} = -t \sum_{j=1}^{\infty} (c_j^\dagger c_{j+1} + c_{j+1}^\dagger c_j) + \varepsilon \sum_{j=1}^{\infty} c_j^\dagger c_j, \tag{E.29c}$$

$$H_{Left\ Lead} = -t \sum_{j=-1}^{-\infty} (c_j^\dagger c_{j-1} + c_{j-1}^\dagger c_j) + \varepsilon \sum_{j=-1}^{-\infty} c_j^\dagger c_j, \tag{E.29d}$$

$$H_{DL} = \sum_{i=a}^{b} \left(V_i^R (a_i^\dagger c_1 + c_1^\dagger a_i) + V_i^L (a_i^\dagger c_{-1} + c_{-1}^\dagger a_i) \right), \tag{E.29e}$$

and the Green's functions are defined similarly,

$$G^R_{ij}(t - t') = -i\theta(t - t') \left\langle \left\{ a_i(t), a_j^\dagger(t') \right\} \right\rangle. \tag{E.30}$$

The analysis is essentially the same, only there are more couplings available. The final result resembles the single lead case,

$$G^R_{aa} = \frac{1}{\omega - \varepsilon_a - \Sigma^R_{aa} - \frac{\Sigma^R_{ab}\Sigma^R_{ba}}{\omega - \varepsilon_b - \Sigma^R_{bb}}}, \tag{E.31a}$$

$$G^R_{bb} = \frac{1}{\omega - \varepsilon_b - \Sigma^R_{bb} - \frac{\Sigma^R_{ba}\Sigma^R_{ab}}{\omega - \varepsilon_a - \Sigma^R_{aa}}}, \tag{E.31b}$$

where the selfenergies are

$$\Sigma^R_{ij} = \left(V^R_i V^R_j + V^L_i V^L_j\right) \tilde{G}^R_{11}, \tag{E.32}$$

and where $\tilde{G}^R_{11}$ is given in Eq. (E.27).

We see that the overall structures of the two results are similar. However it is *not* possible to map e.g. the single lead Green's function onto the double lead Green's function by simply redefining coupling constants. This means that the two systems indeed are different, and hence we cannot model the two lead system by modifying the couplings in the single lead system.

Appendix F

Evaluation of n_i for non-interacting biased quantum dot

In this appendix we consider more explicitly the integration of the Green's function $G_{ij}^{<}$ in Chap. 5.

F.1 Analytic expressions

The retarded Green's functions can be written in matrix form,

$$\mathbf{G}^R = \mathbf{g}^R + \mathbf{g}^R\mathbf{\Sigma}^R\mathbf{G}^R, \tag{F.1}$$

where $\mathbf{G}^R$ is the full retarded Green's function, $\mathbf{g}^R$ is the corresponding free Green's function, and $\mathbf{\Sigma}^R$ is the retarded selfenergy. This result enables us to use a result from non-equilibrium Green's function theory,[1]

$$\mathbf{G}^< = \mathbf{G}^R\mathbf{\Sigma}^<\mathbf{G}^A, \tag{F.2}$$

or more explicitly we use

$$G_{aa}^< = G_{aa}^R\Sigma_{aa}^<G_{aa}^A + G_{ab}^R\Sigma_{ba}^<G_{aa}^A + G_{aa}^R\Sigma_{ab}^<G_{ba}^A + G_{ab}^R\Sigma_{bb}^<G_{ba}^A, \tag{F.3a}$$

$$G_{bb}^< = G_{bb}^R\Sigma_{bb}^<G_{bb}^A + G_{ba}^R\Sigma_{ab}^<G_{bb}^A + G_{bb}^R\Sigma_{ba}^<G_{ab}^A + G_{ba}^R\Sigma_{aa}^<G_{ab}^A, \tag{F.3b}$$

where

$$\Sigma_{ij}^< = V_i^RV_j^R\tilde{G}_{11,\mu_R}^< + V_i^LV_j^L\tilde{G}_{11,\mu_L}^<, \tag{F.4a}$$

$$\tilde{G}_{11,\mu_{R/L}}^< = -2in_F^{R/L}(\omega)\mathrm{Im}\tilde{G}_{11}^R, \tag{F.4b}$$

$$n_F^{R/L}(\omega) = \frac{1}{e^{-\beta(\mu_{L/R}-\omega)}+1}. \tag{F.4c}$$

[1] [18], p. 165-166.

Using this result we may compute the occupation on the dot in the standard way

$$\begin{aligned} n_i(V_g) &= -iG^<_{ii}(t=0,V_g) \\ &= \int_{-\infty}^{\infty} \frac{d\omega}{2\pi i} G^<_{ii}(\omega, V_g). \end{aligned} \tag{F.5}$$

F.2 Numerics

In this section we evaluate the different parts entering the expression for the occupation and evaluate the occupation of the dot.

F.2.1 $G^A(\omega, V_g)$

The advanced Green's function is the complex conjugate of the retarded Green's function,

$$G^A(\omega, V_g) = \left(G^R(\omega, V_g)\right)^*, \tag{F.6}$$

and the retarded Green's functions were found explicitly using EOM techniques in App. E. Plots of $\mathrm{Im}G^A(\omega)$ for various couplings and gate voltages are shown in Fig. F.1, F.2, and F.3.

Any properly defined spectral function obey the sum rule

$$A(t) \equiv \left\langle \{c(t), c^\dagger(0)\} \right\rangle, \tag{F.7a}$$

$$\begin{aligned} \int_{-\infty}^{\infty} \frac{d\omega}{2\pi} A(\omega) &= \int_{-\infty}^{\infty} \frac{d\omega}{2\pi} \int_{-\infty}^{\infty} dt e^{i\omega t} A(t) \\ &= \int_{-\infty}^{\infty} dt \delta(t) A(t) \\ &= A(0) = 1. \end{aligned} \tag{F.7b}$$

When considering the figures of $\mathrm{Im}G^A$ there are two things to notice: (i) The scales are very different, and (ii) the integrated weights of these functions are not equal.

This does not contradict the sum rule in Eq. (F.7), since although the imaginary part of the selfenergy vanishes outside the band, there is still the infinitesimal imaginary part $\omega \to \omega - i\eta$ in the advanced Green's function. η is infinitesimal, and the imaginary part of the advanced Green's function is proportional to η outside the band, making $\mathrm{Im}G^A$ *mostly* zero. But if the denominator of G^A vanishes for particular values of ω then $\mathrm{Im}G^A$ has δ-like peaks for those values of ω and hence also integrated weight.

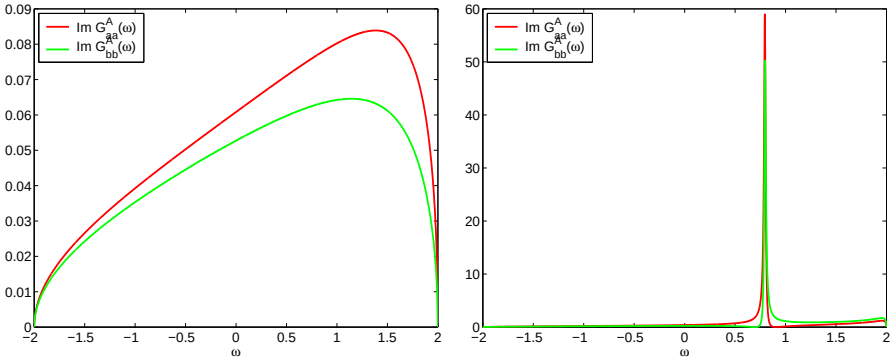

(a) $V_g = -4$. (b) $V_g = -2$.

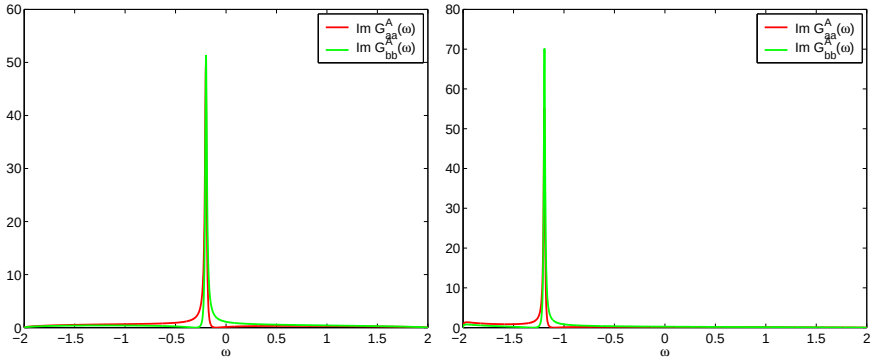

(c) $V_g = -1$. (d) $V_g = 0$.

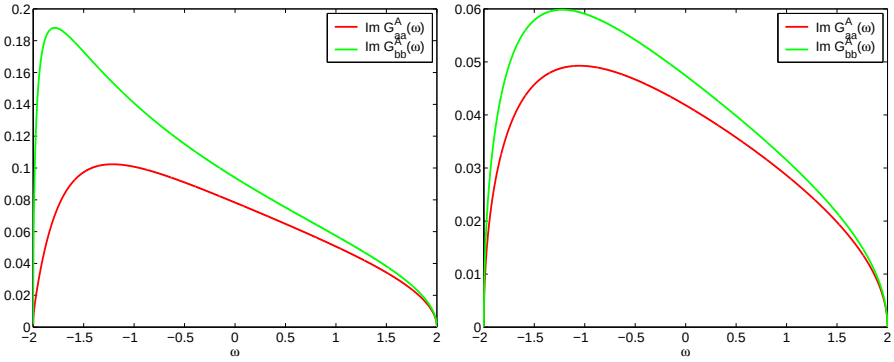

(e) $V_g = 1$. (f) $V_g = 2$.

Figure F.1: Im$G^A(\omega)$ for $V_i^{L/R} = 0.5$. Note the different scales.

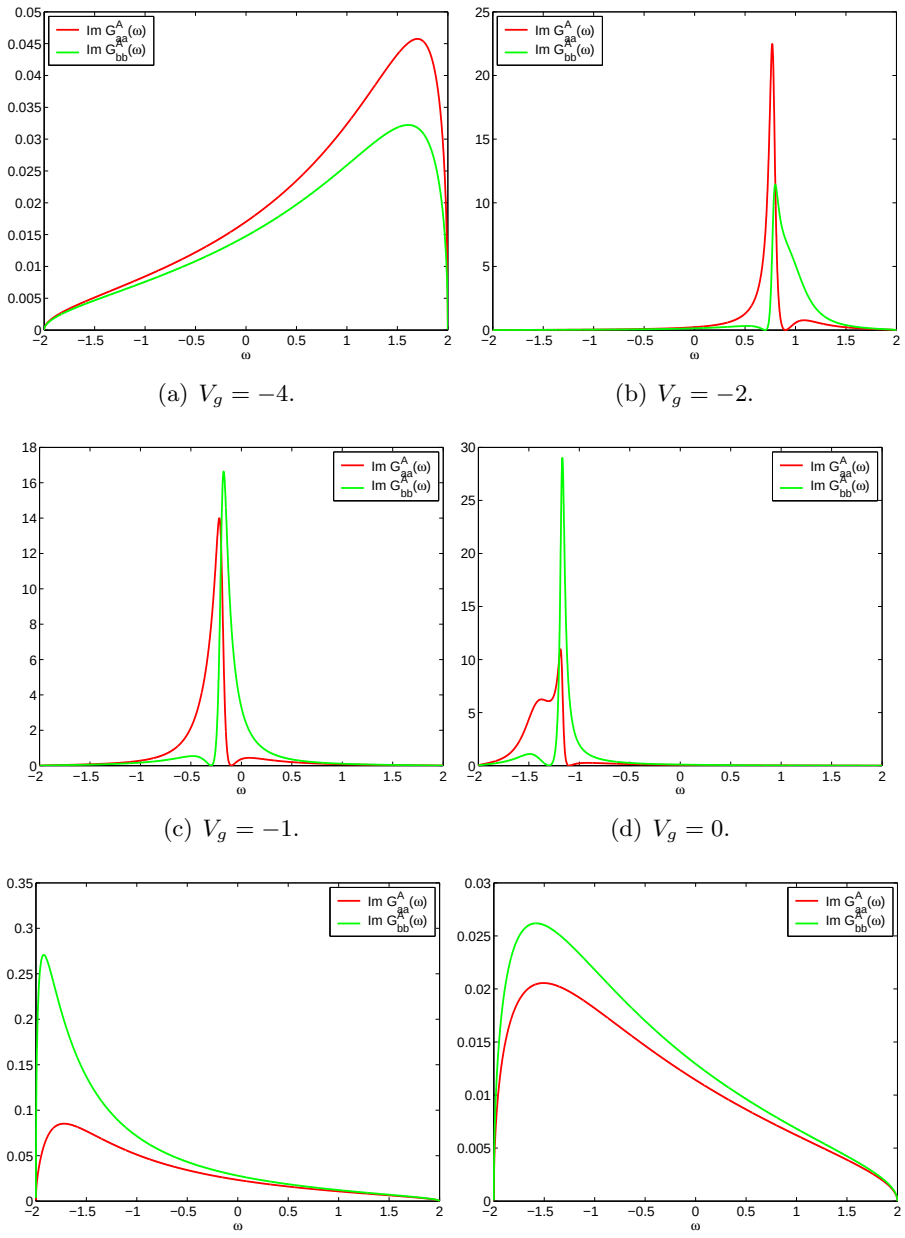

(a) $V_g = -4$. (b) $V_g = -2$.

(c) $V_g = -1$. (d) $V_g = 0$.

(e) $V_g = 1$. (f) $V_g = 2$.

Figure F.2: Im$G^A(\omega)$ for $V_i^{L/R} = 0.25$. Note the different scales.

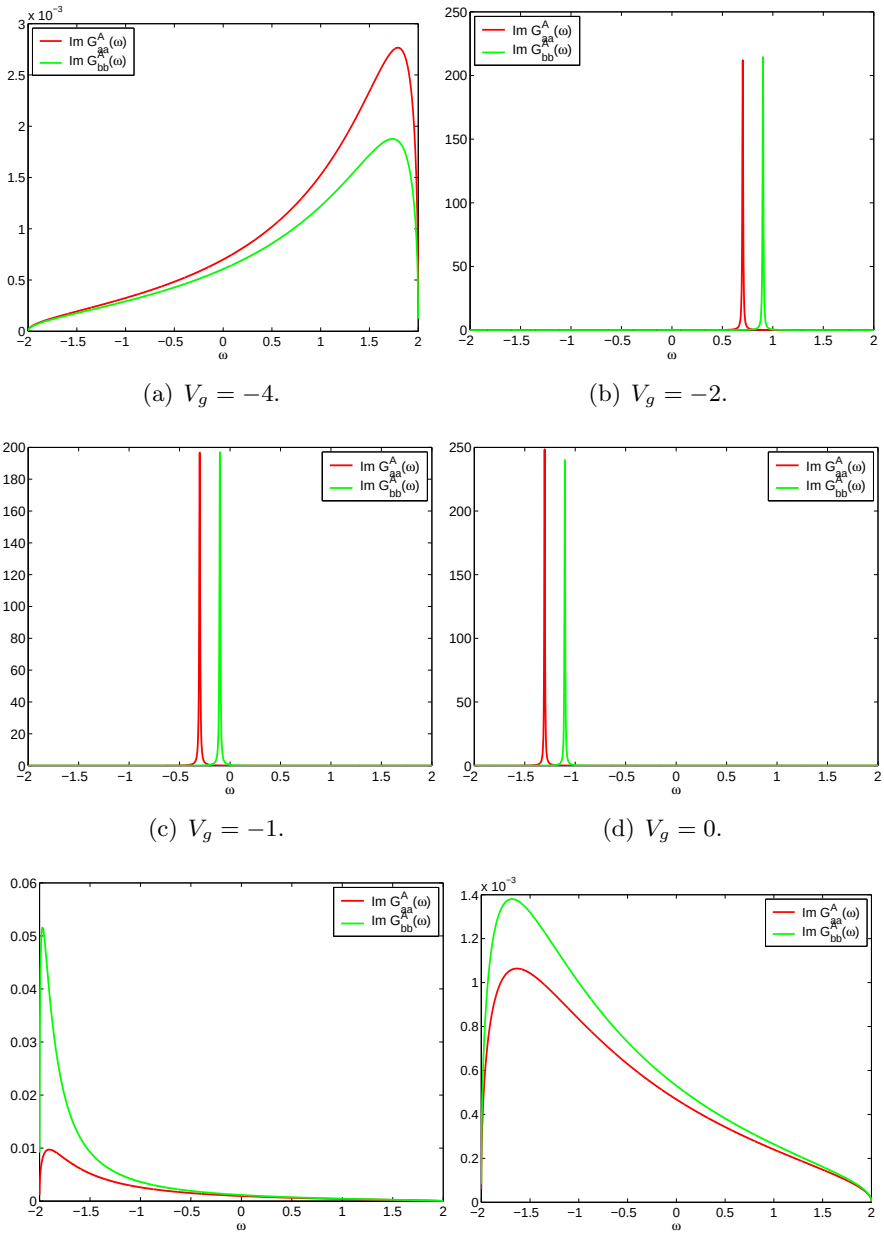

(a) $V_g = -4$. (b) $V_g = -2$.

(c) $V_g = -1$. (d) $V_g = 0$.

(e) $V_g = 1$. (f) $V_g = 2$.

Figure F.3: Im$G^A(\omega)$ for $V_i^{L/R} = 0.05$. Note the different scales.

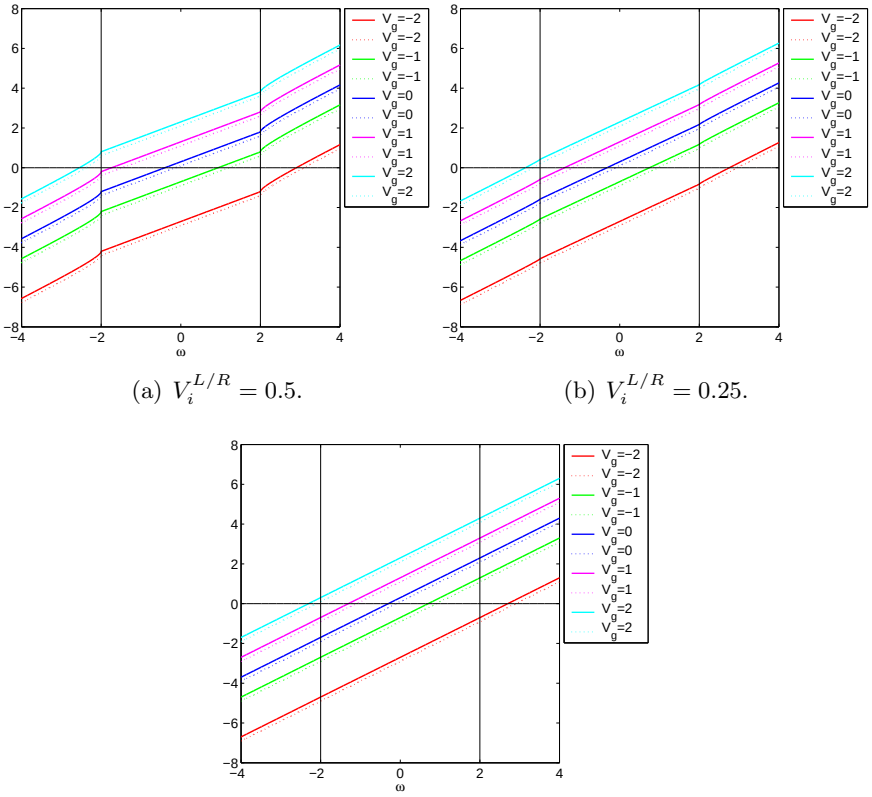

(a) $V_i^{L/R} = 0.5$. (b) $V_i^{L/R} = 0.25$.

(c) $V_i^{L/R} = 0.05$.

Figure F.4: Graphical location of singular points for various couplings. Outside the band a vanishing denominator corresponds to a singular point. Full lines are for G^R_{aa} and dotted lines are for G^R_{bb}.

Singularities

By considering the denominator of G^R or G^A it is possible to find graphically the position of the δ-like peaks outside the band. In general we have

$$\mathrm{Im}\frac{1}{\mathrm{Re}X + i\mathrm{Im}X} \;=\; \frac{-\mathrm{Im}X}{(\mathrm{Re}X)^2 + (\mathrm{Im}X)^2}, \tag{F.8}$$

so that if $\mathrm{Im}X = 0^+$ in some region the singular points are determined by $\mathrm{Re}X = 0$.

In this context this corresponds to

$$0 \;=\; \mathrm{Re}\left(\omega - (\varepsilon_a - V_g) - \Sigma^R_{aa} - \frac{\Sigma^R_{ab}\Sigma^R_{ba}}{\omega - (\varepsilon_b - V_g) - \Sigma^R_{bb}}\right), \tag{F.9}$$

where

$$\Sigma_{ij}^R = (V_i^L V_j^L + V_i^R V_j^R)\tilde{G}_{11}^R, \tag{F.10a}$$

$$\mathrm{Re}\tilde{G}_{11}^R = \frac{\omega/2t - \theta(|\omega|/2t-1)\mathrm{sign}(\omega)\sqrt{(\omega/2t)^2-1}}{t}, \tag{F.10b}$$

$$\mathrm{Im}\tilde{G}_{11}^R = \frac{-\theta(1-|\omega|/2t)\sqrt{1-(\omega/2t)^2}}{t}. \tag{F.10c}$$

Eq. F.9 can easily be solved graphically, to locate the singular points. In Fig. F.4 we have plotted the real part of the denominator of G_{aa}^R and G_{bb}^R for a range of differen gate voltages. It is clearly seen that there are indeed singular points outside the band and hence the spectral function has δ-like peaks at these points.

A comparison with Fig. F.1-F.3 shows that the values of V_g where singular points exist outside the band correspond spectral functions without pronounced δ-like peaks, and where integrated weight is missing.

F.2.2 $G_{ii}^<(\omega, V_g)$

The lesser Green's functions are given explicitly in Eq. (F.3). In Fig. F.5, F.6 and F.7 we show plots of the imaginary part of the lesser Green's functions inside the band for various gate voltages and couplings to the leads.

F.2.3 $n_i(V_g)$

Integrating $G_{ii}^<(\omega, V_g)/2\pi i$ over $\omega \in [-\infty, \infty]$, and using a fine grid of gate voltages gives $n_i(V_g)$. In practice we use integration over a finite interval, where it is essential to include the singular points discussed above. Plots of analytical as well as DMRG occupations are shown in Fig. F.8.

It should be noted that numeric errors might be present in the occupations due to the δ-like peaks in the spectral function discussed above. Such peaks are very difficult to integrate numerically, which possibly introduces numerical errors in the occupations presented here. A more careful analytic study should be performed to eliminate these errors.

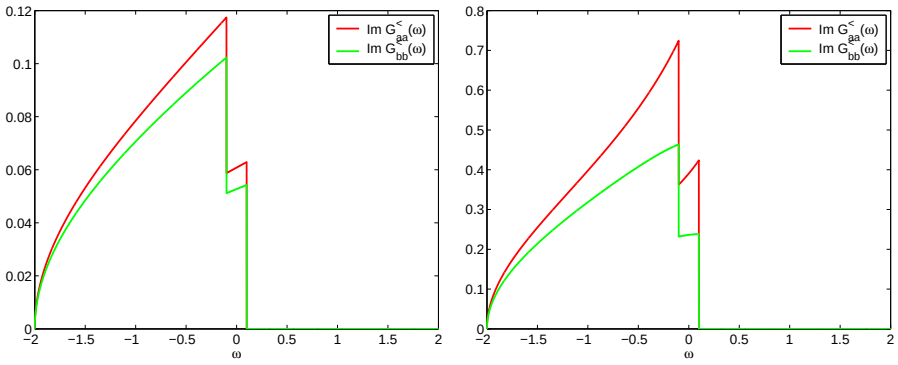

(a) $V_g = -4$.

(b) $V_g = -2$.

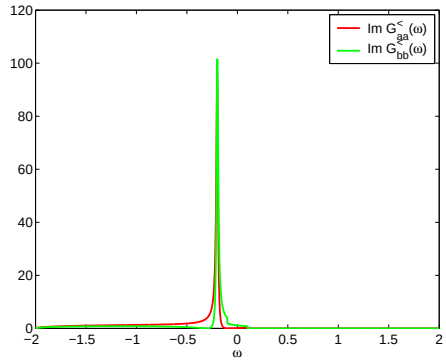

(c) $V_g = -1$.

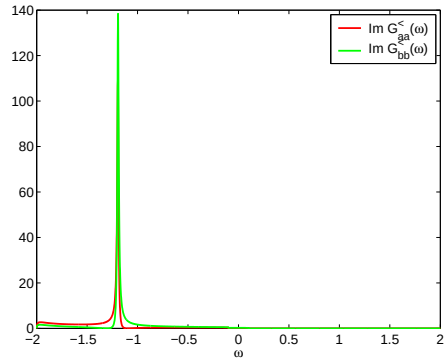

(d) $V_g = 0$.

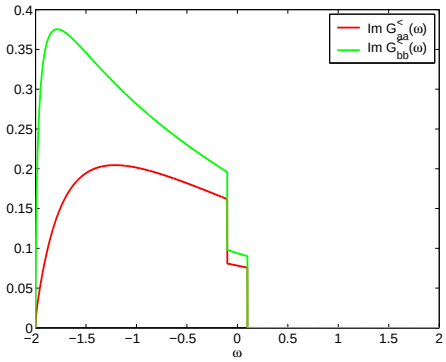

(e) $V_g = 1$.

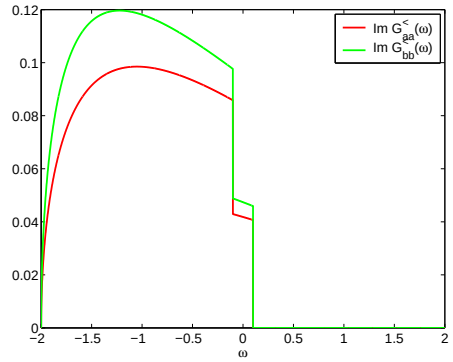

(f) $V_g = 2$.

Figure F.5: Im$G^<(\omega)$ for $V_i^{L/R} = 0.5$. Notice the cut-off due to the finite bandwidth.

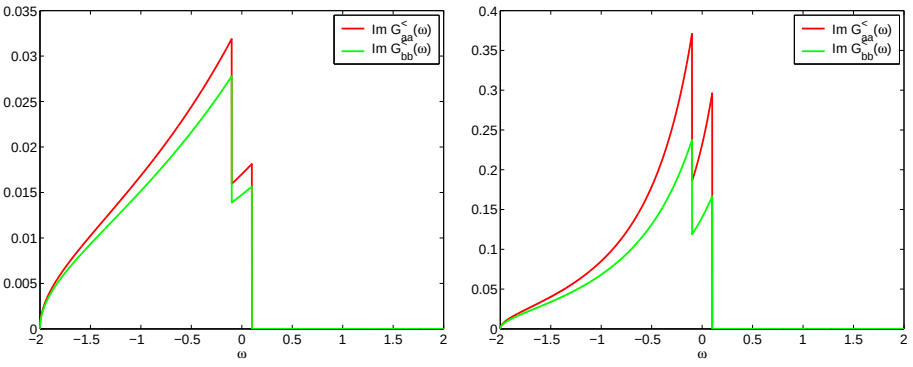

(a) $V_g = -4$. (b) $V_g = -2$.

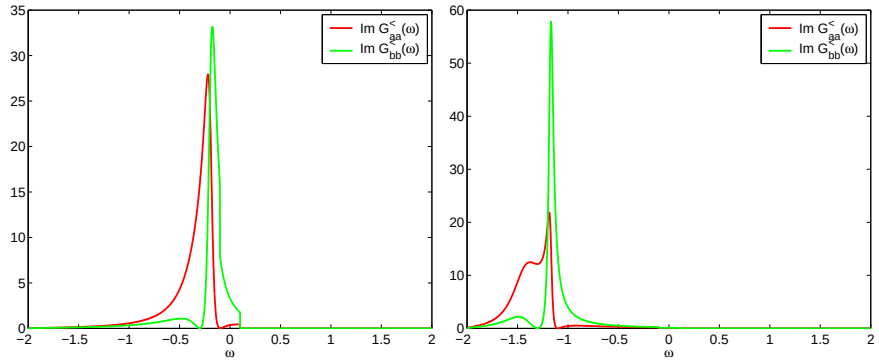

(c) $V_g = -1$. (d) $V_g = 0$.

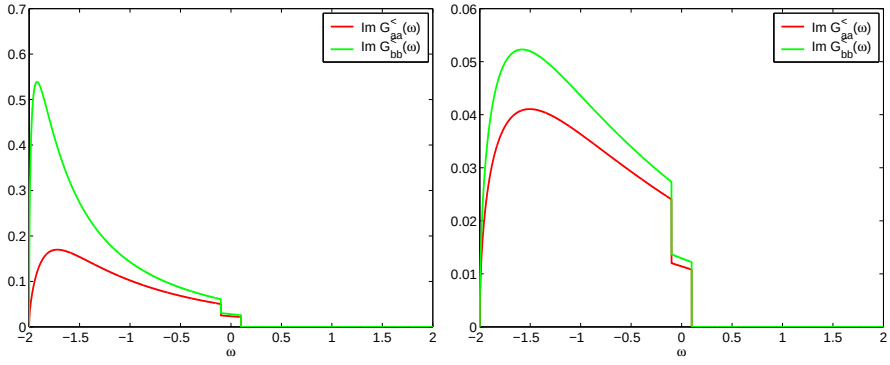

(e) $V_g = 1$. (f) $V_g = 2$.

Figure F.6: Im$G^<(\omega)$ for $V_i^{L/R} = 0.25$. Notice the cut-off due to the finite bandwidth.

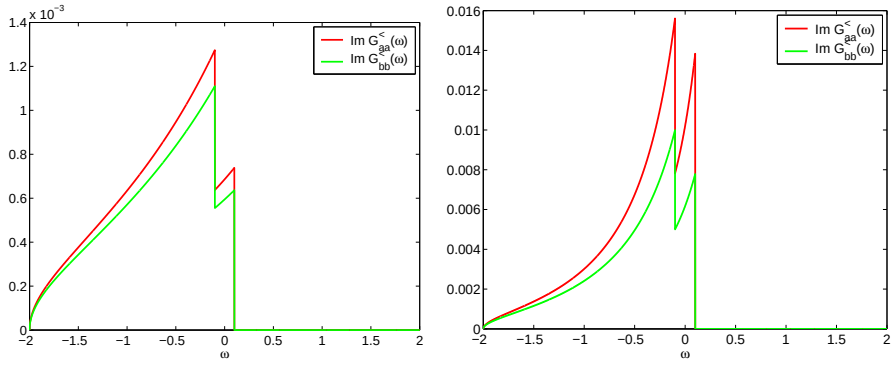

(a) $V_g = -4$.

(b) $V_g = -2$.

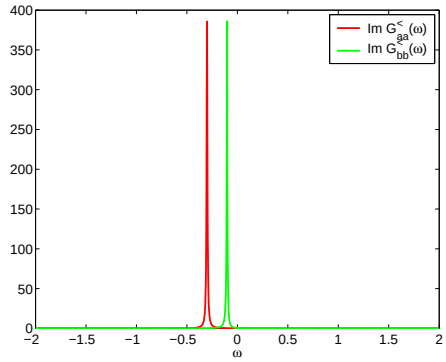

(c) $V_g = -1$.

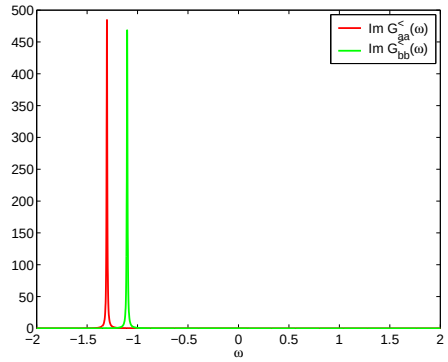

(d) $V_g = 0$.

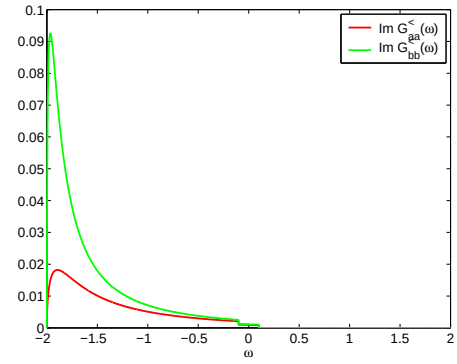

(e) $V_g = 1$.

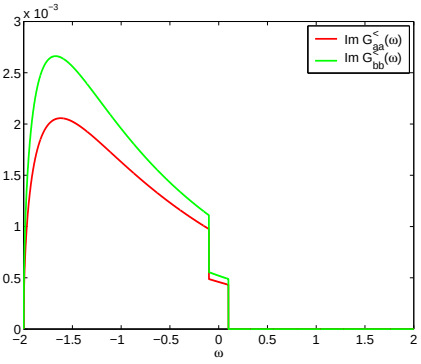

(f) $V_g = 2$.

Figure F.7: Im$G^<(\omega)$ for $V_i^{L/R} = 0.05$. Notice the cut-off due to the finite bandwidth.

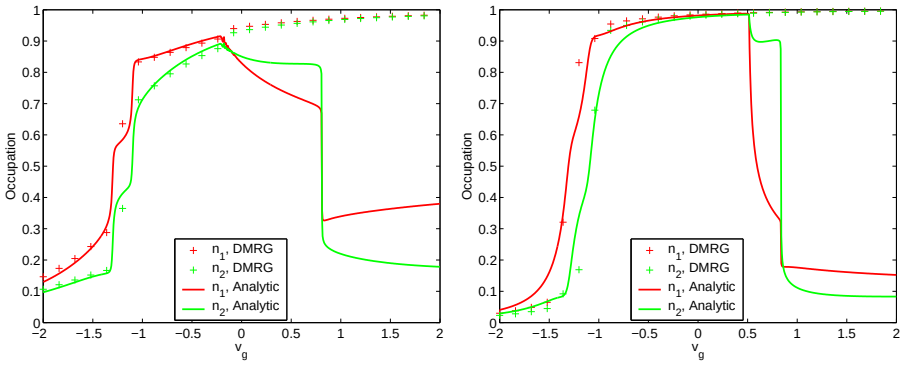

(a) $V_i^{L/R} = 0.5$. (b) $V_i^{L/R} = 0.25$.

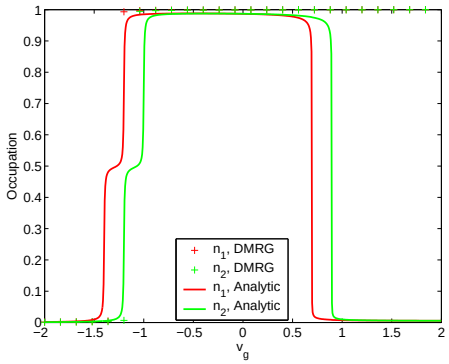

(c) $V_i^{L/R} = 0.05$.

Figure F.8: Comparison between DMRG and analytic occupations for $\epsilon = [-1.3, -1.1]$, $\mu_L = -\mu_R = 0.1$, $m = 32$ states, and 125 sites in the lead. The large gate occupations are not reproduced by DMRG since we have not incorporated the finite band width in our implementation. U, $V_i^{L/R}$, ϵ, and V_g are given in units of t.

Bibliography

[1] K. G. Wilson and J. Kogut, The Renormalization Group and the ϵ Expansion, Physics Reports **12**(2), 75–200 (1973).

[2] I. Peschel, X. Wang, M. Kaulke, and K. Hallberg, *Density-Matrix Renormalization*, volume 528 of *Lecture Notes in Physics*, Springer-Verlag, 1999.

[3] S. R. White, Density matrix formulation for quantum renormalization groups, Phys.Rev.Lett. **69**(19), 2863–2866 (1992).

[4] S. R. White, Density-matrix algorithms for quantum renormalization groups, Phys.Rev.B. **48**(14), 10345–10356 (1993).

[5] P. Schmitteckert, Nonequilibrium electron transport using the density matrix renormalization group, cond-mat/0403759 (2004).

[6] S. R. White and A. E. Feiguin, Real time evolution using the density matrix renormalization group, cond-mat/0403310 (2004).

[7] E. Jeckelmann, Dynamical density-matrix renormalization-group method, Phys.Rev.B. **66**, 045114 (2002).

[8] R. P. Feynman, *Statistical Mechanics – A set of lectures*, W. A. Benjamin, INC., 1972.

[9] N. Shibata, Application of the density matrix renormalization group method to finite temperatures and two-dimensional systems, cond-mat/0310028 (2003).

[10] S. Caprara and A. Rosengren, Density-matrix renormalization group for fermions: Convergence to the infinite-size limit, Nuclear Physics B. (493), 640–650 (1997).

[11] J. Eising, *Lineær Algebra*, Institut for Matematik – Danmarks Tekniske Universitet, 2nd edition, 1997.

[12] E. R. Gagliano and C. A. Balseiro, Dynamical Properties of Quantum Many-Body Systems at Zero Temperature, Phys.Rev.Lett. **59**(26), 2999–3002 (1987).

[13] K. Hallberg, Density-matrix algorithm for the calculation of dynamical properties of low-dimensional systems, Phys.Rev.B. **52**(14), 9827–9830 (1995).

[14] J. R. Laguna, *Real Space Renormalization Group Techniques and Applications*, PhD thesis, Instituto de matemáticas y Física Fundamental (CSIC), 2001.

[15] M. Anderson, *Numerical Renormalization, Doped Antiferromagnets, and Statistics – Topics in Low Dimensional Physics*, PhD thesis, Departement of Theoretical Physics, Chalmers University of Technology, Göteborg University, 2001.

[16] R. Berkovits, Density matrix renormalization group study of the charging of a quantum dot strongly coupled to a single lead, cond-mat/0306284 (2003).

[17] H. Bruus and K. Flensberg, *Quantum field theory in condensed matter physics*, Ørsted Laboratory, Niels Bohr Institute, 2001.

[18] H. Haug and A.-P. Jauho, *Quantum Kinetics in Transport and Optics of Semiconductors*, Springer Series in Solid-State Sciences, Springer-Verlag, 1998.

[19] R. Berkovits, F. v. Oppen, and J. W. Kantelhardt, Discrete charging of a quantum dot strongly coupled to external leads, cond-mat/0307730 (2003).

[20] M. A. Martín-Delgado, G. Sierra, and R. M. Noack, The density matrix renormalization group applied to single-particle quantum mechanics, J.Phys.A:Math.Gen. **32**(33), 6079–6090 (1999).

[21] I. P. Bindloss, Phases of the interacting one-dimensional electron gas coupled to phonons, cond-mat/0404154 (2004).

[22] E. Papa, Nonuniversal properties of the single-particle density of states of 1D system with electron-phonon interactions, cond-mat/0403287 (2004).

[23] T. Frederiksen, Inelastic electron transport in nanosystems, Master's thesis, MIC/DTU, 2004.

[24] E. Jeckelmann and S. R. White, Density-matrix renormalization-group study of the polaron problem in the Holstein model, Phys.Rev.B. **57**(11), 6376–6385 (1998).

[25] T. D. Kühner and S. R. White, Dynamical Correlation Functions using the Density Matrix Renormalization Group, cond-mat/9812372 (2004).

[26] A. Juozapavičius, *Density-Matrix Renormalization-Group Analysis of Kondo and XY models*, PhD thesis, Royal Institute of Technology, Sweden, 2001.

[27] J. König, Y. Gefen, and G. Schön, Level Statistics of Quantum Dots Coupled to Reservoirs, Phys.Rev.Lett. **81**(20), 4468–4471 (1998).

[28] L. E. Ballentine, *Quantum Mechanics – A Modern Development*, World Scientific Publishing Co. Pte. Ltd., 1999.

[29] B. H. Bransden and C. J. Joachain, *Quantum Mechanics*, Prentice Hall, 2nd edition, 2000.

[30] C. Kittel, *Introduction to Solid State Physics*, John Wiley & Sons, 7th edition, 1996.

[31] C. Zhang, E. Jeckelmann, and S. R. White, Density matrix Approach to Local Hilbert Space Reduction, Phys.Rev.Lett. **80**(12), 2661–2664 (1998).

[32] G. Fano, F. Ortolani, and L. Ziosi, The density matrix renormalization group method. Application to the PPP model of a cyclic polyene chain., cond-mat/980307 (1998).

[33] K. Hallberg, Density Matrix Renormalization: A Review of the Method and its Applications, cond-mat/0303557 (2003).

[34] M. A. Cazalilla and J. B. Marston, Time-Dependent Density-Matrix Renormalization Group: A Systematic Method for the Study of Quantum Many-Body Out-of-Equilibrium Systems, Phys.Rev.Lett. **88**, 256403 (2002).

[35] G. D. Mahan, *Many-Particle Physics*, Kluwer Academic/Plenum Publishers, 2nd edition, 1999.

[36] S. Daul, I. Ciofini, C. Daul, and S. R. White, Full-CI Quantum Chemistry Using the Density Matrix Renormalization Group, International Journal of Quantum Chemistry **79**(6), 331–342 (2000).

[37] A. O. Mitrushenkov, G. Fano, F. Ortolani, R. Linguerri, and P. Palmieri, Quantum chemistry using the density matrix renormalization group, Journal of Chemical Physics **115**(15), 6815–6821 (2001).

[38] Y. Park and S. Liang, Charge and spin dynamics of the Hubbard chains, Physica C **328**, 200–206 (1999).

[39] S. Elliot, *The Physics and Chemistry of Solids*, John Wiley & Sons, 2000.

[40] G. D. Mahan, *Applied Mathematics*, Kluwer Academic/Plenum Publishers, 2002.

[41] Y. Nishiyama, Folding of the triangular lattice in a discrete three-dimensional space: Density-matrix-renormalization-group study, cond-mat/0403747 (2004).

[42] H. Benthien and F. Gebhard, Spectral function of the one-dimensional Hubbard model away from half filling, cond-mat/0402664 (2004).

[43] H. Matsueda, T. Tohyama, and S. Maekawa, Dynamical DMRG study of photoexcited states in one-dimensional Mott insulators, cond-mat/0402298 (2004).

[44] R. A. Molina, D. Weinmann, and J.-L. Pichard, Length-dependent oscillations of the conductance through atomic chains: The importance of electronic correlations, Europhysics Letters, cond-mat/0402307 (2004).

[45] A. J. Daley, C. Kollath, U. Schollwöck, and G. Vidal, Time-dependent density-matrix renormalization-group using adaptive effective Hilbert spaces, cond-mat/0403313 (2004).

[46] D. García, K. Hallberg, and M. J. Rozenberg, Dynamical Mean Field Theory with the Density Matrix Renormalization Group, cond-mat/0403169 (2004).

[47] S. Nishimoto and E. Jeckelmann, Density-matrix renormalization group approach to quantum impurity problems, cond-mat/0311291 (2003).

[48] D. J. J. Farnell, Density Matrix Renormalization Group Calculations for Two-Dimensional Lattices: An Application to the Spin-Half and Spin-One Square Lattice Heisenberg Models, cond-mat/0309057 (2003).

[49] L. Capriotti, D. J. Scalapino, and S. R. White, Spin-liquid versus dimerized ground states in a frustrated Heisenberg antiferromagnet, cond-mat/0404085 (2004).

[50] G. K.-L. Chan and M. Head-Gordon, Highly correlated calculations with a polynomial cost algorithm: A study of the density matrix renormalization group, Journal of Chemical Physics **116**(11), 4462–4476 (2002).

[51] I. P. McCulloch and M. Gulácsi, Density Matrix Renormalization Group Method and Symmetries of the Hamiltonian, Aust.J.Phys. **53**, 597–612 (2000).

[52] M. Andersson, M. Boman, and S. Östlund, Density Matrix Renomalization Group of Gapless Systems, cond-mat/9810093 (1998).

[53] E. Capelluti, B. Cerutti, and L. Pietronero, Charge fluctuations and electron-phonon interaction in the finite-U Hubbard model, cond-mat/0312654 (2003).

[54] J. Dukelsky and S. Pittel, The Density Matrix Renormalization Group for finite Fermi systems, cond-mat/0404212 (2004).

[55] C. A. Büsser, G. B. Martins, K. A. Al-Hassanieh, A. Moreo, and E. Dagotto, Interference Effects in the Conductance of Multi-Level Quantum Dots, cond-mat/0404426 (2004).